Pixellated Radiation Detectors
for Scientific Applications

Dzmitry Maneuski

University of Glasgow

Department of Physics and Astronomy

Submitted in fulfilment of the requirements

for the degree of Doctor of Philosophy

June 2009

In memory of Antonina Gostilo...

Abstract

The work in this thesis is focused on the characterisation and evaluation of two classes of science-grade radiation imaging detectors. The first class is Monolithic Active Pixel Sensors (MAPS) . Advances in CMOS fabrication technologies over the last four decades have allowed MAPS to compete with Charge-Coupled Devices (CCD) in many applications. The technology also provides relatively inexpensive ways to tailor design to suit specific application needs. It is important to understand performance capabilities of new sensor designs through characterisation and optimisation of readout parameters. In this work three MAPSs were characterised.

The first one - HEPAPS4 - was designed for charged particle detection, with a potential technology application in the vertex detector for the International Linear Collider. The noise of the sensor was measured to be $35 \pm 5 \ e^-$, which agrees well with simulated data. The dark current was found to be $175 \ pA/cm^2$. The signal-to-noise performance for minimum ionising particles detection was demonstrated to be 40. The sensor was also evaluated for indirect detection of thermal and fast neutrons using lithium and polyethylene converters. The technology performed well in such an application with an estimated fast neutron detection efficiency of $\sim 0.01\%$. The second sensor characterised - Vanilla MAPS - was designed to evaluate new techniques for fast readout, small noise and reduced image lag. The system was capable of reading out 150 full frames (520×520 pixels) per second; the sensor had $14 \pm 4 \ e^-$ noise and decreased image lag. The

dark current density was found to be 50 pA/cm^2. The back-thinned version of the sensor demonstrated a dramatic improvement in quantum efficiency from 0% to 20% at 220 nm. The third device characterised was the parametric sensor eLeNA. It features 14 test structures designed to evaluate noise reduction architectures. The most promising structures showed temporal noise values as low as 6 e^- and 20 e^- fixed pattern noise.

The second class of imaging detectors - hybrid pixel detectors - was evaluated for two applications. The Medipix detector was used as the core element of the ATLAS radiation background monitoring system. The sensors were covered with neutron converters, which extended the number of radiation types that can be detected. X-ray calibration was performed, showing excellent tolerance of all 18 devices characterised. Detection efficiencies were estimated to be $\sim 1\%$ for thermal and $\sim 0.1\%$ for fast neutrons. The second application of Medipix explored was mass spectrometry. The detector was placed in the focal plane of a prototype mass spectrometer. Two-dimensional representation of data allowed focusing correction of the ion beam. The system was capable of detecting ions with energies in the range of $5 - 25$ keV. The detector characterisation with a broad range of ions (from Cu to Pb) showed very good quantitative agreement with table data.

Acknowledgements

First of all, I would like to express deep gratitude to my supervisor Val O'Shea. Without his help, efforts and patience this PhD would hardly be possible. I also appreciate his expertise and guidance over the last few years that enabled me to accomplish this thesis on time. I thank David Saxon for giving me an opportunity to do PhD by providing University scholarship and Ken Smith for supporting my case. My second supervisor Craig Buttar deserves many thanks not only for believing in me, but also for genuine interest in what I was doing and very helpful discussions of physics stuff and thesis manuscript.

Very special acknowledgments go to Lars Eklund and Andy Blue, who I closely worked with throughout my PhD time. I deeply appreciate the patience and time they invested in me. The level of attention and help I was given was far beyond normal, but this made me work harder and grasp knowledge much quicker. Lars, thanks for helping out off working times in a mad rush literally hours before conferences. Cheers Andy for perfect organisation of free time during unforgettable trips to Erlangen and Dresden.

The other special thanks I address to Keith Mathieson. Despite not being directly involved in my research, he was always ready to provide any help he could. His quality advice, patience and deep knowledge of the subject heavily influenced my research and made the learning process more enjoyable and less painful.

It was pleasure to work with and get support from many people. In Glasgow

University I would like to thank Richard Bates, Andrew Laing, David Forrest, Sarah Houston, Fred Doherty, John Melone and Fiona McEwan.

In the MI3 Collaboration I really appreciate the help, quality advice and always prompt responses from Renato Turchetta (RAL). Life would be much more complicated without these things... Thanks to Andy Clark, Thalis Anaxagoras and Tim Pickering – it was an extraordinary experience to work mad hours on eLeNA guys! Also thanks to Sarah Bohndiek from UCL.

During my PhD time I worked in close collaboration with Institute of Experimental and Applied Physics of Czech Technical University. I am grateful to Stanislav Pospíšil for an extremely well organised working environment, which made my time in Prague efficient, productive and enjoyable. His advice, expertise and knowledge not only helped me to learn quicker but also led to valuable results. I would like to thank Zdeněk Vykydal and Dominic Greiffenberg (from University of Frieburg) for enjoyable working hours on the ATLAS-Medipix project. Zdeněk also deserves an extra mention for many useful advice concerning technical Medipix issues. Thanks also go to Miloslav Králík from Czech Metrology Institute whose professionalism made all measurements painless and very time efficient. I also want to acknowledge Jan Jakůbek for quality discussions on a broad range of topics and brainstorming me with many ideas for future research and collaboration.

I also had an opportunity to work in Ukraine. Many thanks go to Valery Pugatch from Kiev Institute for Nuclear Research for proposing an interesting project and organisation of the trip. Thanks to Alexey Kovalchuk, Andrey Chaus and Lukas Tlustos (from CERN Microelectronics Design Group) for carrying out measurements with me. Not to forget the invaluable assistance given to us by Sergey Homenko, Andrey Shelekhov and Victor Eremenko from Sumy Institute of Applied Physics.

The writing up time was probably one of the most difficult periods during PhD. I deeply appreciate the commitment of Aaron Mac Raighne to read every

Declaration

I declare that except where explicit reference is made to the work of others, this dissertation is the result of my own work. This work has not been submitted for any other degree at the University of Glasgow or any other institution.

Dzmitry Maneuski

Contents

List of figures

xiii

List of tables

Chapter 1

Introduction

Improvements in radiation detection have been sought since the late 19th century, when the first X-ray image was demonstrated by W. Roentgen using the photographic plate [1]. At that time, photographic plates were the only apparatus available to record and store an image. This was until the widespread use of photographic film at the beginning of 20th century as a more convenient and less fragile method of X-ray imaging. Both photographic plates and film suffer from many drawbacks. They have a limited dynamic range, poor sensitivity and a non-linear response. However, the importance of film for physics should not be underestimated. Together with the Wilson's cloud chamber it played a crucial role in the understanding of basic principles of radioactive decay and the discovery of the atomic structure. The bubble chamber, invented in 1952, tackled the detection medium instability issues related to the cloud chamber and provided better time and spatial resolution [2]. However, an old style photographic plate readout remained in use, making it inconvenient for data analysis in repetitive experiments. Moreover, increasing particle energies were requiring larger and larger chambers in order to stop the particle and measure its energy.

Solid state detectors (SSD) came into play in the early $60s$ after the highly successful development of silicon and germanium single crystals for transistor tech-

nologies. They have many advantages over gaseous detectors, including among others better energy resolution, linearity of response over a wider energy range and compact design. Advances in electronics and fabrication processes enabled manufacturing of high resolution position sensitive detectors. They were fabricated on a single substrate by dividing the contact on the semiconductor into strips which can be read out by multi-channel electronics [3].

The invention of the charge-coupled device (CCD) in 1970 started a revolution in scientific imaging. Surprisingly, the inventors were looking for a silicon alternative to the magnetic bubble memory to make use of well developed silicon technology [4]. While CCDs have made an impact in the memory field, they had profound effects in the fields of optical imaging, astronomy, particle tracking, material sciences and X-ray detection [5]. The use of CCDs in many fields boosted the development of the technology to customise it to suit particular needs. This enabled CCDs to be the leading technology available for a majority of imaging applications for more than two decades.

Dramatic advances in the electronics industry over the last 40 years brought CMOS Monolithic Active Pixel Sensors (MAPS) into imaging as a feasible alternative to the CCDs in the early $90s$. Though they were hardly comparable to CCDs in terms of noise, leakage current and uniformity, the possible benefits of monolithic integration permitted complex on-chip functionality and drastic cost reductions which caught the eye of both the industrial and scientific communities.

An alternative technology is the hybrid pixel detector. These devices combine the advantages of CMOS technology and the benefits of exotic detection materials [6]. The detector is made of a pixellated single crystalline sensor which is bump bonded to a custom VLSI readout chip working in the single photon counting or current integration mode. This approach allows optimisation of the detector elements and the readout circuit separately. Such materials as Si, $GaAs$, $CdTe$ and $CdZnTe$ are available and actively researched [7], paving the way for new low dose, high efficiency spectroscopic applications.

The use of any sensor in high-end and scientific applications imposes stringent requirements on the devices. These strongly vary from one application to another and sometimes contradict each other. Noise performance is almost always of vital importance. In applications, like particle physics, where the image is formed by traversing particles within small regions, on-chip data processing becomes important, using complex in-pixel electronics. These sensors require fast response (order of ns), high resolution (order of micron) and small power dissipation. Additionally, radiation hardness is of vital importance to high energy physics applications such as tracking detectors and calorimeters. The above mentioned aspects were addressed in a number of ways. For example, in 3D detectors [8] the close implant spacing results in short signal collection times and high intrinsic radiation hardness. Vertical integration of sensor and electronics achieves the requirement of small mass, improved functionality and reduced power dissipation [9]. Minimisation of radiation dose is crucial in medical applications. This requires high detection efficiency. High dynamic range is essential to resolve low intensity and high intensity parts of an image simultaneously with good linearity. A broad range of integration times is required, from nanoseconds (*e.g.* measurements of fluorescence decay) up to hours in autoradiography [10]. These requirements are usually addressed by tailoring available technologies to suit either of the crucial parameters.

In this thesis an evaluation of three science-grade CMOS MAPSs was performed – HEPAPS4, Vanilla and eLeNA. The sensors were designed to test new technologies and pixel architectures for different applications. Also, a hybrid pixel detector Medipix was evaluated in two applications: ATLAS background monitoring system at the LHC and mass-spectrometry. The author of the thesis has also contributed to the simulation of the radiation hardness [11, 12, 13] of a new type of CCD with fast readout for the vertex detector of the proposed International Linear Collider [14] . However, due to the disbandment of the Linear Collider Flavour Identification (LCFI) Collaboration [15] the simulated data has

never been compared to measurements. This makes the simulation work rather irrelevant in the context of the thesis and for this reason it is not included. The rest of the thesis is organised as described bellow.

Chapter 2 overviews the fundamental principles of radiation interaction with matter. It describes relevant properties of silicon as it is the most commonly used material for radiation detection. Basic semiconductor structures, forming the building blocks of the more complex systems, are discussed and simulated data is compared to textbook examples. The latter part of the chapter reviews integrated circuits. Finally, the basic operating principles of two types of pixellated radiation detectors, CMOS MAPS and the hybrid pixel detector, are summarised.

Chapter 3 describes the theoretical basis for sensor characterisation. It defines the fundamental properties of the imaging sensors and describes in detail the techniques employed to quantify them.

Chapter 4 is devoted to a detailed characterisation of three CMOS Monolithic Active Pixel Sensors. The HEPAPS4 (High Energy Physics Active Pixel Sensor) was developed to evaluate the technology for particle physics applications. The basic properties of three variants of the sensor were estimated using photonic techniques. The noise of the sensor was estimated to be 35 e^-, which agrees well with simulated data. Minimum Ionising Particles (MIPs) were employed to quantify sensor suitability for charged particle detection. The signal-to-noise ratio of the system was found to be 40 for minimum ionising particles. Finally, the HEPAPS4 was evaluated for neutron detection for future neutron imaging applications of this technology and showed acceptable detection efficiency of $\sim 0.01\%$ for fast neutrons. The Vanilla sensor is a general purpose technology evaluation sensor, which features several new approaches to tackle fundamental limitations of the CMOS MAPSs. The results of detailed photonic characterisation of the sensor are described and conclusions drawn, showing low noise of 14 e^- and low dark current density of 50 pA/cm^2. Increased ultraviolet (UV) sensitivity (from 0% to 20% at 220 nm) was achieved by back-thinning. The last sensor tested is

a novel parametric sensor eLeNA (Low Noise APS), which was designed to evaluate various noise reduction architectures. It features fourteen test structures. All of them were characterised and the most significant results and discussion are presented. Some test structures achived 6 e^- temporal noise and 20 e^- fixed pattern noise.

Chapter 5 is devoted to the single photon counting CMOS hybrid pixel detector Medipix. Two applications of the detector based on the technology are described. The first one is the radiation background monitoring system for the ATLAS detector at the LHC. The necessity of such a system is explained, the detector calibration techniques are discussed and the preliminary results and conclusions of the commissioning of the monitoring network are reported, showing that the system performed well in the day of the LHC start up. The second application of the chip is the real time 2D detector in the focal plane of a mass spectrometer. The results of sensor characterisation are presented and the improvements for the prototype system are discussed. These include identifying and correcting magnet focusing problems using 2D beam representation; good agreement of measured element abundances with reference data and capability of the system to detect ions in the energy range $5 - 25 \; keV$.

Chapter 6 overviews the results of the thesis. General conclusions about the work are drawn and the main results are discussed.

Chapter 2

Principles of radiation detection

This chapter gives a literature overview of the theoretical background to radiation interactions with matter as well as the detection principles as applied to semiconductor radiation detectors. It is divided into five sections. Section 2.1 describes the types of radiation interaction relevant to the work described in this thesis. Section 2.2 is devoted to the properties of silicon related to the detection of radiation. In Section 2.3 the operational principles of a p-n diode and a field-effect transistor are discussed. Section 2.4 gives an introduction to the complementary metal-oxide-semiconductor (CMOS) technology. Finally, Section 2.5 describes the basic operational principles of two types of large scale pixellated radiation detector systems. A comprehensive introduction to the background of radiation detection can be found in [16]. Radiation detection instrumentation is well described in [17]. The theoretical background to semiconductor electronics is explained in [18].

2.1 Radiation interactions

The operation of any radiation detection system depends on the manner in which the radiation to be detected interacts with the detection medium. The under-

standing of the fundamental mechanisms by which radiation interacts and loses energy in matter dictates which combination of detection material and readout electronics is best suited to a particular requirement. This section gives an overview of the interaction mechanisms for the four groups of radiation relevant to this thesis:

- heavy charged particles (α-particles, protons);

- electrons;

- photons (γ-rays, X-rays, UV and visible);

- neutrons;

The first three groups of radiation can be directly detected in a semiconductor via different interaction mechanisms while special conversion materials are required for neutron detection.

2.1.1 Heavy charged particles

Heavy charged particles interact with matter mainly through the Coulomb force between its charge and orbital electrons surrounding a nuclei. The charged particle transfers its energy to many electrons upon entering the detection medium. It causes the electrons to gain energy and get excited into a higher orbital shell or leave the atom causing *ionisation*. The charged particle in turn is gradually slowed down until it stops. The *specific energy loss* of the particle along the track is described by the *Bethe* equation

$$S \equiv -\frac{dE}{dx} = \frac{4\pi e^4 z^2}{m_e v^2} NZ \left[ln\frac{2m_e v^2}{I} - ln(1 - \frac{v^2}{c^2}) - \frac{v^2}{c^2} \right] \tag{2.1}$$

where v and $z \cdot e$ is the velocity and charge of the particle, m_e is the electron rest mass, N is the number of atoms per unit volume, Z is the atomic number. I is the average ionisation and excitation potential of the absorption material, which is usually an experimentally determined parameter [16].
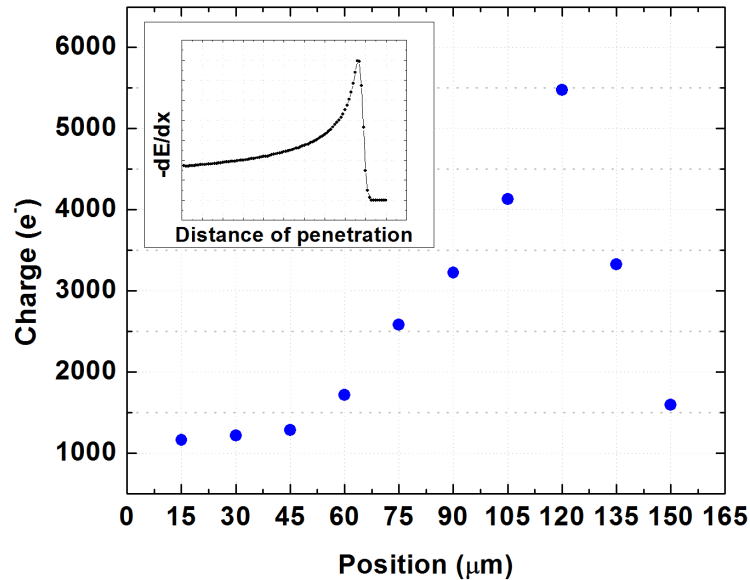
Figure 2.1: A typical Bragg curve showing the variation of energy loss as a function of the penetration depth of a recoil proton in silicon recorded with the HEPAPS4 sensor. The insert shows theoretical textbook example.

A plot of the specific energy loss along the track of a charged particle is known as the *Bragg curve*. An example of such a track for protons is illustrated in Fig. 2.1. At the beginning of the path a charged particle tends to capture electrons from atoms of the traversing material. The particle is gradually losing energy, increasing the interaction cross section which results in a peak. Near the end of the track, the particle charge is reduced through electron capture and the curve falls off. This plot is an experimental result obtained with the HEPAPS4 sensor adapted to record neutron interactions (for details of the experiment see Section 4.1.6, page 79).

2.1.2 Fast electrons

The specific electron energy loss is described by an expression similar to the Bethe equation. In contrast to heavy charged particles, electrons follow erratic
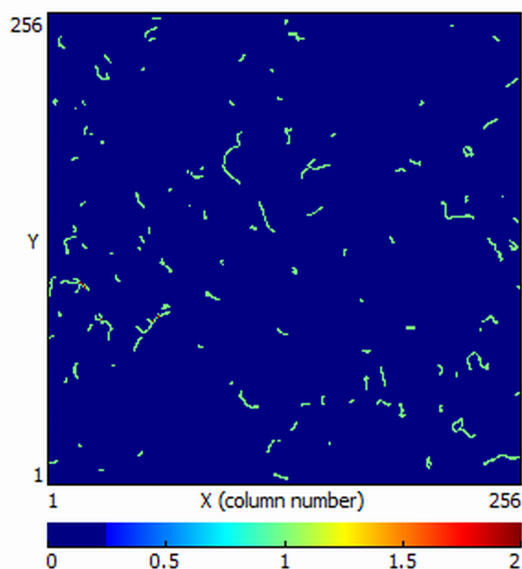
Figure 2.2: A snapshot of electron interaction in silicon detector recorded by Medipix chip.

paths and can either lose their energy in a single collision or experience multiple scattering and sharply change direction (also known as "random walk"). This is demonstrated in Fig. 2.2. They not only lose their energy by Coulomb interactions, but due to their small mass a different energy loss mechanism occurs: the emission of electromagnetic radiation arises from the electron scattering in the electric field of a nucleus in a form of *bremsstrahlung*. This can be understood as a radiation arising from the acceleration of the electron caused by the electrical attraction of the nucleus. Bremsstrahlung plays significant role for high-energy electrons and for absorption materials of large atomic number. The total linear stopping power of electrons is the sum of collisional and radiative loses [16].

The variation of the specific energy loss for electrons of different energies in lead is shown in Fig. 2.3. Electrons lose energy primarily due to ionisation at low energies. The value of dE/dx decreases logarithmically, approaching a near flat broad minimum at the energies of several hundred MeV. Such behaviour is typical for a wide range of particles when they approach the speed of light. Fast elections, as well as other relativistic particles, are often referred to as "Minimum
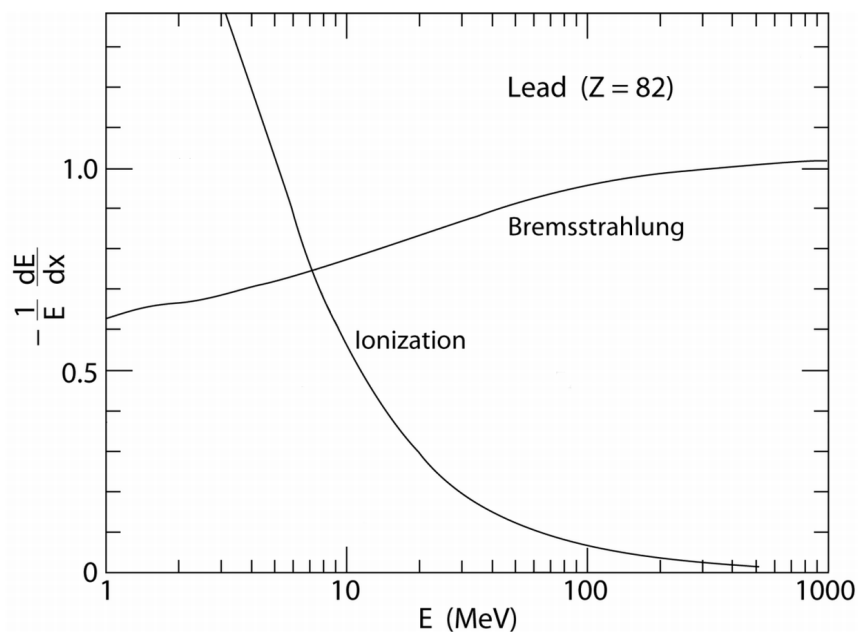
Figure 2.3: Specific energy loss in lead as a function of electron energy (adapted from [19]).

Ionising Particles" (MIPs). The bremsstrahlung energy loss becomes important only after a few MeV, it rises nearly linearly and almost saturating after $\sim$ 200 MeV.

2.1.3 Photons

Since photons are a form of electromagnetic radiation, they have zero mass, zero charge and travel at the speed of light. Three major types of interaction mechanisms play an important role in radiation measurements. The photo-electric effect dominates in the energy range of up to $\sim 100~keV$. The Compton effect contributes significantly at higher energies, while electron-positron pair production is possible at energies above $\sim 1~MeV$. The relative importance of these three processes, as a function of photon energy, is shown in Fig. 2.4. The lines to the left and to the right represent the energy at which the Compton effect is equally probable with photoelectric effect and pair production respectively as a function of the absorber atomic number.
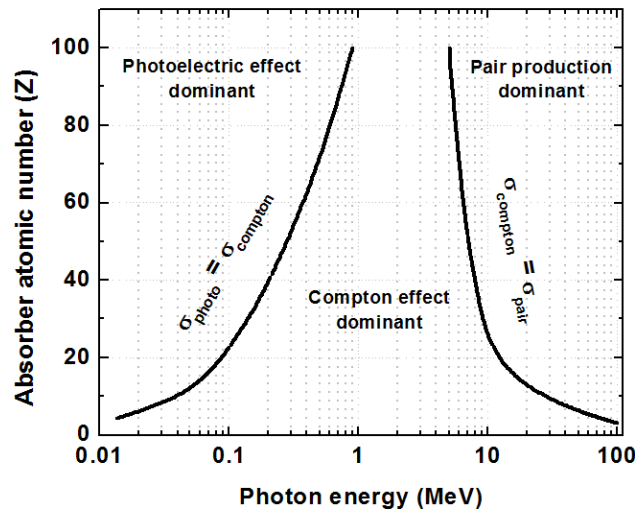
Figure 2.4: The relative importance of the three types of photon interaction at different energies and for different atomic numbers.

Photoelectric effect

The photoelectric effect occurs when a photon undergoes absorption by an atomic electron with the subsequent ejection of the electron from one of the bound shells of an atom. The energy of the outgoing electron is given by

$$E = h\nu - E_{bin} \tag{2.2}$$

where E is the energy of the ejected electron, $h\nu$ is the energy of the incident photon and E_{bin} is the binding energy of the electron in the atom.

The photoelectric effect has a higher probability which occurs when the energy of the incident photon becomes higher than the binding energy of the electron which it interacts with. The primary mechanism for the absorption of visible light photons is the elevation of electrons to higher energy levels, *excitation*. There are many available states, so visible light is strongly absorbed. In the case of X-ray photons, their energies are too high to be absorbed in electron transitions between states for most atoms, so they can interact with an electron only by knocking it completely out of the atom, causing *ionisation*. If the energy of X-ray / γ - ray
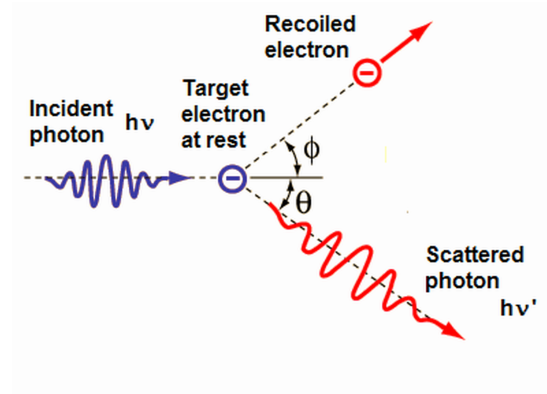
Figure 2.5: Kinematics of Compton scattering.

photon is high enough, another mechanism of energy loss takes place - Compton scattering.

Compton scattering

Compton scattering occurs as a result of a high-energy photon colliding with a target, which releases loosely bound electrons from the outer shell of the atom. The kinematics of the energy transfer is shown in Fig. 2.5 and described by the following equation

$$h\nu' = \frac{h\nu}{1 + \frac{h\nu}{m_0 c^2}(1 - \cos\theta)} \tag{2.3}$$

where $m_0 c^2$ is the rest-mass energy of the electron ($0.511~MeV$), $h\nu$ and $h\nu'$ is the energy of incident and recoil photon respectively.

The incoming photon is deflected to an angle θ with respect to its original direction. A fraction of the photon's energy is transferred to the electron. This energy can vary from zero to a large fraction of the γ - ray energy, as all scattering angles are possible [20] with varying probabilities.

Electron-positron pair production

Gamma-ray photons with energy greater than $1.02~MeV$ may interact with a nucleus to form an electron-positron pair. This amount of energy is just sufficient

to provide the rest masses of the electron and positron (0.511 MeV each). Excess energy goes into kinetic energy equally shared between these two particles, which produce ionisation as they travel in the material. The positron is eventually captured by an electron and annihilation of the two particles occurs. This results in the release of two photons each of 0.511 MeV known as *annihilation radiation*. These two photons then lose energy by Compton scattering or the photoelectric effect.

Photon attenuation

Photons are electrically neutral, they do not steadily lose energy via Coulomb interactions with atomic electrons as charged particles do. The penetration depth of photons is governed by statistical interaction probability of occurrence and depends on photon energy and material being traversed. This probability is called the *linear attenuation coefficient*, μ. The number of transmitted photons I is given by the following equation

$$I = I_0 e^{-\mu t} \tag{2.4}$$

where I_0 is number of incident photons on the absorption material, μ is the sum of the probabilities of photoelectric effect, Compton scattering and pair production interactions, t is the absorber thickness expressed in g/cm^2.

2.1.4   Neutrons

Neutrons do not carry charge, therefore they cannot be detected directly by means of the Coulomb force. Only nuclear reactions with the emission of secondary radiation provide means of detection. Two kinds of such reactions exist. The first one is based on an immediate nuclear charged particle emission, similar to the reaction ${}_3^6Li(n, \alpha){}_1^3H$. The second kind of reaction - *activation* - results in radiation emission (β^+, β^- or γ - rays), which can be detected after the irradiated

material is removed from the neutron field. The work done in this thesis is based on the first type of reaction only.

The relative probability of different types of neutron interaction varies dramatically with neutron energy. Typically neutrons are classified as *thermal* (or *slow*) ($E < 1\ keV$), *epithermal* ($1 < E < 500\ keV$) and *fast* ($0.5 < E < 20\ MeV$). When a neutron interacts with matter, it may undergo a variety of nuclear processes depending on its energy. Among those of interest are:

- Elastic scattering from nuclei, $A(n, n)A$. This is the principal mechanism of energy loss for fast neutrons.

- Inelastic scattering, $A(n, n')A^*$. In such a reaction, the nucleus is left in an excited state which may later undergo a γ-decay. The neutron must have sufficient energy to excite the nucleus and usually is in the range above $1\ MeV$.

- Other kinds of nuclear reaction in which the neutron is captured by the nucleus and a charged particle is emitted, *e.g.* $(n,\ p)$, $(n,\ \alpha)$, $(n,\ d)$, $(n,\ t)$. These reactions are more relevant to slow neutrons in the energy range from eV to keV.

2.2 Silicon semiconductor properties

Silicon is one of the most widely used semiconductor material both in radiation detection and electronics industry. It has adequate chemical and mechanical properties, *e.g.* its natural oxide is easily grown while forming a better semiconductor/dielectric interface than any other semiconductor. Various techniques were developed to purify or grow very high purity silicon [21].

The radiation detection community uses crystalline silicon as a detection medium for several main reasons in addition to those mentioned above. Impurities can be introduced into the silicon in a highly controlled way significantly

Conduction band

Valence band

Metal   Semiconductor   Insulator
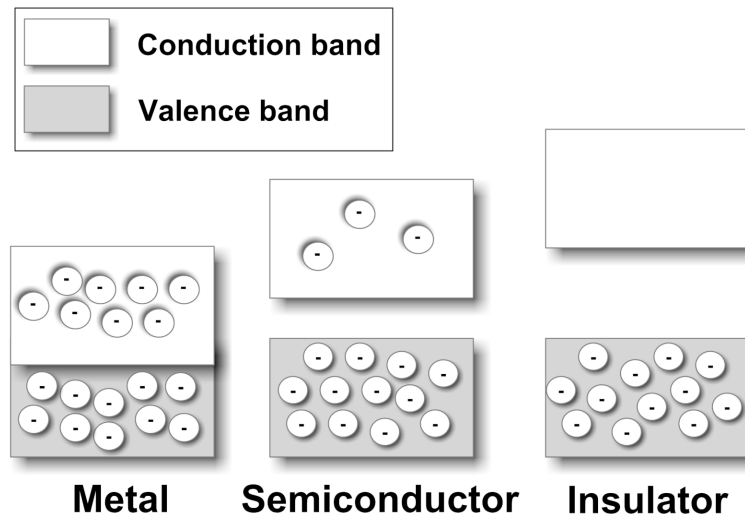
Figure 2.6: Energy band structure of metal, semiconductor and insulator.

changing electrical properties of the crystal. It has a low ionisation energy, which leads to good signal levels. The high mobility of charge carriers leads to fast charge collection. Relatively long mean free path gives good charge collection efficiency. An overview of the relevant semiconductor properties is explained in the following sub-section.

2.2.1   Energy band structure

Silicon is a crystalline semiconductor material whose outer shell atomic levels can be represented by an energy band structure. Fig. 2.6 schematically illustrates such a structure, which consists of a *valence band*, a "forbidden" *energy gap* and a *conduction band*. The valence and conduction bands have many discrete energy states, while there are no available states in the energy gap region. Discrete levels exist as the Pauli principle forbids two electrons with one spin from being in the same state. There are as many energy levels as there are electron pairs in the crystal. The width of the bands and the band gap are defined by the lattice spacing between atoms. In insulators, the energy gap is large while in metals it does not exist.

Under normal conditions, where an external electric field is applied to the insulator, no current is observed as there is not enough energy to excite electrons from the valence band to the conduction band across the gap. In metals, as there is no gap, thermal energy is enough to excite electrons to the conduction band. Therefore, a current is easily generated if an external electric field is applied. In semiconductors the energy gap is finite. So only a few electrons are excited from the valence band by the thermal energy and, when external electric field is applied, only a small current is generated at room temperature. The amount of electrons excited over the band gap can be increased by putting impurities in to the silicon crystal. This introduces the concept of *intrinsic* and *extrinsic* semiconductors.

2.2.2 Intrinsic and extrinsic silicon

The intrinsic carrier concentration of pure silicon denotes the number of electrons and holes present in the semiconductor. This can be described by the following equations

$$n = N_C \exp\left(\frac{E_C - E_F}{kT}\right), N_C = \left(\frac{m_e kT}{2\pi h}\right)^{3/2}$$
$$p = N_V \exp\left(\frac{E_F - E_V}{kT}\right), N_V = \left(\frac{m_p kT}{2\pi h}\right)^{3/2} \tag{2.5}$$

where N_C and N_V are the number of states in the conduction and valence band, E_F the Fermi energy, E_C and E_V are the conduction and valence band energies, m_e and m_p are the effective masses of electrons and holes respectively.

In intrinsic silicon the concentration of electrons in the conduction band is equal to the concentration of holes in the valence band. Therefore the total concentration of carriers is equal to

$$n_i = \sqrt{np} \tag{2.6}$$

At room temperature ($T = 300\ K$) a typical intrinsic concentration of carriers in silicon is $n_i = 10^{10}\ cm^{-3}$ [17]. Compared to the room temperature concen-

tration of electrons in metals of in the order of $n_i = 10^{21} \ cm^{-3}$, the value for semiconductors is very small.

By adding impurity atoms in a controlled way the density of electrons or holes in silicon can be altered significantly. The semiconductor becomes *doped* or *extrinsic*. Two kinds of atoms are commonly introduced into silicon. If the dopant is pentavalent, four electrons form covalent bonds with the silicon atom, while one electron is left free, forming an energy level very close $(0.05 \ eV)$ to the conduction band. At normal temperatures, therefore, the extra electron is easily excited into the conduction band where it enhances the conductivity. In such materials current is mainly due to the movement of electrons. Doped semiconductors in which electrons are the majority carriers are called *n-type* semiconductors. If the impurity atom is trivalent with one less valence electron, there are not enough electrons to fill the valence band, there is an excess of holes in the material. These kinds of impurities create extra energy states in the gap close to the valence band. Electrons can then be easily excited to this level and the holes become the majority charge carriers. Such materials are referred to as *p-type* semiconductors.

Phosphorus is usually used to make n-type silicon while boron is mostly employed as an acceptor impurity for p-type material. The concentration of impurity atoms used is usually several orders of magnitude less then the concentration of silicon atoms. Nevertheless heavily doped silicon is used in applications for electrical contacts in semiconductors. To distinguish such a material from normally doped Si, a "+" sign after the material type is used (n^+ for donor and p^+ for acceptor material).

2.2.3 Carrier transport in semiconductors

The previous section described the natural equilibrium state of the semiconductor. This section will deal with two cases of non-equilibrium states. *Diffusion* occurs when charge carriers are trying to reach equilibrium conditions due to

their non-uniform spacial distribution. *Drift* is an ordered movement of carriers due to externally applied electric field.

Diffusion

Diffusion takes place when the charge carriers are inhomogeneously distributed in the semiconductor. It arises due to the fact that carriers in the higher concentration region are more likely to move into a region with lower concentration to reach equilibrium. This results in a diffusion current with density

$$J_n^{diff} = qD_n\nabla n \quad , \quad J_p^{diff} = -qD_p\nabla p \tag{2.7}$$

where D is a diffusion constant, which is proportional to the thermal velocity and the mean free path of the carrier in the material.

The total diffusion current density from holes and electrons is given by

$$J_{diff} = qD_n\nabla n - qD_p\nabla p \tag{2.8}$$

Drift

The charge carriers in the conduction band are in random thermal motion with zero average displacement if a semiconductor is in an equilibrium state and no electric field is applied across it. An external electric field, E, will apply a force to each electron and hole. They are accelerated and scatter in the crystalline lattice losing momentum, eventually gaining an average *drift velocity*

$$v_n = -\mu_n E \quad , \quad v_p = \mu_p E \tag{2.9}$$

where μ_n and μ_p denote the carrier mobility for electrons and holes.

The drift velocity of the carriers is small compared to the thermal velocity if the electric field is low enough. So the average velocity of electrons and holes increases linearly with the external field. However, for higher electric fields a strong deviation from linearity can be observed. As the electric field strength

increases, scattering occurs more frequently and the drift velocity eventually saturates, becoming independent of the electric field.

A microscopic current density will be increased by the drift current

$$J_{drift} = (n\mu_n + p\mu_p)qE = \sigma E \tag{2.10}$$

σ is known as the *material conductivity*, while the inverse value is the *resistivity*, ρ.

Combining current contributions from diffusion and drift gives total current density for electrons and holes

$$J_n = qD_n\nabla n + n\mu_n qE \quad , \quad J_p = -qD_p\nabla p + p\mu_p qE \tag{2.11}$$

Diffusion and mobility for both electrons and holes are related to each other by the Einstein equation

$$D_n = \frac{kT}{q}\mu_n \quad , \quad D_p = \frac{kT}{q}\mu_p \tag{2.12}$$

Since the mobility of the charge carriers is defined as

$$\mu_n = -\frac{q\tau_c}{m_n} \quad , \quad \mu_p = \frac{q\tau_c}{m_p} \tag{2.13}$$

the diffusion constant of a material then depends upon the effective mass of the charge carriers, m_n, m_p, mean free time, τ_c), and the material temperature, T.

The semiconductor properties described above are the critical parameters that have led the development of solid state radiation detectors as well the vast number of electronic devices.

2.3 Semiconductor structures

2.3.1 The p-n junction diode

The p-n junction is probably the most important basic electronic structure. Its special properties have found application in a wide range of electronic devices
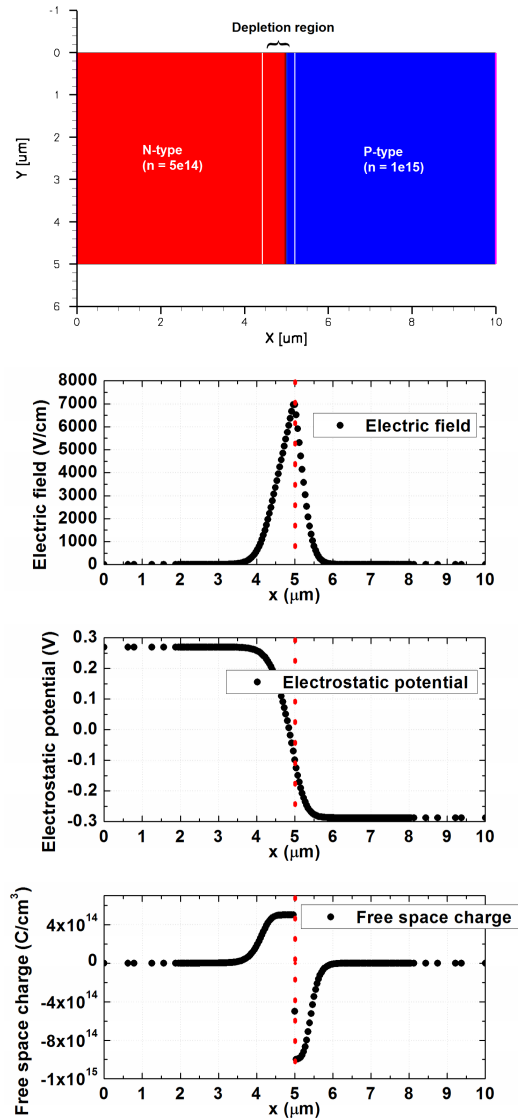
Figure 2.7: A typical p-n junction diode performance characteristics simulated in Synopsis Sentaurus TCAD [22].

as well as in radiation detection. It is formed by bringing into contact extrinsic semiconductors of opposite doping. The principle of operation of a p-n junction diode - one of the crucial elements for radiation detection devices - is described below.

Consider separate homogeneously doped p- and n-regions in thermal equilibrium. When they are brought into a close contact, the majority of carriers will

diffuse out to the areas of lower concentration: the electrons will diffuse to the p-type material and holes to the n-type material. This creates excess negative fixed space charge in the p-region and positive fixed space charge in the n-type region. An electric field that counteracts the diffusion will be established. It also sweeps away mobile charge carriers in the region around the junction interface, creating the *depletion region*. The resulting potential difference across this region is known as the *built-in voltage* (V_{bi}) and can be calculated as follows

$$V_{bi} = \frac{kT}{e} \ln \frac{n\,p}{n_i^2} \tag{2.14}$$

where n_i is the intrinsic carrier concentration. Fig. 2.7 demonstrates a simulated example of the distribution of the electric field, electrostatic potential and charge in a typical p-n junction diode. The electric field is established only in the depletion region. The maximum is achieved in the physical junction of two types of semiconductor. The field gradually decreases, reaching zero in the regions where the carrier concentration equilibrium is established. Electrostatic potential is positive in the n-type region because of the excessive positive charge and negative in the p-type region.

By applying an external voltage to the p- or n-type terminals of the diode, the depletion region can be either extended or contracted. Positive voltage on the contact with n-side (or negative on p-side) makes the diode *reverse biased*, extending the carrier free region. The opposite situation contracts the depletion region and is known as *forward biasing*. Mathematically this is described by the following equation

$$d = \sqrt{\frac{2\epsilon\epsilon_0(n+p)}{e\,n\,p}(V_{bi} - V)} \tag{2.15}$$

where V is the external voltage applied, e is elementary charge, ϵ and ϵ_0 is the permittivity in silicon and vacuum respectively.

These properties make the p-n junction diode suitable for basic radiation detection. The depleted volume remains free of mobile carriers even after the diode is irradiated. If a charged particle interacts in the diode, it creates e-h
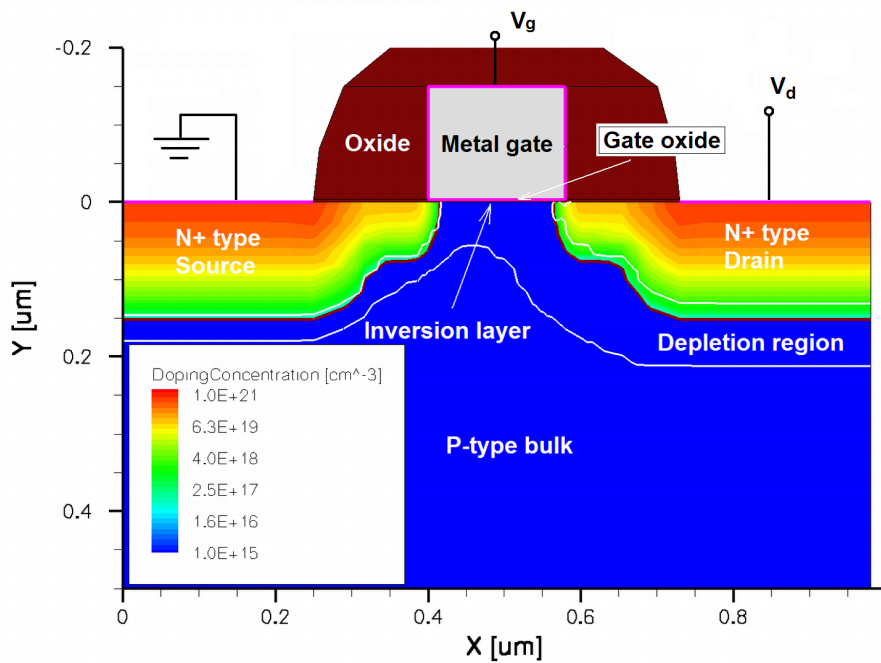
Figure 2.8: A typical 0.18 μm nMOS transistor layout model simulated in Synopsis TCAD .

pairs in the fixed space charge region of the p-n junction, which will be cleared away by the external electric field. This generates a *photo current* which can be amplified and measured by the readout electronics. Usually the p-type terminal is grounded and a bias voltage is applied to the n-terminal.

2.3.2 The MOS transistor

Nowadays the basic element of any electronic circuit is the transistor. The unipolar or metal-oxide-semiconductor field-effect transistor (MOSFET) will be described here (the other type - *bipolar* - is not relevant to the work in this thesis). Under different operational conditions the transistor can be used as a simple switch, a current source, an amplifier, a variable resistor or a capacitor. Combination of several transistors forms the basis for a digital logic. Fig. 2.8 shows

a model of a typical nMOS transistor[1]. It has four terminals: a source, drain, gate and a substrate bias contact (usually kept at ground). The structures may be formed on a moderately doped p-type silicon substrate. The source and drain are heavily doped n-type regions (*n-wells*) implanted on the substrate with a separation distance (*transistor channel*). Above the channel there is a thin silicon dioxide layer (*the gate oxide*) that isolates the gate from the substrate. In a silicon integrated circuits, a MOSFET is surrounded by a thick *field oxide* to isolate it from adjacent devices.

The MOS structure properties

The properties of the MOS structure dictate the operation principle of the MOS transistor. A simple MOS structure consists of an oxide layer grown on top of a p-type semiconductor and a metal contact placed on the oxide. The structure is equivalent to a planar capacitor with one of the electrodes replaced by a semiconductor. When a positive voltage is applied across the MOS structure, the established electric field sweeps away positively charged holes from the oxide-semiconductor interface, creating a depletion layer by leaving electrons only. If the voltage is above certain level know as the *threshold voltage*, a high concentration of electrons forms an *inversion layer* located in a thin layer next to the interface between the semiconductor and the insulator. In the transistor this layer is formed in the channel between the source and drain.

The nMOS transistor principle of operation

In equilibrium, when a voltage above threshold (V_{th}) is applied to the gate terminal (V_g), the source to drain channel acts as two back to back connected p-n junctions. If small drain voltage (V_d) is applied, the silicon beneath the gate acts simply as a resistor, and the linear relationship between the current and the voltage is obtained as shown in Fig. 2.9. As the V_d is increased the p-n junction

---

[1] pMOS transistor may be considered by exchanging p for n and reversing the polarity of the voltages.

at the drain becomes more reverse biased and the depletion region spreads out into the bulk and the channel under the gate, which eventually become closed or "pinched off". Nevertheless, the characteristic curve does not become flat and still has a small positive slope. This small increase in current can be attributed to the shortening of the effective channel length due to the growth in the "pinched off" region [18].

Fig. 2.9 shows a family of drain-to-source current curves as a function of drain-to-source voltage for different applied gate voltages. For V_g below V_{th} the region under the gate oxide is lightly populated with free electrons and only a small sub-threshold leakage current can flow between the source and the drain, which is mainly due to the thermal excitation of carriers. If V_g is fixed at some small voltage and again V_d is gradually increased, then, as the depletion layer will initially be larger, the slope of the characteristic curve will be initially smaller and the "pinch off" will occur at lower current values.

2.4   CMOS technology

The crucial reason for the success of the MOS transistors was the development of the CMOS logic. Modern CMOS technology is used in the production of microprocessors, memory, digital and analog circuits as well as imaging sensors. The technology benefits from the fabrication of nMOS and pMOS transistors on the same substrate, which gives fundamental advantages for low power consumption and high noise immunity for the entire system.

However, integrated electronics technology is very restrictive in the sense that only limited number of component types are available for implementation. All devices have to be built on a single semiconductor substrate. Only capacitors and resistors are available as passive components, while usually two transistor types can be integrated. The most common integrated circuit CMOS technology is based on MOS transistors as amplifying elements.
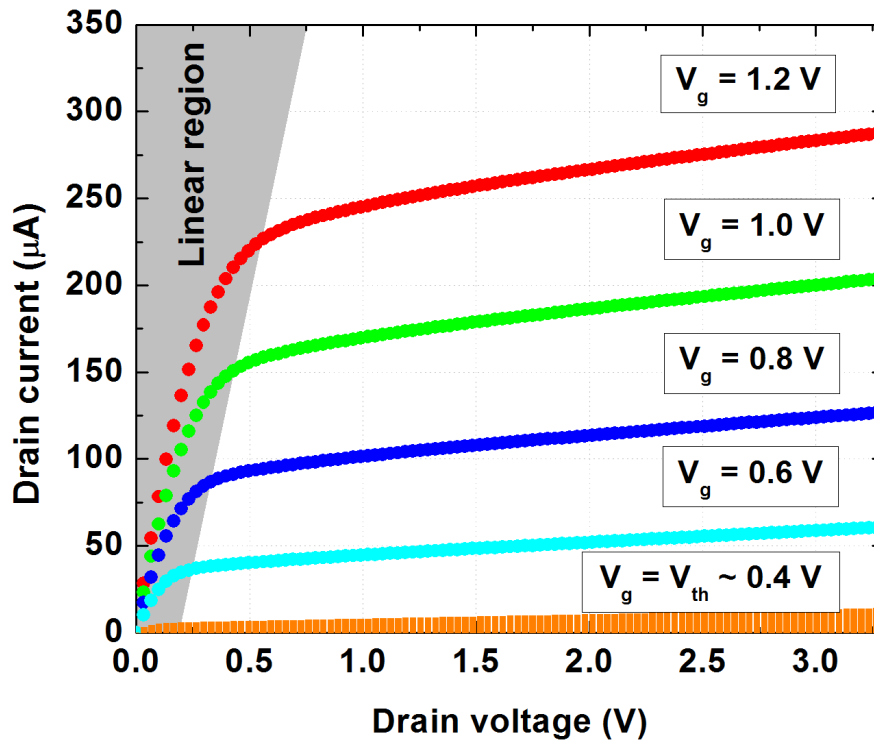
Figure 2.9: A typical 0.18 μm nMOS transistor performance characteristics simulated in Synopsys TCAD.

The main advantage of CMOS over nMOS and bipolar technology is the much smaller power dissipation. Unlike nMOS or bipolar circuits, a CMOS circuit has almost no static power dissipation. Power is only dissipated in the case, where the circuit actually switches. This allows the integration of many more CMOS gates on an integrated circuit than in nMOS or bipolar technology, resulting in improved performance and extended functionality. Besides the relative simplicity in fabrication and low-power consumption in digital applications of CMOS technology, its drawbacks are the limitation in speed and inability to drive large currents.
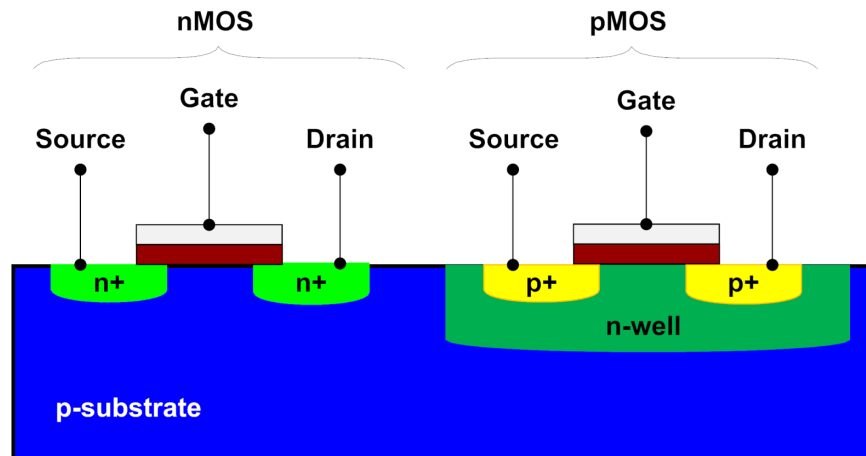
Figure 2.10: Schematic layout of a typical CMOS device.

2.4.1 Composition

CMOS electronics uses only p- and n-channel transistors as active devices. The cross section of the typical CMOS active device is shown in Fig. 2.10. These complementary transistors are insulated from each other by putting one of them into a well with opposite doping to the bulk material. Combination of such devices is extremely useful, since the same signal which turns on a transistor of one type is used to turn off a transistor of the other type, dramatically reducing power consumption. Another fundamental advantage behind it, is that such a combination allows the creation of paths to the output from either the voltage source or ground. These two concepts form the basis for CMOS digital logic.

2.5 Large scale pixellated radiation detectors

The development of position-sensitive semiconductor detector technologies have required significant development efforts in not only the optimisation of the detection materials and methods, but also in the electronics of the readout. A very large number of signal channels with high spatial density and temporal resolution have to be read out. The specific needs of the detector development were
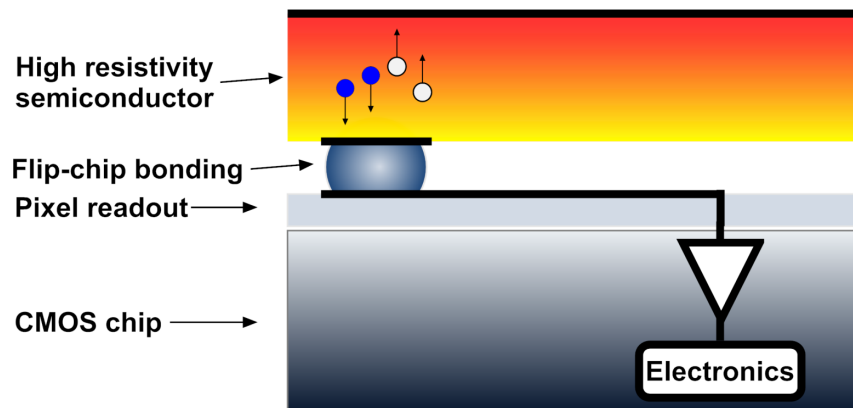
Figure 2.11: Cross section of a typical hybrid pixel detector.

low-noise analog readout, high density component integration combined with low power consumption. Therefore readout circuits are largely based on existing CMOS integrated electronics technology, which fulfils the low-noise requirements while the extensions and modifications improved radiation hardness. Below is an introduction to two such technologies.

2.5.1 Hybrid Pixel Detectors

A hybrid pixel detector technology comprises a detection medium and the readout electronics manufactured in different fabrication processes. Both parts of the detection system have a matching matrix of electrodes which are brought into contact via a standard flip-chip bonding process [23] (Fig. 2.11). Such a technology allows independent design and optimisation of the readout electronics and detection medium. Thanks to advances in CMOS technology, the readout chip can fully exploit advanced signal processing techniques on-chip. This can include amplification, energy discrimination, digitisation and post processing of the signal on the pixel level. Moreover exotic detection materials, *e.g. Ge, GaAs, CdZnTe*, can be used as a detector, which makes hybrid technology very attractive for a wide range of applications despite its relatively high fabrication costs [24, 25, 26].

2.5.2 Monolithic Active Pixel Sensors

A CMOS Monolithic Active Pixel Sensor (MAPS) is a pixellated imaging sensor, produced using a standard CMOS fabrication process. However, the wafers differ slightly from those used for electronic circuit fabrication. A high resistivity, high quality epitaxial layer of $< 20 \ \mu m$ is deposited on top of the wafer. This improves the charge collection and noise characteristics of the sensor. Such an approach found application not only for visible light imaging but also for charged particle detection [27]. There are many different MAPS architectures, which improve a particular sensor characteristic or enhance functionality. A basic sensor consists of an array of pixels each containing a photo sensitive diode, an amplifier, a reset transistor and a select transistor. The schematic in Fig. 2.12 shows the elements of such a pixel. This design is known as 3MOS pixel design. A photon or charged particle interacts with the silicon of the epitaxial layer, generating charge, which is then collected by the photo diode. The source follower transistor (M_{sf}) acts as a buffer to convert charge to voltage within the pixel. The select transistor (M_{sel}) switches the pixel to the read-out electronics. After the signal is read out from the pixel the reset transistor (M_{rst}) clears the charge from the diode by pulling it to a reset voltage. The pixel array is usually readout using a "rolling shutter" method. The pixels of row n are individually selected by the select transistor using a column shift register and the charge generated in each pixel in the row is sampled to a storage capacitor and then digitised off-chip.

The 3MOS pixel has several significant shortcomings. The bulk of the noise in the pixel is introduced during the reset phase by the reset transistor and known as the kTC noise [28]. The 3MOS pixel also exhibits high thermal dark current mainly due to fabrication damage in the n^+ contact of the photo diode. Generally CMOS MAPS pixels show non-linear outputs, which are due to the fact that the diode capacitance changes as it charges up [29].

The other most commonly used pixel architecture is referred to as a 4MOS pixel (Fig. 2.13). It features an extra switch (M_{tr}) between the photo diode and
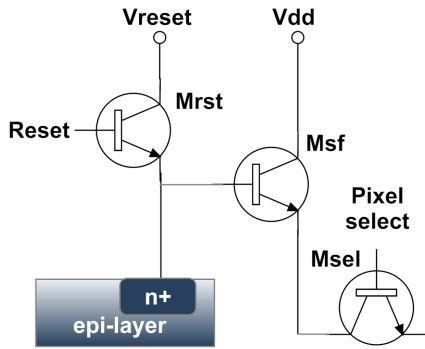
Figure 2.12: Schematic of the standard 3MOS pixel design of the MAPS.
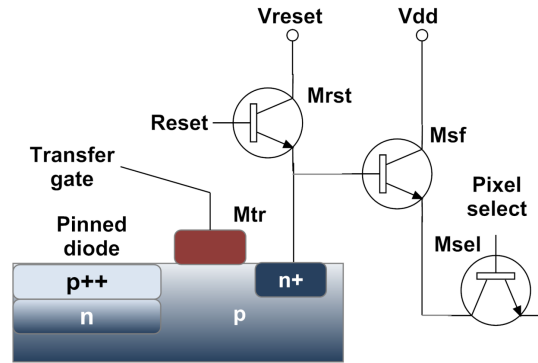
Figure 2.13: Schematic of the 4MOS pixel design of the MAPS.

the reset transistor. This design allows the reset level to be sampled just before integration, which means that the noise of the reset transistor can be subtracted. Such a technique is known as the *correlated double sampling* (CDS) . Despite tremendous noise reduction, this architecture suffers from several disadvantages. The sensors featuring 4MOS design usually use pin-diode instead of pn-diode, complicating standard CMOS process [30]. The charge capacity of the pixel is also dramatically reduced limiting the architecture to large pixel sizes.

Chapter 3

Characterisation techniques

This chapter discusses CMOS MAPS characterisation techniques. In Section 3.1 three relevant steps of image generation are described. Each of them introduces parameters of sensor that need to be assessed. Section 3.2 gives a background to a technique that employs photons in the visible wavelength range as a test stimulus for the sensor – the Photon Transfer Curve (PTC) . Finally, in Section 3.3, tests with Minimum Ionising Particles (MIPs), which are common for HEP applications, are discussed as an alternative to photonic methods. These estimate the key sensor parameters – conversion gain and signal-to-noise performance.

3.1 Image generation mechanisms

3.1.1 Charge generation

Charge generation is the ability of the sensor to intercept an incoming photon and convert it into an electric charge. This process is described by a performance parameter *quantum efficiency (QE)* and defined as

$$QE = \eta_i QE_i \tag{3.1}$$

where η_i is the quantum yield (number of e^- per interacting photon) and QE_i is the interacting QE (number of interacting photons per number of incident photons). An interacting photon is one that is absorbed by the sensor and generates e-h pairs. In order to achieve high QE response, there are three main types of photon loss to be minimised – absorption, reflection and transmission.

Absorption loss is associated with optically dead structures. For CMOS MAPSs they typically include MOSFET transistors that are incorporated into each pixel and located above the sensitive epitaxial layer. The CMOS technology also requires several metal layers above the transistors for interconnection, biasing and grounding. This typically adds an extra several microns of material above the pixel. The surface of the sensor is usually covered with a passivation layer for extra protection against physical damage. These structures can sum up to $7 - 10 \ \mu m$ of optically dead layers.

Reflection and transmission losses are inherent to the physical properties of silicon and the layer structure. Reflection losses can be significant at certain wavelengths, e.g. up to 70% at 250 nm [30]. Transmission loses are pronounced at very short (soft X-rays) or very long wavelengths (near IR), when the incoming photon passes through the sensitive epitaxial layer without interaction.

3.1.2 Charge collection

Signal charge generated in the sensor must be collected by individual picture elements (pixels). The ability of these elements to collect charge equally from the sensitive layer of the sensor greatly influences image quality. There are three main parameters to be discussed which describe this process.

The first one in the spatial variation in the sensitivity of individual pixels - *pixel-to-pixel non-uniformity*. If the sensor is uniformly illuminated, the charge level collected by the pixels will be slightly different from pixel to pixel even if all other noise sources are eliminated. These deviations are related to both imperfections in silicon wafers and fabrication process variations which define pixel

boundaries. The second parameter – *full well capacity* – refers to the maximum amount of charge which the photo diode in each pixel can hold. This depends on the pixel geometry and size as well as the epitaxial layer thickness and quality. The last one – *charge collection efficiency* – reflects the capability of the sensor to efficiently collect signal charge without loss to the neighbouring pixels. In CMOS MAPS the primary charge collection mechanism is diffusion. Due to the lack of an external field across the active volume it is inherent to the design that some of the charge generated will diffuse into neighbouring pixels. The phenomenon, known as *charge sharing*, determines spatial resolution for imaging applications and significantly complicates data analysis for HEP applications.

3.1.3 Charge measurement

Signal charge measurement is the last major operation in the image formation. After the charge is generated and collected by the photo diode, it must be converted to a voltage, amplified, measured and then digitised for readout respectively. Apart from the *photon shot noise* and pixel-to-pixel non-uniformity, all noise sources are inherent to these operations. The noise sources in CMOS MAPSs can be divided into *temporal* and *spatial*. Temporal noise refers to time-dependent fluctuations in the measured signal level that arise from fundamental processes. It can be introduced in pixels, column amplifiers, gain amplifiers and ADCs . Temporal pixel noise includes *reset noise*, *dark current shot noise* and MOS device noise. *Fixed pattern noise (FPN)* refers to a non-temporal spatial noise and is due to device mismatches in the pixels, variations in column amplifiers, *etc*.

The next section exploits techniques used to determine the parameters discussed above. Visible light is employed as a probe with its well known Poisson distributions.
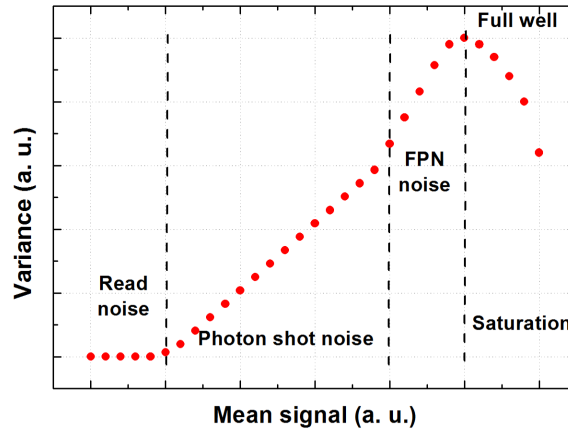
Figure 3.1: Theoretical PTC where four regions can be identified: read noise, photon shot noise dominated region, FPN noise region and saturation.

3.2   Photonic technique

The photon transfer curve (PTC) [28] is the key element of the photonic technique which provides a reliable method of estimating many of the sensor's parameters and is a valuable testing methodology employed in the design, characterisation, optimisation and application of CMOS MAPSs. It is based on the fact that the distribution of photons from a source is a Poisson process and one can use statistical methods for deriving sensor parameters. Use of the photon shot noise as a test stimulus to the camera is very convenient as characteristics of the Poisson distribution are well known. A plot of the mean number of photons against the variance gives a linear dependence. Assuming that the sensor gain is not affected by the illumination level, one can say that any deviation from the straight line is caused by the sensor (Fig. 3.1). There are four regions that can be identified on the PTC plot for an imaging sensor. The read noise region is represented by the flat region and associated with the sensor and its readout electronics. It is pronounced when there is no incident light on the sensor. As the input
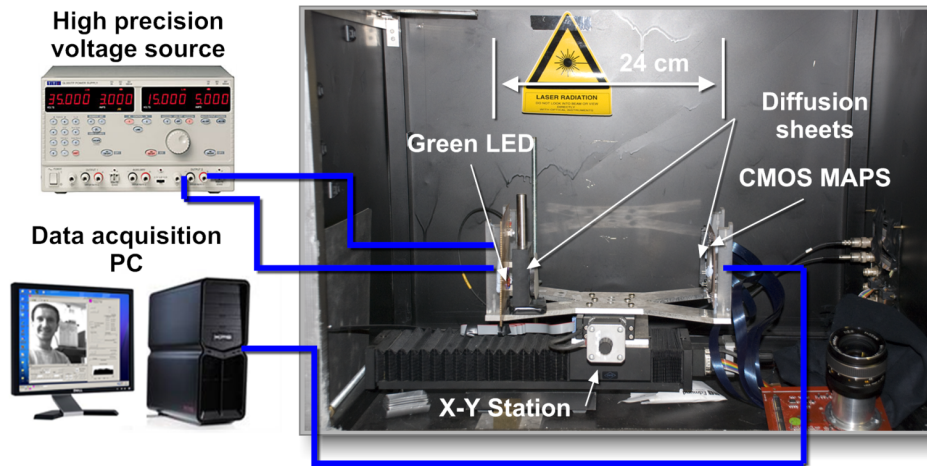
Figure 3.2: Diagram of the PTC setup.

light amplitude level increases, the noise becomes dominated by the photon shot noise. It obeys the Poisson statistics and therefore the signal is proportional to the variance. The fixed pattern noise dominates at high illumination levels. It results from differences and non-uniformities in the pixels, which may reach saturation at different light intensities giving rise to signal deviation. The variance of the signal drops, when nearly all pixels in the sensor saturate.

3.2.1 Experimental setup

The diagram of the experimental setup is shown in Fig. 3.2. The sensor is mounted on a X-Y station in order to tune its position and placed in a light tight box. A green Light Emitting Diode (LED) is positioned several centimetres from the sensor. Two diffusion sheets in front of the sensor and the LED ensures uniform sensor illumination across its area. The distance between the diffusion sheets is set to 24 cm for the purpose of keeping the ratio of the distance between the sheets, S_d, to the sheet diameter, S_a, equal to value of 8, $S_d/S_a = 8$, as suggested in [31]. The LED is connected to a mV precision voltage supply which is controlled by a data acquisition PC. For QE measurements the LED can be replaced with a monochromator.

3.2.2 Gain

The photon transfer method of gain estimation is valid only if the following assumptions hold:

- Fluctuations in the number of incident photons and generated electrons follow a Poisson distribution;

- The sensor output is linearly proportional to illumination;

- The variance of the conversion gain is small;

- Noise sources in the sensor are uncorrelated;

For a linear sensor, the electron to digital number conversion gain G (e^-/DN) is constant. An interacting photon results in an input P_I producing a signal S (DN)

$$S = \frac{P_I}{G} \tag{3.2}$$

Photons of wavelengths greater than 400 nm generate one e-h pair in silicon, therefore the mean output signal, $\bar{S}$, is proportional to the mean number of primary signal electrons, $\bar{N}$,

$$\bar{S} = \frac{\bar{N}}{\bar{G}} \tag{3.3}$$

The variance of the generated signal can be found using the propagation of errors formula

$$\sigma_S^2 = \left(\frac{\partial S}{\partial N}\right)^2 \sigma_N^2 + \left(\frac{\partial S}{\partial G}\right)^2 \sigma_G^2 \tag{3.4}$$

Assuming Poisson distribution of generated photo electrons ($\sigma_N^2 = \bar{N}$) and negligible gain variance ($\sigma_G^2 << \sigma_N^2$) one can derive the following equation in the photon shot noise limited region

$$G = \frac{\bar{S}}{\sigma_S^2} \tag{3.5}$$

The data for the gain calculation is taken as follows. N full frames ($L \times M$ pixels) are taken at zero illumination level and the mean dark offset value and variance are calculated using the following equations
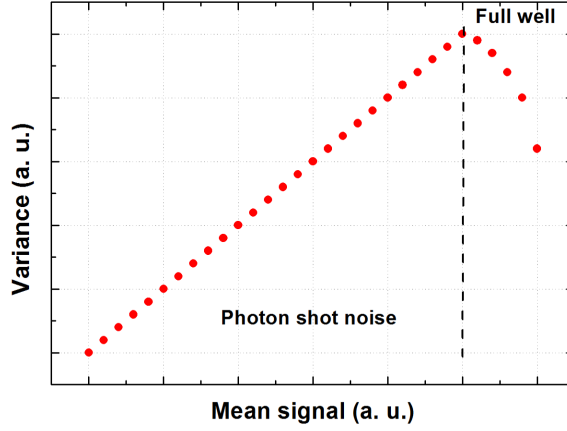
Figure 3.3: Theoretical photon transfer curve for an imaging sensor with the fixed pattern noise and read noise components removed.

$$\bar{S}_{i,j} = \frac{1}{N} \sum_{n=1}^{N} S_{i,j,n} \qquad\qquad \sigma_{i,j}^2 = \frac{\sum_{n=1}^{N} S_{i,j,n}^2}{N} - \bar{S}_{i,j}^2 \qquad (3.6)$$

$$\bar{S}_{dark} = \frac{1}{LM} \sum_{i,j}^{L,M} \bar{S}_{i,j} \qquad\qquad \sigma_{dark}^2 = \frac{1}{LM} \sum_{i,j}^{L,M} \sigma_{i,j}^2 \qquad (3.7)$$

Sets of two frames are then taken for a number of illumination levels from nearly dark to camera saturation level. The two frames are then subtracted from each other pixel by pixel. This eliminates fixed pattern variations since these are present in both images. Therefore the shot noise limited region is extended to the point of full well. The mean and the variance of the signal frames are then calculated as for the dark frame using Eq. 3.7. Subtraction of the dark offset and dark offset variance gives the plot for the determination of the camera gain constant (Fig. 3.3).

The graphical method for estimation of the gain is accurate to within $10 - 20\%$ [32], depending upon how well the line is fitted to the data points. It provides

a rather quick and robust way of presenting many parameters of the sensor in absolute units.

However, the average gain estimation approach gives no information about uniformity across the sensor matrix. This drawback can be overcome by plotting the PTC for each pixel in the sensor array. The dark and signal pixel mean and variance are calculated as described using Eq. 3.6. There is no need to subtract two frames taken at the same illumination level as the pixel to pixel non-uniformity does not affect the PTC in this case. If the dark mean and dark variance is subtracted from the signal, a series of PTCs similar to the one shown in Fig. 3.3 can be plotted. Fitting the shot noise limited region of each of them with the straight line results in the camera gain constant calculated per pixel and is usually presented in the form of a histogram.

To achieve better precision in comparison to the averaged PTC, not less than $N = 100$ frames per illumination level should be accumulated. For a sensor with 640×480 pixels and 10-bit ADC precision, one needs $0.6\ Mb$ per frame. Taking into account at least 50 illumination steps, the data accumulated over a typical pixel by pixel PTC run easily exceeds several gigabytes of storage and requires extensive computational resources for analysis.

3.2.3   Full well capacity and dynamic range

Full well capacity (FW) is the measure of the maximum amount of charge that a pixel can hold without sharing it with adjacent pixels. It can be determined from the conventional PTC. When the light intensity is increased, the charge in a saturated pixel is collected by neighbouring pixels which also become saturated. Therefore the variance reduces. The signal level at which the variance reaches a maximum on the PTC graph determines the full well capacity of the sensor and is expressed in electrons.

Dynamic range (DR) is the ratio between the brightest and faintest objects that can be simultaneously discriminated. Therefore, it is determined by the full

well capacity, $S_{FW}(e^-)$, and the read noise, $\sigma_R(e^-)$, floor and usually expressed in decibels (dB) in the following form

$$DR = 20\log\left(\frac{S_{FW}}{\sigma_R}\right). \tag{3.8}$$

3.2.4 Linearity

Charge that is generated and collected in the pixel should be proportional to the number of interacting photons. However, there are several factors that make the response of the sensor non-linear. Two fundamental types of non-linearity exist for CMOS MAPSs – *sensitivity non-linearity* and *gain non-linearity*. Sensitivity non-linearity is associated with the photo diode capacitance that varies with the amount of charge stored in the well. The potential on the source follower gate, V_g, is the ratio of the charge on the photo diode, Q_d, and the capacitance of the photo diode, C_d (see Section 2.5.2, page 28). As the photo diode charges up the capacitance increases, therefore the charge to voltage conversion factor reduces, resulting in a non-linear response. Gain non-linearity is fundamentally associated with the source follower transistor gain characteristics (see Section 2.3.2, page 22).

The linearity can be measured using two methods. In the first method the sensor in illuminated in the shot noise limited region just above the dark level. A series of measurements are taken without resets between the frames. Since the additional charge between each frame remains the same because of the constant illumination and integration time, any deviation from the linear dependence on the "signal vs. frame #" graph indicates a non-linearity.

For the second method, the sensor is illuminated for a constant integration time, gradually increasing the intensity of the source from near dark level to saturation. If the LED chosen for the experiment responds linearly with applied voltage, the non-linearity of the sensor can be estimated by plotting number of generated electrons vs. number of emitted photons.

The first method of the linearity estimation is preferred as it does not require the LED to be perfectly linear with the applied voltage, the LED absolute pho-

ton yield is not required which avoids the usage of the calibrated photo diode. However, not every sensor provides the necessary functionality on the firmware level to make such a measurement possible.

3.2.5 Temporal Noise

Temporal noise refers to time-dependent fluctuations on the signal level. It can be both of fundamental origin or poor design and fabrication quality. Temporal noise can be introduced in the pixel, column amplifier, ADC or the external circuitry.

Shot noise

Due to the quantum nature of light, there is an uncertainty in the number of photons hitting the surface of the sensor. The number of photons incident in the given observation time window on the sensor is known to follow the Poisson distribution, where the mean number of arrived photons is equal to its variance. The photons that interact in the sensor generate *electron shot noise* which also follow the Poison distribution and is proportional to the quantum yield η. This is a fundamental noise source and cannot be eliminated.

Reset noise

The signal integrated on the photo diode of a pixel is measured relative to its reset level (see Section 2.5.2, page 28). Reset noise is associated with the characteristic of the reset transistor in the pixel. It is thermally generated by the channel resistance due to the uncertainty in the capacitance of the sense node [33]. As a result, the sense node voltage is slightly different each time the pixel is reset. The reset noise, σ_{rst} (rms V), on the sense node is given by [18]

$$\sigma_{rst} = \sqrt{4kTR_RB} \tag{3.9}$$

where R_R is the effective channel resistance, B is the noise power bandwidth, T and k are temperature and Boltzmann constant respectively.

According to [28], $B = 1/4RC$. Substituting noise power bandwidth equation into 3.9 gives

$$\sigma_{rst} = \sqrt{\frac{kT}{C}} \tag{3.10}$$

In units of rms noise electrons, taking into account that $V = e/C$, the reset noise can be expressed as

$$\sigma_{rst}(e^-) = \sqrt{\frac{kTC}{e}} \tag{3.11}$$

where e is the elementary charge.

The reset noise is also known as the "kTC" noise and refers to both Eq. 3.10 and Eq. 3.11 depending on the context.

Column amplifier noise

The column amplifiers sample the pixel signal and then buffer and/or amplify it. Major noise sources are the kTC noise associated with the sample and hold capacitors and the thermal and 1/f noise of the column amplifier MOS devices. At the same time column amplifier noise also contributes to the fixed pattern noise as the column components cannot be perfectly matched during fabrication.

3.2.6   Fixed pattern noise

Fixed pattern noise refers to a non-temporal spatial noise. It is due to device mismatches in the individual pixels and variations across the column amplifiers.

Pixel response non-uniformity

Pixel response non-uniformity (PRNU) is a quantitative measure of the fact that not all pixels have the same response to the incident light. This comes from the variations in doping concentration of the silicon wafers as well as mask misalignments during the many fabrication steps. These issues have been addressed by

the sensor designers as well as the fabrication foundries resulting in the PRNU being negligible in comparison to other noise sources.

Gain fixed pattern noise

The source follower transistor gain also varies from pixel to pixel generating gain FPN. This component of the noise is signal level dependent and varies with illumination. Unlike photon shot noise, which varies as a square root of the photon flux, the gain FPN is proportional to the signal. It means that the gain FPN dominates the photon shot noise over a large fraction of the sensor dynamic range. Gain FPN does not change as a function of time and can be characterised, assuming a linear pixel response, for each pixel. Pixel by pixel gain distribution and the standard deviation of the pixel gain divided by the mean pixel gain gives a quantitative estimation of the gain uniformity

$$\sigma_{GainFPN} = \frac{\sigma_G}{G} \tag{3.12}$$

3.2.7 Dark current

Dark current occurs through the thermal generation of minority carriers and is intrinsic to semiconductors. The amount of dark current produced varies from pixel to pixel, which also contributes to the read noise in a form of dark current shot noise and dark current fixed pattern noise. The shot noise component is given by

$$\sigma_{DCshot} = \sqrt{DC} \tag{3.13}$$

where DC is the average dark current (e^-) proportional [30] to

$$DC \propto t_{int} \cdot S_{pix} \cdot T^{3/2} \cdot e^{-E_g/2kT} \tag{3.14}$$

where t_{int} – integration time, S_{pix} – pixel area, T – the operating temperature, E_g and k are the silicon band gap energy and Boltzmann constant respectively.

Dark current in the form of leakage current originates from several places in the pixel. This includes bulk and epitaxial silicon, back and front surfaces of the sensor.

In practise dark current is measured using the following technique. A series of N dark measurements at room temperature are taken setting integration times in the range between minimum possible and up to tens of seconds with two frames each. The pedestal and gain variations are removed by subtracting two adjacent frames at each integration time. The remaining signal is then dominated by the dark current, which is averaged over the array of pixels. The dark current is found by calculating the slope of the best fit line to the plot of signal in e^- against integration time in seconds. The dark current is typically normalised per cm^2.

3.2.8   Read noise

Read noise is sometimes referred to as the total noise at the output of the system. It is given by the quadratic sum of all noise components excluding photon shot noise. These include the components described above as well as random fluctuations in electronics and external power supply induced elements which can degrade the overall performance of the system.

3.2.9   Quantum efficiency

Quantum efficiency of the sensor can be measured only if the light source output is known. The setup for QE is similar to one shown in Fig. 3.2. The LED is replaced by the deuterium light source (Hamamatsu L7893) and the monochromator (Jobin Yvon H20).

The output of the light source system which includes the deuterium light source, two optical fibres, the monochromator and the intensity attenuator is unknown and requires precise calibration in order to quantify absolute output in photons per second per unit area. A high quality calibrated silicon PIN photo diode (Hamamatsu S1336) was used for this purpose. The manufacturer pro-

vided the standard diode responsivity curve, SR (A/W), that covers the near UV (200 nm) to the near IR (800 nm) range. The curve establishes a direct relationship between the incident light power and the photo diode current. The quantum efficiency of the sensor under test is related to the responsivity of the calibrated photo diode through the relationship[1]

$$QE = \frac{hc}{\lambda e} \frac{A_{diode}}{A_{sensor}} \frac{S_{sensor}}{I_{diode}} \frac{1}{t_{int}} SR \tag{3.15}$$

where hc is the product of Planck's constant and the speed of light, λ is the wavelength, e is the elementary charge, A_{diode} and A_{sensor} are the active area of the photo diode and the pixel (including fill factor correction), S_{sensor} and I_{diode} is the sensor and diode response in e^- and e^-/sec respectively, t_{int} is the sensor integration time.

3.2.10   Signal-to-noise performance

The quantitative comparison of the amplitude of the signal to the background noise defines signal to noise ratio (S/N) of the imaging system. The PTC data provides direct access to this performance parameter. S/N is determined by dividing each signal data point by the corresponding noise of the sensor. The result is usually expressed in decibels (dB) and presented in a form of "S/N vs. Signal" plot calculated using the following equation

$$SN = 20 \log \frac{S}{\sigma} = 20 \log \frac{S}{\sqrt{\sigma_{read}^2 + \sigma_{shot}^2 + \sigma_{FPN}^2}} \tag{3.16}$$

where σ_{read}, σ_{shot}, σ_{FPN} are read noise, shot noise and fixed pattern noise components respectively, S is the signal in e^-.

High signal to noise performance is important especially for low contrast imaging. The S/N can be increased using a flat-field correction technique. This is achieved by reducing the fixed pattern noise component and hence the overall read noise.

---

[1]Quantum yield η for the range of wavelengths used equals 1

3.2.11 Flat field correction

As was discussed earlier in this chapter each pixel in the sensor matrix has a slightly different response to incident uniformly distributed light as compared to neighbouring pixels. *Flat-fielding* is a technique that in use to correct for these pixel-to-pixel variations by dividing the gain variations out of an image, therefore flattening the relative response for each pixel. It is important to take into account that response characteristics strongly depend on such parameters as ambient temperature, filters and lenses used, light wavelength, *etc.* Therefore, flat-field calibration is needed each time the setup is modified or new set of data is being taken, which imposes difficulties on the actual measurement.

This simple algorithm can remove FPN and achieve the shot noise limit, significantly improving signal to noise performance. The image processing is based on the following linear equation

$$S_i^{COR} = \mu^{FF} \frac{S_i^{RAW}}{S_i^{FF}} \tag{3.17}$$

where S_i^{COR} is the corrected i-th pixel value, μ^{FF} is the average flat-field signal, S_i^{RAW} and S_i^{FF} are the uncorrected and the flat-field pixel values respectively.

The flat field image is usually taken as follows. The integration time of the sensor is set to several seconds. Two diffusion sheets are placed between the sensor and the LED light source to illuminate the sensor as uniformly as possible. The PTC setup described earlier is well suited for this purpose. The LED intensity is chosen such that the average sensor response is roughly equal to the level where the sensor goes from the shot noise limited region to the FPN region (see *e.g.* Fig. 3.3). Several frames are then accumulated and the mean frame is calculated, which ensures averaging across random noisy pixels that can occur.

In some rare applications, where the object being captured is steady during frames acquisition, simple pixel by pixel frame subtraction could be the most elegant approximation for FPN removal as was demonstrated for the PTC gain estimation technique (see Section 3.2.2, page 35).
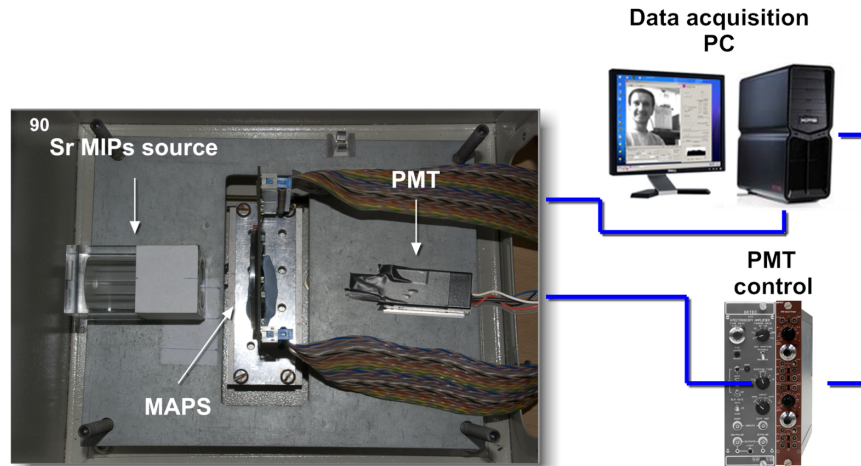
Figure 3.4: Diagram of the MIPs setup.

3.3   Minimum ionising particles

A great interest in CMOS MAPS exists not only for applications using visible light. The key characteristics of the technology, *e.g.* relatively low cost, low power consumption, increased functionality and in-pixel intelligence make these sensors very attractive for particle physics experiments and for tracking applications in particular. It was shown that MAPS fabricated in standard VLSI CMOS process demonstrate an excellent performance [27].

Several conventional detector characterisation techniques for charged particles detection were developed over decades. Some of them can be adapted for CMOS MAPS testing. The use of Minimum Ionising Particles (MIPs) as a test stimulus is one of them and has become a standard. The behaviour of these particles in the detector is well understood, therefore they can be used to evaluate the performance parameters of the detecting system based on MAPS.

3.3.1   Experimental setup

The experimental setup is shown in Fig. 3.4 and is similar to one for the PTC measurement. The sensor is placed in the middle of the light tight box. A

^{90}Sr source is put in front of the sensor and the Photo Multiplier Tube (PMT) with scintillator is located behind the sensor. The MIPs emitted from the source traverse the active area of the sensor and hit the PMT. The PMT in turn generates a trigger pulse and sends it to the sensor. The frames are accumulated as a response to the trigger signal and are stored in the PC for the analysis. The essential parameters that are to be investigated include the sensor gain and the signal to noise performance.

3.3.2 Gain

A relativistic charged particle releases only a fraction of its energy in a thin layer of matter, it generates typically 80 electron-holes pairs per micron in silicon [27]. If the depth of the sensitive epitaxial layer is known, the conversion gain, $G(e^-/ADC)$, of the pixel can be estimated using the following equation

$$G = \frac{dq}{S} \tag{3.18}$$

where d is the depth of the epitaxial layer, q is the charge generated per unit distance, S is the sensor signal in ADC.

However, depending on the geometry of the device and the relative position of the impact point, the charge can be shared between two or more pixels. This can complicate the charge collection per pixel and requires a cluster analysis algorithm to be applied in order to efficiently measure charge generated from each particle. It is also known that the traversing particle creates electron-hole pairs in the bulk, which can diffuse back to the sensitive layer and be collected [34]. This phenomenon has not been quantitatively estimated yet and contributes to the uncertainty of the gain estimation using the MIPs characterisation technique.

3.3.3 Signal-to-noise ratio

The signal to noise characteristic is similar to that explained earlier (see Section 3.2.10, page 43) and is defined as the ratio between the signal generated by

the traversing MIP and the read noise floor

$$S/N = \frac{S}{\sigma_{read}} \tag{3.19}$$

The S/N is calculated for each cluster identified and the result is presented in the form of a histogram.

Chapter 4

Active Pixel Sensors

This chapter is devoted to the comprehensive characterisation of three active pixel sensors. Section 4.1 evaluates CMOS MAPS designed with HEP applications in mind – HEPAPS4. Extensive optical and particle techniques are employed in order to optimise the performance of the sensor and understand the technology potential. In Section 4.2 a next generation general purpose technology evaluation sensor – Vanilla – is described. The key parameters of the sensor are characterised using the photon transfer technique. The last Section 4.3 evaluates the most recent parametric sensor – eLeNA – designed to evaluate noise reduction architectures.

4.1 HEPAPS4

High Energy Physics Active Pixel Sensor (HEPAPS4) [35, 36] is the fourth generation in a series of MAPS developed at RAL. It is based on the most promising test structure from the parametric sensor HEPAPS2 [37, 38]. The sensor is designed for high efficiency (100%) detection of minimum ionising particles. The sensing part of the sensor consists of 1024×384 pixels with 15 μm pitch and 20 μm epitaxial layer thickness. The sensor is organised in two halves, left and

right. In addition two rows are addressed simultaneously by one shift register. Hence there are four outputs that are readout at the same time (Fig. 4.1). The pixel array is read out using the "rolling shutter" method in two steps. The pixels of row n are individually addressed by the select transistor via a column shift register and the signal generated in each pixel in the row is sampled to a storage capacitor (two per column). The readout loop multiplexes the voltage from the capacitors through the 4-to-1 multiplexer to the off-chip ADC, where the voltage on the capacitors is digitised and stored in the DAQ card memory. After the sampling, the pixels in row n are reset and then the pixels in the row $n + 1$ are sampled.

4.1.1 The HEPAPS4 acquisition system

Pixel design

The HEPAPS4 sensor features the standard 3MOS pixel design. It was produced in three variants with different configurations of sensing element and transistor layouts. They are referred to as "D1", "D2" and "D4". The "D1" version has one n-well 1.7×1.7 μm diode with enclosed geometry transistors (EGT) [39] . It has been proven that employing novel transistor design techniques helps to improve the overall radiation tolerance of sensors fabricated in a commercial CMOS process (see *e.g.* [40]). Conventional transistors under ionising radiation suffer from parasitic source-to-drain edge leakage currents as well as from field oxide radiation induced parasitic currents. EGTs eliminate the oxide edge between source and drain of the transistor giving improved radiation tolerance. The "D2" (3.0×3.0 μm diode size) and "D4" (1.7×1.7 μm diode size) versions benefit from two and four photo diodes connected in parallel respectively in addition to the standard pixel design. By using several diodes connected in parallel inside a pixel, it is possible to improve the radiation hardness of the sensor by making the charge collection more uniform across the pixel [41]. However, the total

capacitance of the pixel increases with the number of diodes and reduces the charge-to-voltage conversion efficiency which affects the gain.

Pixel addressing

The addressing of pixels is controlled by three shift registers: one for the rows and two for the columns. The row register is 512 cells long so two rows are addressed at the same time. Signals from the pixels in these two rows are addressed through two readout lines, one for the even-numbered rows and the other for the odd-numbered rows. Column-wise the sensor is organised as two halves, each with a 192-cell long shift register and a separate output amplifier. These two registers are clocked in parallel. The floor plan of the sensor is shown in Fig. 4.1. The sensor is read out as follows: two column tokens enter the outermost part of the sensor and run towards the centre of the chip while the row token selects the first two rows. So the first columns to
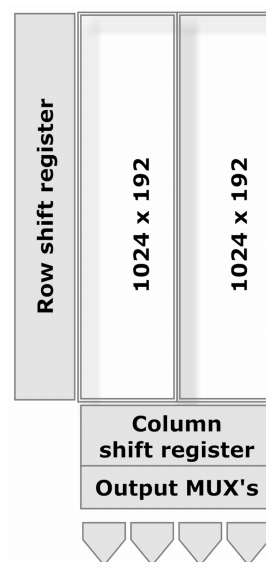
Figure 4.1: HEPAPS4 readout floor plan.

be clocked out are the two most outer columns to the left and right respectively. When the first two rows are read out, the row register selects the next two rows and the columns are clocked out again.

Readout control

The architecture of the sensor readout is shown in Fig. 4.2. The basic pixel operation is described in Section 2.5.2, page 28, and common to all 3MOS pixel design sensors. The row register enables M_{sel} and M_{rst} transistors. It is controlled by the timing parameter Row Sample Duration (RSD). The potential on the Sampling Capacitor during the enable time charges up the one on the M_{sf} transistor of the selected pixel. When all the pixel signals from one pair of rows are sampled
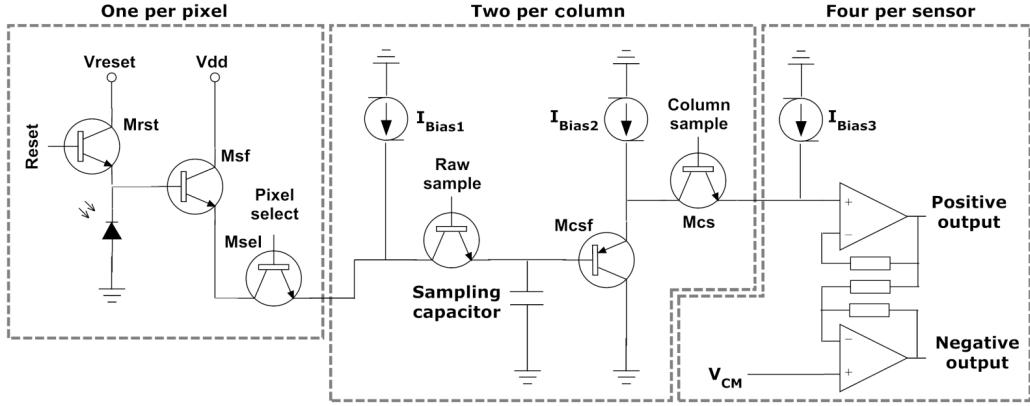
Figure 4.2: Detailed sensor readout architecture.

on the corresponding capacitors, the column shift register enables the Column Sample transistor, M_{cs}, which passes the signal from the Sampling Capacitor to the Differential Amplifier through the Column Source Follower transistor, M_{csf}. The M_{cs} transistor is active for the amount of time controlled by the Column Sample Duration (CSD) parameter. The signals from four differential amplifiers are then multiplexed to the ADC. The multiplexing time can be controlled by the MUX Wait Duration parameter (MWD).

The M_{cs} transistor is controlled by two current sources in parallel, I_{bias2} is in every column, while I_{bias3} is one per output. The only purpose of the I_{bias2} source is to keep the M_{cs} powered when it is not read out in order to minimise switching time from one column to another. Each of the differential output amplifiers is biased by the current source I_{biasA} and a V_{casc} voltage. The differential common mode offset voltage is controlled by the V_{CM}.

Data Acquisition System

The Data Acquisition (DAQ) system for the HEPAPS4 chip consists of a PC with a PCI DAQ card, a driver board and header board hosting the chip. The core components of the DAQ card are two FPGAs , I/O drivers, 128Mb of memory and the PCI interface. The DAQ generates all the necessary control signals, accepts external triggers (if enabled), reads in the data from the ADC and transfers data
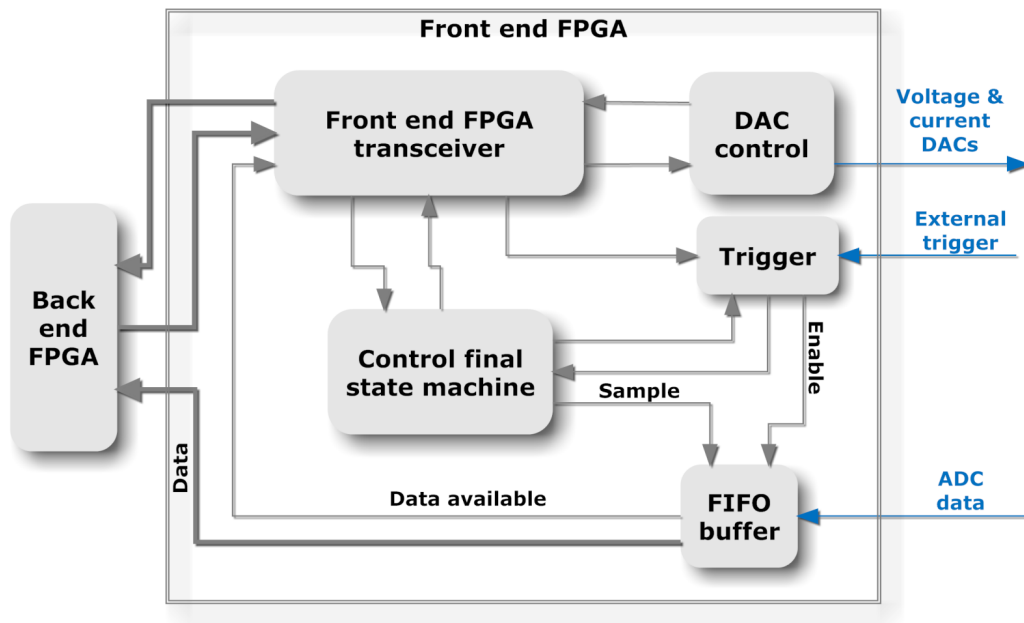
Figure 4.3: A principle block diagram of the front end FPGA for the HEPAPS4 sensor.

to RAM on the PCI card. The first FPGA - the front end FPGA - generates the control signals and samples the data to a 256 pixel deep FIFO buffer. The back end FPGA writes the data to the memory buffer and manages the communication with the PC, both for control commands and data flow. The driver board has voltage regulators, signal repeaters and the ADC. The header board hosts the HEPAPS4 chip and a multiplexer which drives four data outputs to the ADC.

FPGA firmware

The HEPAPS4 sensor is controlled by two dedicated FPGAs, which handle control signals, output data and communication with the PC. The code for the back end FPGA was reused from the previous HEPAPS2 sensor. The front end FPGA code was tailored to HEPAPS4 and new features were implemented. Fig. 4.3 shows the simplified schematic of the key blocks of the front end FPGA. It consists of the following elements:

- Control finite state machine (FSM) is the core element of the firmware

architecture. It maintains control signal flow to the chip and ADC, handles the data stream from the chip to the FIFO buffer and controls other blocks of the firmware.

- The FIFO buffer accumulates data packets and when the data frame becomes available sends a "data available" strobe to the front end FPGA transceiver block.

- The front end FPGA transceiver block functions as a communication bridge between the two FPGAs. It has internal registers for configuration parameters. The transceiver block is also in charge of the data flow management between the back end FPGA with DAC control and the external trigger block.

- The back end FPGA is responsible for data exchange between the front end FPGA and DAQ memory. The interface communication between the DAQ card and the PCI bus is also maintained by this block.

- The DAC control block sets appropriate voltages on bias and current generators via off-chip digital-to-analog converter.

- The Trigger block enables the sensor to work with an external trigger.

There are several readout modes implemented in the HEPAPS4 DAQ system. They can be grouped into operation with and without an external trigger, region of interest readout (ROI), test pattern generation, and operation in three reset modes: normal, CDS1 and CDS2.

Normal readout mode. The HEPAPS4 sensor operates in the rolling shutter mode, where the readout is cycling through the chip continuously to clock out and reset each pixel. The pixels accumulate charge from light and leakage current, so after an idle period the pixels are saturated and require a series of reset cycles skipping the integration to bring them to stable operating conditions. This is controlled by the "Num Resets" parameter in the acquisition software

(see Section 4.1.1, page 57). The timing parameters of the sensor are set by the internal register values. The integration time of the sensor can be varied utilising an idle phase between frames controlled by the "wait between frames" (WBF) parameter. The WBF defines the wait time between minimum possible integration time plus the reset duration and the read out cycle of the following frame. The reset length is controlled by the "row reset duration" (RRD) register. The FSM controlling the read-out sends a read-out strobe to the input FIFO which tells it to latch the data into the FIFO buffer. This data is then written to the DAQ memory. After the pair of rows is read out to the buffer, the reset occurs and the cycle continues. The read out cycle can run until the DAQ memory is filled up. 128 Mb of memory is available for data storage. It can accommodate up to 85 full frames per acquisition run.

Correlated Double Sampling (CDS) mode 1. The off line CDS is implemented in order to study the influence of a reset noise. In this mode the sensor is reset only for the first several frames at the beginning of the acquisition cycle (defined by "Num Resets") while other frames are accumulated without resetting between frames. By subtracting two consecutive frames the reset noise is eliminated (See Section 2.5.2, page 28). This mode is used mainly to analyse the linearity of the sensor (as discussed in Section 3.2.4, page 38). The data accumulation for noise analysis is inconvenient as only two frames from the run can be used. This requires multiple runs to be conducted in order to gain enough statistics. The CDS2 mode was implemented to tackle this restriction.

Correlated Double Sampling (CDS) mode 2. A second variant to study noise of the sensor. In this mode resets are only issued for even frames. Hence the reset noise can be eliminated by subtracting two adjacent frames in the offline CDS. These frames later can be used to calculate sensor noise from one acquisition run.

Region of Interest (ROI) readout. A fraction of the pixel array readout was implemented in the firmware. The ROI mode is useful to either speed up
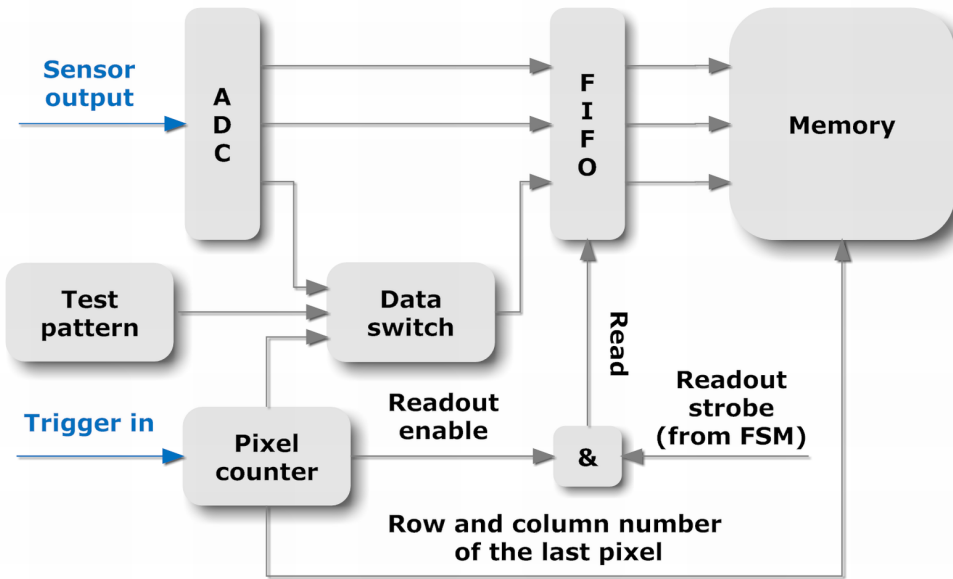
Figure 4.4: A block diagram of the trigger logic of the HEPAPS4 DAQ.

the read out or increase number of frames recorded per acquisition run. There are some constraints on how the region can be selected due to the way the rows and columns are addressed in the chip. As the sensor is arranged as two halves (see Section 4.1.1, page 50), the ROI must be centred with respect to the middle column. It is defined by the first and last row as well as by the width of the region.

Trigger mode. The firmware provides the facility to operate the DAQ in a mode with an external trigger. The triggering concept is schematically shown in Fig. 4.4. In this mode, the signal from an external trigger goes to the pixel counter block, which keeps track of which row and column is currently being read out. The pixel counter writes the row and column number of the pixel read out at the time the trigger arrives to the memory. This allows the software, which parses the data, to reconstruct the frame correctly. Then the pixel counter raises a readout enable signal which is combined with the readout strobe from the FSM. The enable signal is kept high until the rolling shutter readout reaches the pixel preceding the first pixel read out, then the signal goes low until the next trigger arrives. The parameter "Num trig frames" can be used to enable accumulation

2	6	...	762	766	764	760	...	4	0
3	7	...	763	767	765	761	...	5	1
...	...	...	...	...	...	...	...	...	...
392450	392454	...	393210	393214	393212	393208	...	392452	392448
392451	392455	...	393211	393215	393213	393209	...	392453	392449

Table 4.1: The order of the pixels as they are read out to the HEPAPS4 DAQ memory.

of more than one frame per trigger.

Firmware test patterns. To verify the chain of data acquisition and data decoding at the stage of firmware and DLL middleware debugging, test patterns can be generated and read out instead of sensor data. There are four different test patterns that can be selected: a row number, column number, multiplexer setting and a fixed test pattern. In the row and column modes the data for each pixel is replaced by the address of the shift register that corresponds to the current row or column. In the multiplexer mode the position of the multiplexer is read out. The fixed test pattern makes the hexadecimal value "B0B" written as a pixel value.

DLL middleware

The data from the ADC for each pixel is written to the memory bank of the PCI DAQ board. The 14 bit ADC value and the out-of-range bit are written in a 16 bit word for each pixel. The ADC values are associated with each pixel by their location in the memory. The values are written sequentially to the memory in the order they are addressed by the shift register FIFOs as was described in Section 4.1.1, page 50. Table 4.1 shows the order in which the pixels are read out and therefore their order in the memory.

The pixel values have to be reordered to form an image when the data is read out from the DAQ memory. This functionality was implemented in a dedicated middleware in the form of a Dynamic Link Library (DLL). The DLL handles communication between the DAQ card driver and the control program. The
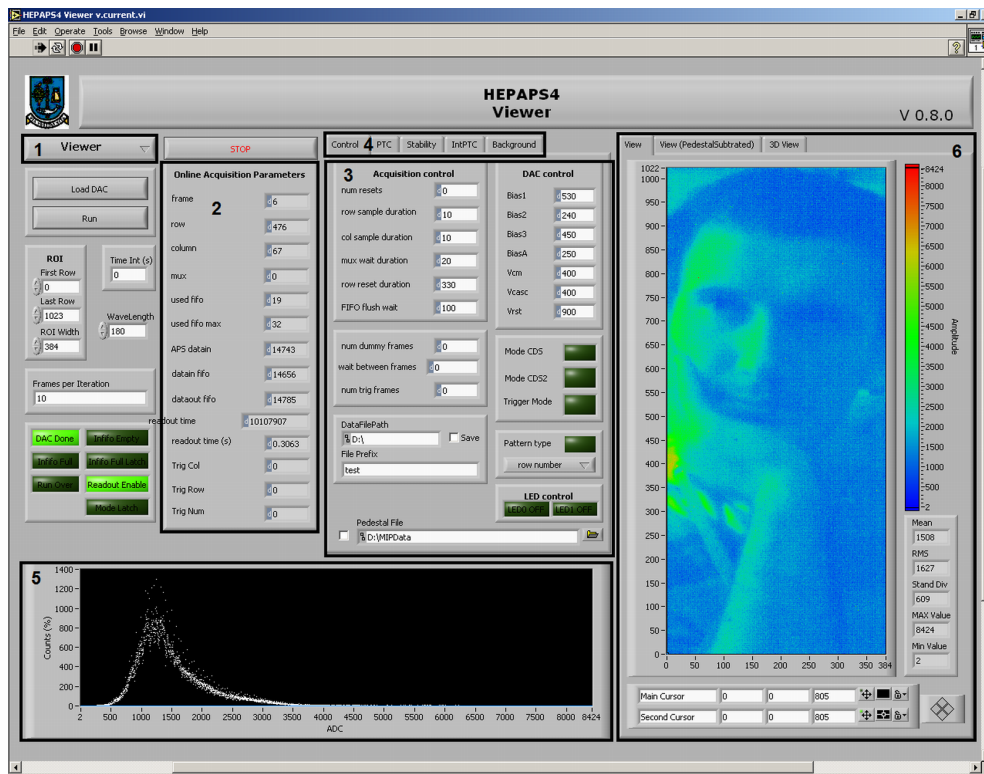
Figure 4.5: The HEPAPS4 Viewer application provides access to all functions of the sensor and online acquisition parameters.

program sends the control signals to the DAQ memory, which is read by the back-end FPGA. The sensor responds according to the control signals sent and writes the acquired data to the memory. The DLL reads the data from the DAQ memory and reorders it to form image frames. It also generates the appropriate header information containing all the parameters used for data acquisition. The data and header from each acquisition run is written to an output file on the PC for analysis.

Control and data acquisition software

The front end part of the data acquisition was designed and implemented in Labview 7.1 package [42]. It provides a user friendly interface to access the sensor control parameters and serves as a framework for different experimental setups. Such an approach allows fully automated experiments to be carried out

with several independent instruments controlled simultaneously. Fig. 4.5 shows the front end part of the user interface. There are several main blocks in the interface of the program:

1. The experiment selection menu ring. The experiments implemented include the "Viewer" to display data from the sensor in an online mode. It is usually used for test runs as well as tuning both the setup and debugging. "PTC" and "IntPTC" are designed to control the PTC experiment (detailed in Section 3.2, page 33). "Spectral Response" is devoted to the quantum efficiency measurements (see Section 3.2.9, page 42) while the "Stability" experiment is used to understand how the sensor behaves over a long period of time.

2. The online acquisition parameters monitor. This is used to display and monitor the acquisition parameters and data flow processes online. The monitor was mainly in use at the stage of FPGA firmware debugging.

3. HEPAPS4 acquisition control panel. Here the user can control all available parameters of the sensor and output for acquired data.

4. Experiment specific equipment control tabs. These tabs are used to set parameters for external instruments used in the experiments.

5. An online histogram displays real time data and allows preliminary basic data analysis.

6. The visualisation window shows the actual picture from the sensor and allows both 2D and 3D representation of the data.
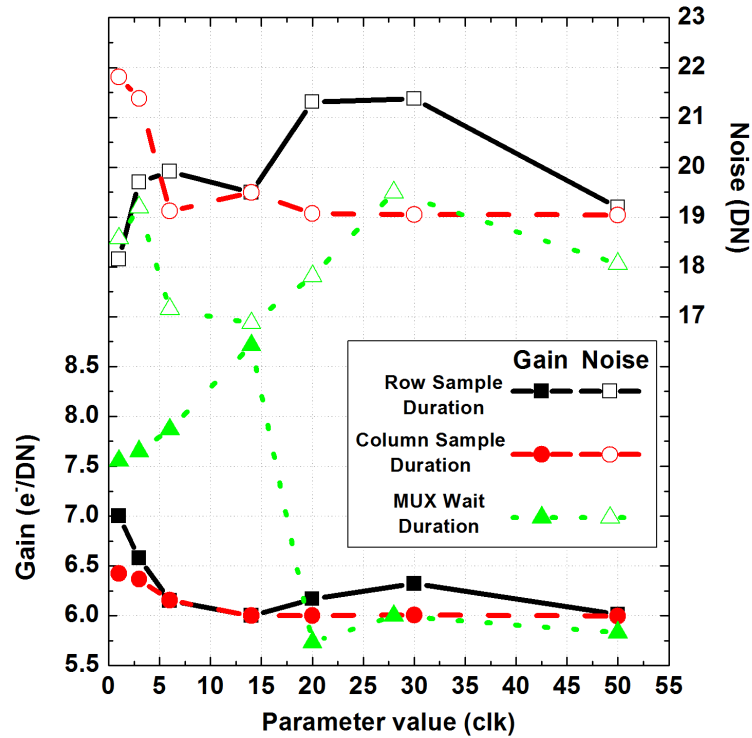
Figure 4.6: Optimisation of the timing parameters of HEPAPS4.

4.1.2 HEPAPS4 readout optimisation

Optimisation of the timing parameters

Readout sequence tuning is an essential part of the sensor characterisation process. It is an iterative process and strongly depends on the parameters that are to be enhanced. HEPAPS4 was designed for the detection of charged particles, hence the optimisation of the sensor performance was carried out in order to achieve the highest gain and lowest possible readout noise. Three timing parameters of the sensor that can heavily influence the gain and noise are – row sample duration (RSD), column sample duration (CSD) and MUX wait duration (MWD) (see Section 4.1.1, page 50, for parameters definitions) – were chosen. A series of PTC plots for normal readout mode (as defined in Section 4.1.1, page 52)
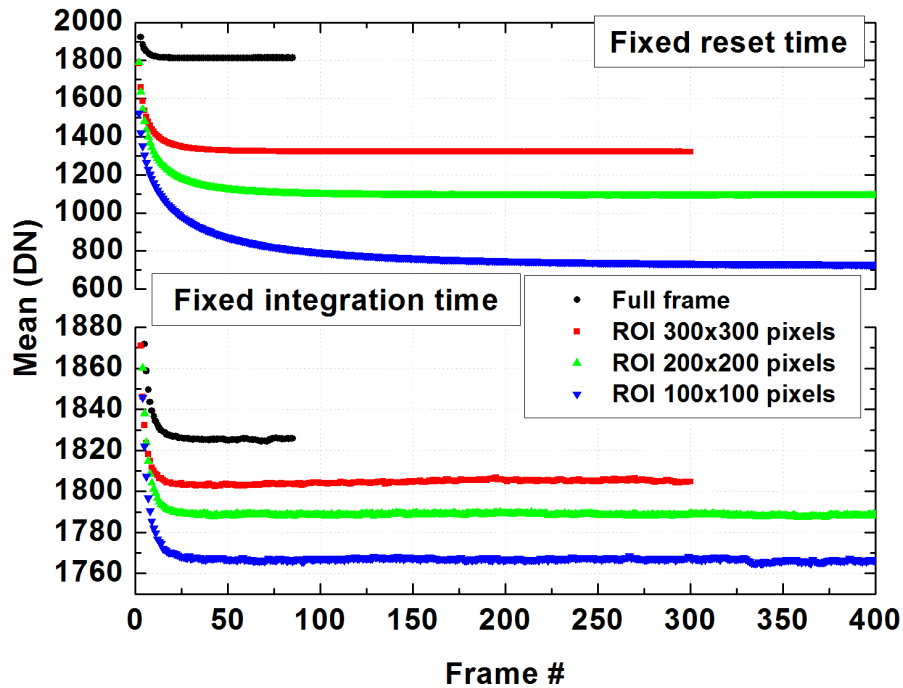
Figure 4.7: Dark level saturation for several ROIs in HEPAPS4.

were produced, using the method described in Section 3.2, page 33. Each of the three parameters of the sensor were varied one at a time while keeping other parameters to default values: 14 clock cycles for RSD, CSD and 28 for MWD. The sensor was clocked at 33 MHz. The best combination of the parameters in terms of the lowest noise, highest gain and fastest readout time were selected (Fig. 4.6). The optimised set of parameters was chosen as follows: RSD = 10 clk, CSD = 10 clk, MWD = 20 clk. All three variants of the sensor HEPAPS4 were characterised using these parameters.

Reset stability optimisation

The sensor can operate in the soft reset mode only (see Section 4.2.1, page 85). It has to be reset numerous times after being inactive in order to clear charge accumulated in the pixels due to the leakage current. A series of measurements was carried out in order to find the combination of readout parameters that
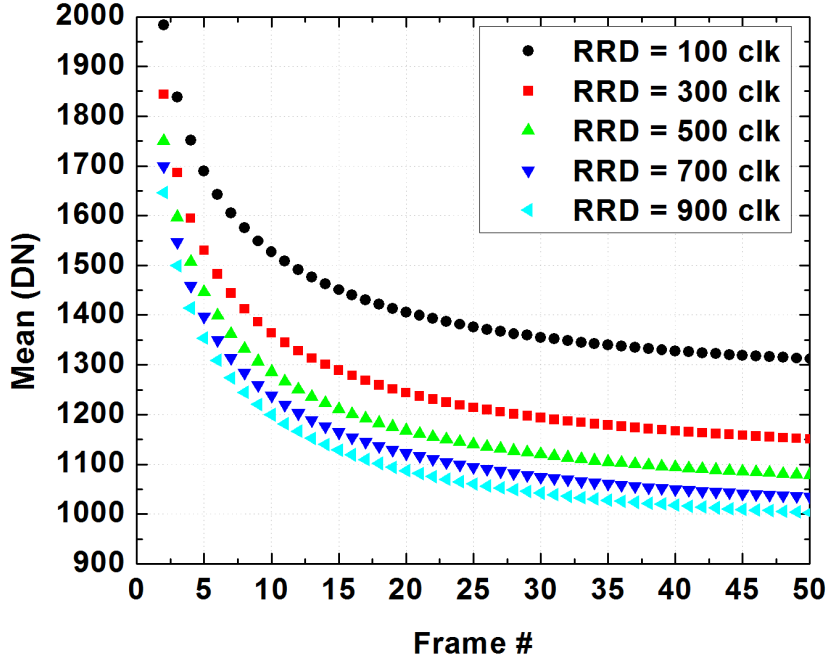
Figure 4.8: Dark level saturation for different row reset durations in HEPAPS4.

minimise the number of frames that have to be disregarded due to inappropriate reset. At the same time the concept of "dummy frame" and "number of resets" was introduced into the firmware. When "Dummy frame" $= n$, $(n > 0)$ the readout cycle resets and clocks n frames without reading data out. This allows the sensor to be reset faster than in normal readout mode. In CDS1 mode (see Section 4.1.1, page 52) the reset is performed for the first "Number of resets" frames only, achieving stable signal level faster. Fig. 4.7 shows the dependence of the dark stability level on the frame number in one acquisition run for several regions of interest (ROIs). The data for the top part of the figure is obtained keeping the integration time of the sensor to a minimum possible value for each ROI. The integration time is defined as follows

$$T_{int} = T_{WBF} + T_{readout} + T_{reset} \tag{4.1}$$

where T_{int} is the total integration time, T_{WBF} is the delay introduced between reading out the frames, $T_{readout}$ and T_{reset} are the readout and reset times of the sensor.

It was noticed that despite the constant reset time for every ROI, the stable frame for different ROI's was not the same, tending to be higher for the smaller frame size (see top Fig. 4.7). Moreover, the stable dark pedestal value dramatically varies from one frame size to another (from ≈ 1800 DN for full frame to ≈ 800 DN for 100×100 pixels). This indicates that the soft reset voltage applied is unable to fully clear the residual charge from the pixel, which is dependant on the integration time. This can also be explained in terms of different amounts of leakage current being accumulated in the pixel, which is proportional to the integration time (see Section 4.1.3, page 72).

The data for the bottom plot in Fig. 4.7 was taken keeping the integration time constant by varying the T_{WBF} parameter. The saturation frame in this case is not dependent on the ROI size and is ≈ 25 frames for 410 ms integration time. The spread in the level of saturation dramatically shrinks, however, a small difference remains. This can be attributed to a dynamic effect in the reset line from the duty cycle that is applied. The duty cycle is proportional to ((number of readout columns) + (reset duration))/(readout time). The direct proof of this theory can be demonstrated by varying the number of rows being read out while keeping the number of columns constant. The result from this measurement shows the consistency in saturation level to within $\approx 1\%$.

Other parameters that can influence the reset saturation level include the reset duration and the reset voltage level. The latter cannot be varied in the sensor. Consequently, the reset voltage is always pulled to $V_{dd} = 3.3$ V and the measurements which involve its variation are not possible. Fig. 4.8 illustrates the dependence of the dark level on the row reset duration (RRD). The data was taken for a 200×200 pixels ROI and minimum possible readout time of 30 ms. As was expected the increase of the RRD does influence the saturation and the
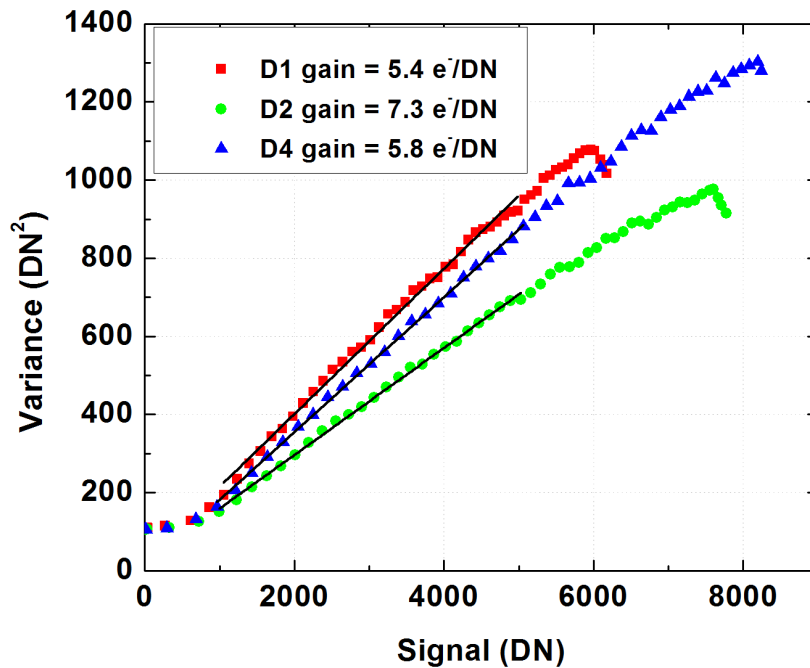
Figure 4.9: Conventional average PTC for the HEPAPS4 family.

"deeper" reset level occurs for longer reset duration. However, the dark saturation level is an arbitrary value, which does not influence measurements. It is always subtracted for all data frames in the experiments described in this thesis. The speed of saturation is not affected by the RRD due to the approximate nature of the soft reset mode.

The output of the sensor is highly sensitives to variations in timing parameters. This means that the dark frames have to be collected in the same conditions as the measurements in order to effectively use a pedestal subtraction technique.

4.1.3 HEPAPS4 optical characterisation

Gain

The HEPAPS4 conversion gain was measured on the setup described in Section 3.2.1, page 34. Three photonic methods were used, two of which are the av-
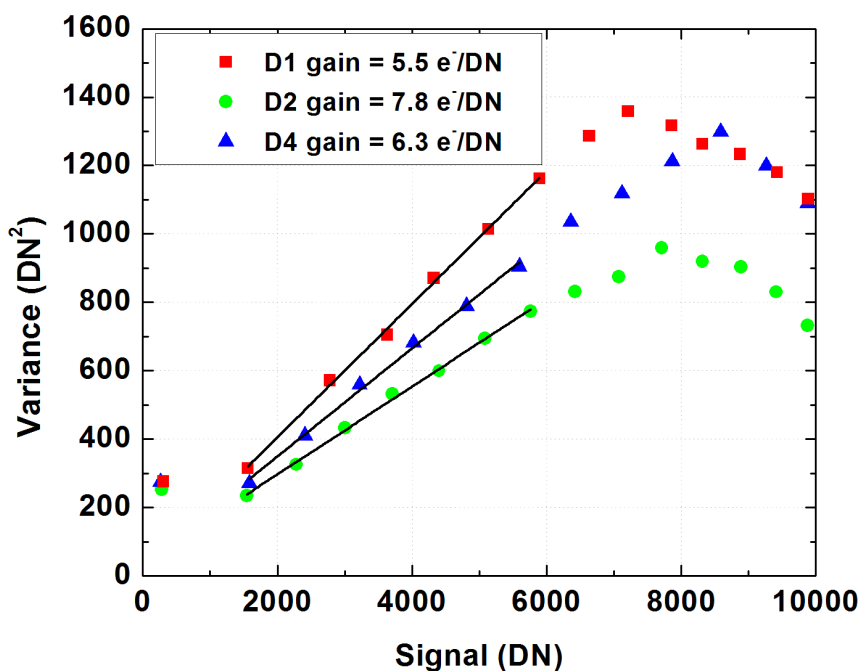
Figure 4.10: Integration PTC for the HEPAPS4 family.

erage PTC and pixel-by-pixel PTC, both are explained in Section 3.2.2, page 35. The third method of gain calculation is similar to the average gain estimation approach. The difference is as follows: the sensor is illuminated at a constant LED brightness just above the dark level of the device using normal operating parameters. The number of frames is then accumulated, varying the integration time of the sensor from minimum to a level, where the device is saturated. This method is referred to as the "integration PTC". It is an alternative method to the conventional PTC and helps to cross-check the sensor parameters. It also eliminates a potential non-linearity of the LED as the illumination level remains constant during the measurement. However, at longer integration times the leakage current of the pixels increases, while the gain fixed pattern noise is more pronounced. This kind of PTC experiment is also more time consuming (~ 5 times longer) due to the substantial integration time, especially near the full well and saturation of the device.
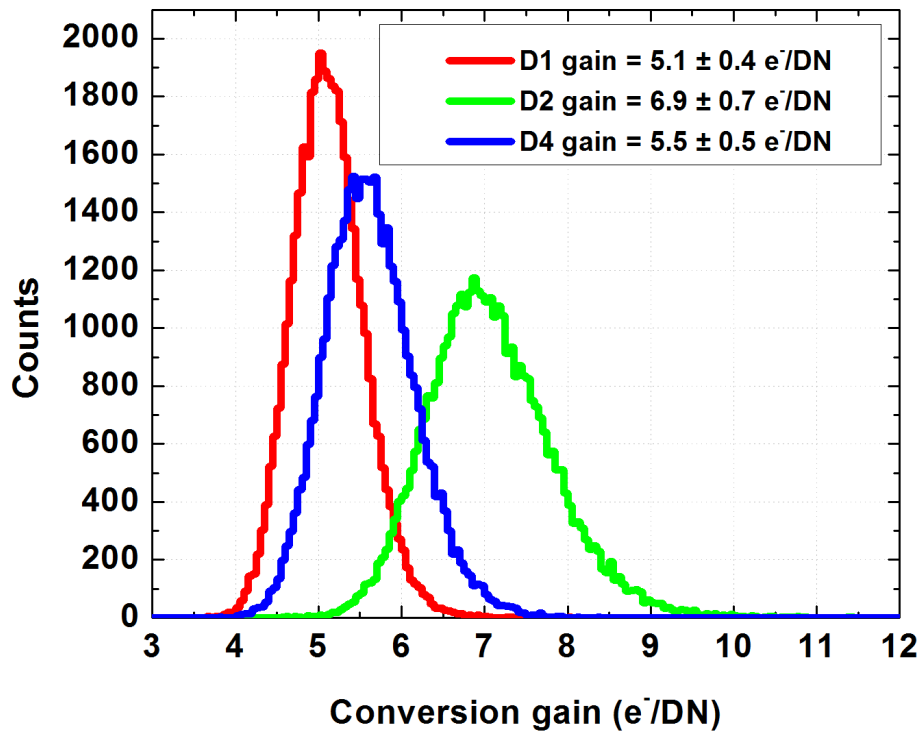
Figure 4.11: Gain distribution from pixel-by-pixel PTC for the HEPAPS4 family.

The examples of average and integration PTCs for optimised timing parameters of three variants of the sensor are shown in Fig. 4.9 and 4.10 respectively. The plots were produced in order to determine the fitting boundaries for the pixel-by-pixel PTC and cross-check the similarity of the results. Accurate estimation of the sensor gain is crucial as it is the only parameter which allows the conversion of all other measured properties to absolute units for quality assessment and direct comparison with alternative technologies available for a particular application. The conversion gain extracted from the integration PTC is systematically $7 - 10\%$ worse in comparison to the average PTC. The integration PTC requires high integration times which affects the PTC in two ways. Higher leakage current contributes to additional noise, while the diode capacitance non-linearity occurs faster.

Method	D1	D2	D4	Units
Total diode size	1.7	18	12	μm^2
Pixel-by-pixel	5.1 ± 0.4	6.9 ± 0.7	5.5 ± 0.5	
Average	5.4	7.3	5.8	e^-/DN
Integration	5.5	7.8	6.3	
Pixel-by-pixel	24.5 ± 1.9	18.1 ± 1.8	22.7 ± 2.1	
Average	23.1	17.1	21.6	$\mu V/e^-$
Integration	19.1	16.0	19.8	
Simulated values	15.7	11.0	9.6	$\mu V/e^-$
Gain FPN	8	10	9	%

Table 4.2: Summary of the gain performance for the HEPAPS4 family.

The pixel-by-pixel PTC shown in Fig. 4.11 was calculated for a 200×200 pixels ROI from 800 frames per illumination step. The boundaries of the shot noise limited linear region for fitting was taken from the average PTC. The results are consistent within a standard deviation with the other form of the PTC.

The gain estimation results are summarised in Table 4.2 and compared to the simulation results reported in [41]. The gain performance of all sensor variants is slightly better than simulated. However, all three methods of the gain estimation reported an inconsistency with the simulations as the measured gain for the "D4" is higher than one for the "D2". The diodes in the pixels are connected in parallel, therefore the total capacitance of the pixel is the sum of the individual diode capacitances. Assuming that the capacitance is proportional to the area of the diode and the other parameters that can possibly influence it are the same for two pixel designs, it is possible to estimate the relative difference in the gain of the "D2" and "D4". The "D2" pixel has two 3×3 μm diodes with total area of $(3 \times 3) \times 2 = 18$ μm^2, while the "D4" has $(1.7 \times 1.7) \times 4 \approx 12$ μm^2. This implies that the gain of the "D2" should be lower than one for the "D4". As one can see from Table 4.2, the measured gain within standard deviation satisfies this approximation. The gain FPN is $8 - 10\%$ and slightly higher for the "D2" variant of the HEPAPS4 family.
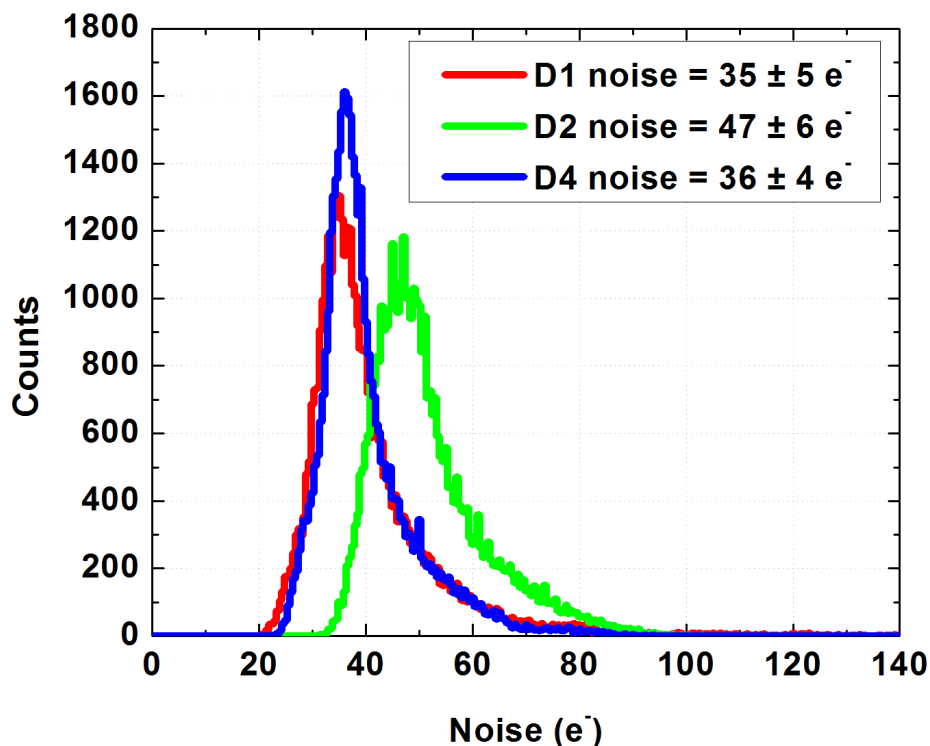
Figure 4.12: Noise distribution for the HEPAPS4 family.

Noise

The noise characterisation for the HEPAPS4 sensor consists of spatial and temporal component analysis (see Section 3.2.5 – 3.2.6, page 39 – 40). All three variants of the sensor were characterised using the following method for the temporal noise. 800 frames were accumulated in the dark from a 200×200 pixels ROI. The standard deviation for each pixel was calculated and the result presented in the form of a histogram. Fig. 4.12 shows the read noise distribution for the HEPAPS4 family. All three histograms reasonably follow the Gaussian distribution, however quite a long noise "tail" can be seen. The "D1" and "D4" chips show very similar noise performance within the uncertainties of the measurement. The "D2" variant has higher noise on average which is due to the lower gain. All three sensors show $\sim$ 1% of very noisy pixels. This was visually
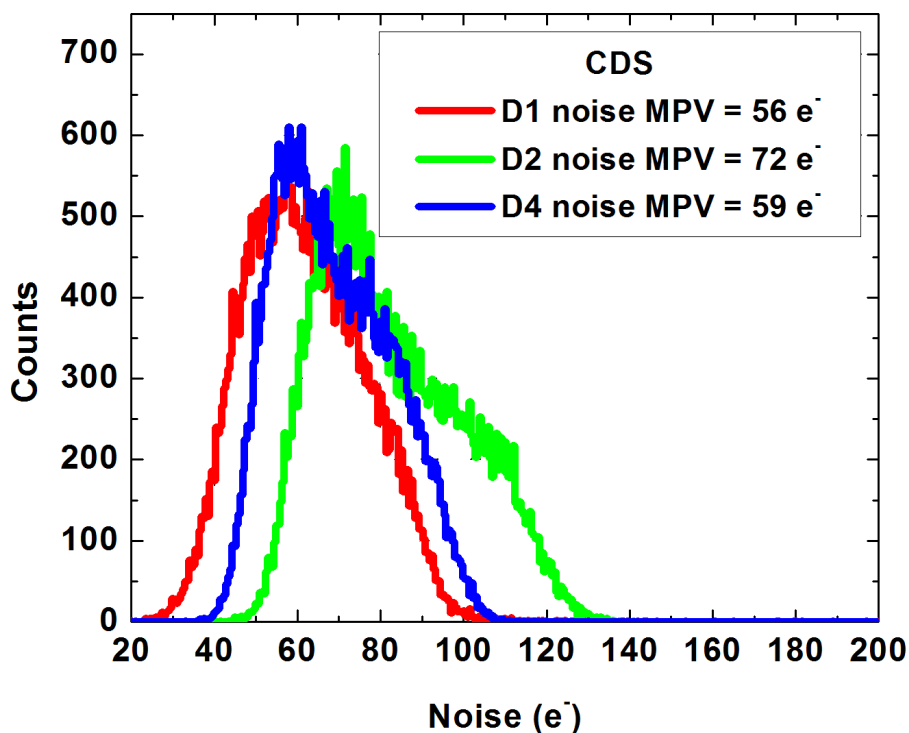
Figure 4.13: Noise distribution for the HEPAPS4 family operating in off-line CDS mode.

observed during many experiments carried out. The nature of these excessively noisy pixels remains unknown. The noise pattern tends to be fixed for all frames during one acquisition run, however it randomly changes from run to run even for the consecutive runs. The noisy pixels usually exceed $\approx 10000 \ DN$ pixel value for any dark frame (average value $1500 - 2000 \ DN$). This has to be taken into account in the cluster analysis for charged particles detection experiments, otherwise it would result in erroneous seeds being identified.

The off chip CDS was implemented in the firmware in order to demonstrate the difference in noise performance for two readout modes. The sensor does not have any on-chip buffer, so the whole frame has to be read out and stored in the FPGA memory in order to perform subtraction, which halves the number of "useful" frames. The data was accumulated from 400 dark frames in the CDS

mode 2 (see Section 4.1.1, page 52).

Fig. 4.13 shows the noise from three variants of the sensor after CDS. The noise is roughly twice as high as in the normal operation mode. The histogram is a result of the superposition of several (up to four) Gaussian distributions. There are four outputs in the sensor with separate differential amplifiers. Each of them could perform differently due to fabrication mismatches and different optimal operational parameters, which results in the histograms obtained.

Table 4.3 compares the measured results with the simulated data reported in [41]. Good agreement is observed for both D1 and D2 versions of the sensor working in the normal operation mode. D4 sensor noise performance is better than expected and is comparable to D1. All sensors showed non-Gaussian noise distributions in off-line CDS mode with mean values almost twice as high as in the normal mode. The CDS results suggest that the noise in the system is dominated by an unresolved component which is most likely associated with the readout board hosting the ADC and power regulators. This could have dynamic effects on reset lines, affect grounding and power supply to the sensor. It is not possible to check the board and report the results due to the fact that the board needs the load, equivalent to the sensor. Therefore it is suggested to always have a "dummy" sensor at the technology evaluation stage in order to be able to estimate the readout block noise, which can dramatically degrade the overall system performance.

Two kinds of spatial noise are analysed and estimated for the HEPAPS4 chip. This includes the pixel fixed pattern noise (FPN) (see Section 3.2.6, page 40) at dark and full saturation levels. The FPN is defined as the standard deviation in the histogram of the averaged frame from one acquisition run (800 frames, 200×200 pixels ROI). Fig. 4.14 shows both results for dark and saturation from all three variants of the sensor. The analysis data is summarised in Table 4.4. The response of all three variants of the sensor is very close both at dark and saturation. This indicates that for the same fabrication technology, the layout of the components

	D1	D2	D4	Units
Noise	35 ± 5	47 ± 6	36 ± 4	e^-
Noise CDS	56	72	59	e^-
Simulated values	35	45	47	e^-

Table 4.3: Summary of the HEPAPS4 family temporal noise performance.

	D1	D2	D4	Units
Dark FPN	1250	1150	1200	e^-
Saturation FPN	250	450	350	e^-
Pixel level FPN	1200	1050	1150	e^-

Table 4.4: Summary of the HEPAPS4 family fixed pattern noise performance.

and the number of photo diodes do not significantly contribute to the spatial noise. The FPN of the non-illuminated sensor is much higher in comparison to the saturated one. The non-uniformities of pixel response which are due to sensor wafers imperfections or fabrication misalignments are more pronounced if there is no light on the sensor. The relative amount of charge generated in the dark is small, therefore the response is highly sensitive resulting in a broader range of the sensor output values. Unlike the dark frame level, the output of the sensor at saturation is not highly dependent on material imperfections. The photo diode in the pixels exposed to light saturates, reaching the full well and beyond, where the charge is collected also by adjacent cells making the response fairly flat. However, at this point the non-uniformities in the column source followers as well as the column amplifiers give a significant contribution to noise on the column level. Assuming a saturated sensor, the column source follower non-uniformities dominate the FPN, while in the dark both the pixel and column based circuitry contribute to the FPN, one can estimate pure pixel level FPN as the quadrature difference of these two parameters (see bottom line in Table 4.4). As can be seen from the result the FPN is dominated by the pixel level non-uniformities.
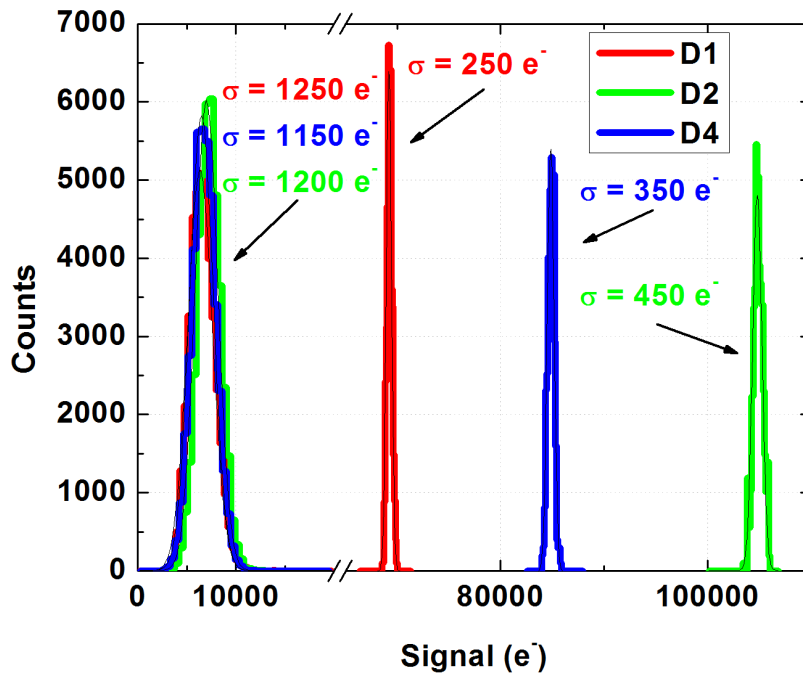
Figure 4.14: Fixed pattern noise performance for the HEPAPS4 family.

Full well capacity and dynamic range

The full well capacity (FW) and dynamic range (DR) of the sensor were calculated from the average and integration PTCs as described in Section 3.2.3, page 37. The results of the measurements are summarised in Tables 4.5 and 4.6. The FW is the highest for the "D2" version as expected because this has the biggest total area (and hence capacitance) of photo diode. The DR is the same for all three versions of the sensor. "D1" has the smallest FW but has the lowest noise, while "D2" has the highest FW as well as the highest noise. These two components compensate each other making the DR the same for all three chips.

Linearity

The non-linearly of the HEPAPS4 family was measured and calculated utilising integration without the reset method described in Section 3.2.4, page 38. The

	D1	D2	D4	Units
Full well (average PTC)	32000	56000	48000	e^-
Full well (integration PTC)	39000	61000	54000	e^-
Average full well	36000	59000	51000	e^-

Table 4.5: Summary of the the HEPAPS4 family full well capacity performance.

	D1	D2	D4	Units
Dynamic range (average PTC)	55	57	59	dB
Dynamic range (integration PTC)	57	58	60	dB
Average dynamic range	56	58	60	dB

Table 4.6: Summary of the the HEPAPS4 family dynamic range performance.

sensor was exposed to a fixed intensity LED. The integration time of the sensor was varied from the minimum possible for the 200×200 pixels ROI up to ten seconds. The resultant plot was presented in a form of the deviation from the linear fit and depicted in Fig. 4.15. All three variants of the sensor show very close non-linearity behaviour with the maximum of $\approx 6\%$ at the full well.

Dark current

Dark current of the HEPAPS4 was measured at room temperature as described in Section 3.2.7, page 41. Fig. 4.16 shows the comparison graph for all variants of the sensor. The results suggest that the dark current does not really depend on the number and size of the photo diodes in the pixel even though it remains relatively high in comparison to currently available scientific CCDs [43, 44]. This basically excludes current CMOS MAPS technology from being used in astronomy applications, where typically hours of integration time are required to acquire an image. Much progress has been made in order to reduce the DC in more recent MAPS (see *e.g.* Vanilla dark current measurement in Section 4.2.3, page 101).
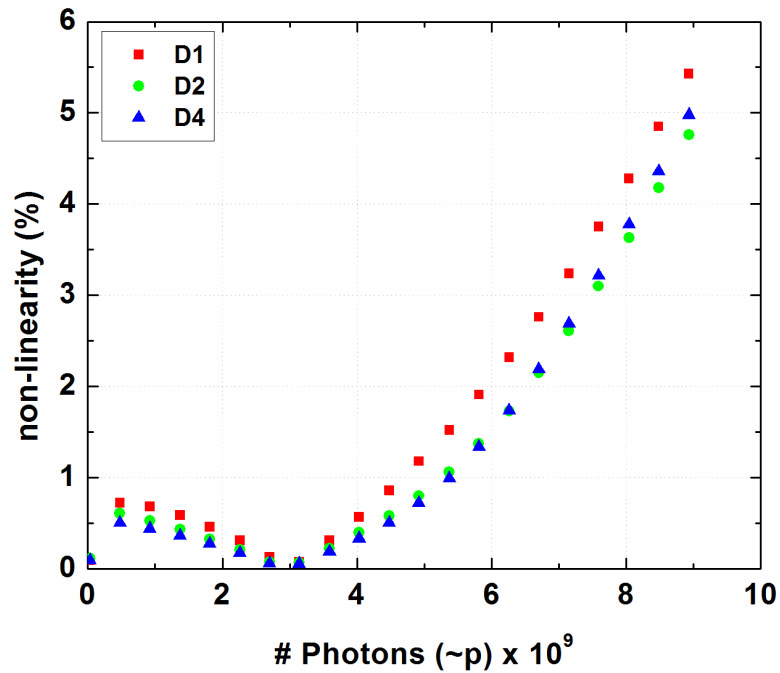
Figure 4.15: Linearity estimation for the HEPAPS4 family.

Signal-to-noise performance

Signal-to-noise performance of the HEPAPS4 is shown in Fig. 4.17. The smallest SNR is observed at lower illumination levels due to relatively high noise and small signal, while the highest SNR is reached at full well of the sensor. The average S/N is between 14 dB for "D1" and 17 dB for "D2" over the dynamic range of the sensor. The sensor has not been designed with imaging applications in mind therefore this parameter is not of a crucial importance.

4.1.4 Minimum ionising particles

The "D1" version of the HEPAPS4 family was characterised for gain and S/N performance using a 4 MBq ^{90}Sr β-source [34]. The experiment was carried out using the setup described in Section 3.3, page 45. The measurements were performed for a 600×384 pixels ROI and optimised timing parameters. Due
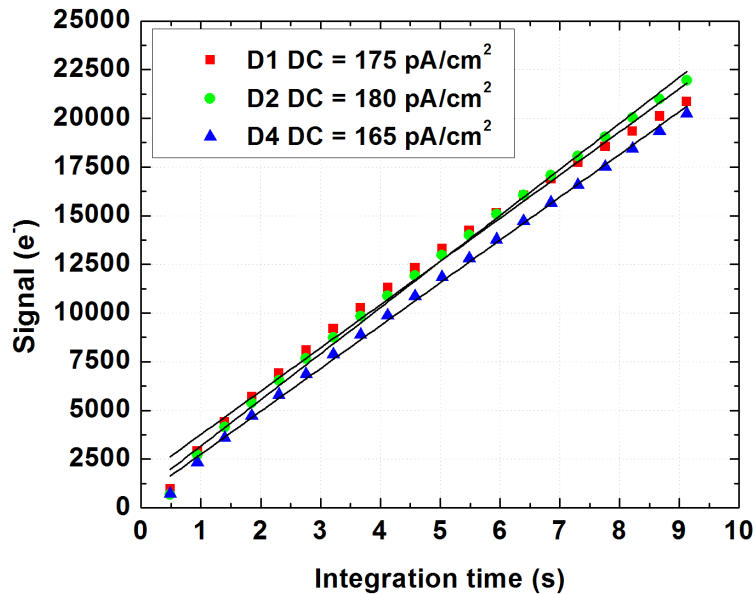
Figure 4.16: Dark current performance for the HEPAPS4 family.

to the small pixel size (15×15 μm^2) and the nature of charge collection in the CMOS MAPS (see Section 2.5.2, page 28), the passage of a β-particle through the sensor is registered by several adjacent pixels. In order to calculate the charge generated by the particle, clustering and hit reconstruction has to be performed.

A hit is a signal registered by several pixels in the localised area of the sensor after the particle passage. A dedicated cluster analysis algorithm was developed within the Data Analysis Framework. The algorithm is split into three main parts: noise map calculation, isolated seed identification, cluster formation and analysis. The noise map was calculated on a pixel by pixel basis for the ROI used from 200 sets of 300 frames (maximum available storage space in the FPGA memory). It was found that for an unknown reason the pedestal values accumulated from different runs sometimes vary from run to run by $\sim$ $5 - 10\%$ under the same conditions, making it very difficult to acquire enough statistics for the noise and pedestal calculation as well as the pedestal subtraction from the signal frames. This is probably one of the reasons why the noise obtained for this
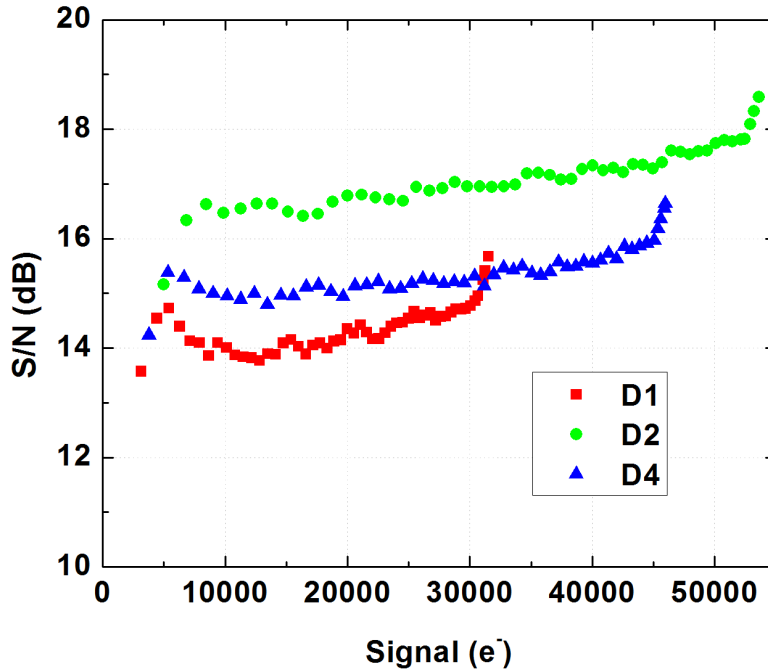
Figure 4.17: Signal-to-noise performance for the HEPAPS4 family.

experiment is slightly higher, 50 e^-, instead of 35 e^-, obtained in Section 4.1.3, page 67. The other reason may be due to the edge pixels being included, which are always slightly noisier. Isolated seeds are identified after the noise map is created and the pedestal is subtracted from the signal frames. The algorithm scans each frame for pixels exceeding 7 σ in value. When such a pixel is identified, the surrounding 9 × 9 region is checked for other pixels exceeding 7 σ cut. If such pixels are identified and it is lower significance that the original seed in a 3 × 3 region only, the program flags that the an isolated seed has been found, otherwise this one is skipped from the analysis. An isolated seed map is created for each frame. Another algorithm then scans the frames again and compares them with the associated seed map. It calculates the sum of all pixels around the seed within a 5 × 5 region which exceed 3 σ cut, recording the cluster size in pixels and cluster charge in ADC units.

The results of the experiment are presented in Fig. 4.18 and 4.19 for the cluster
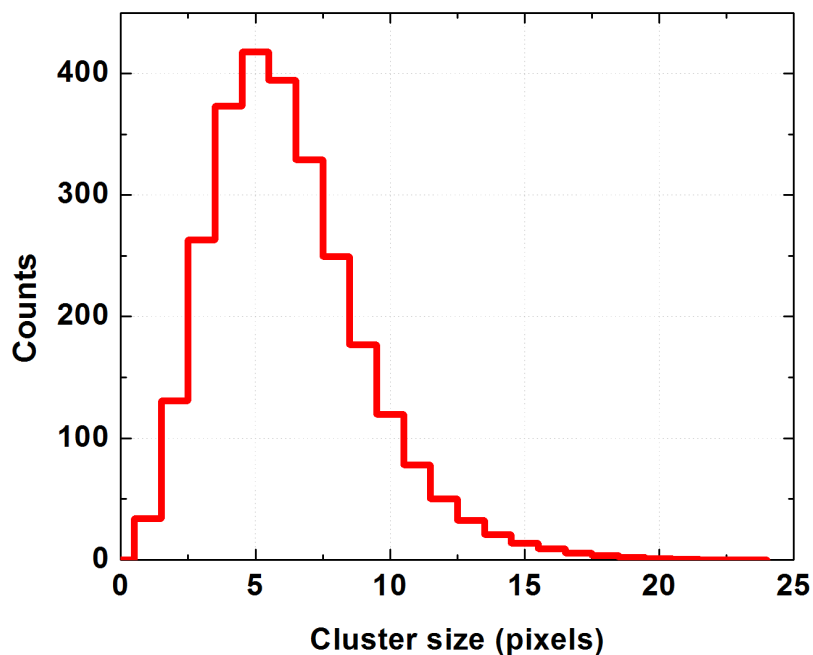
Figure 4.18: Cluster size distribution from the ^{90}Sr MIPs source in HEP-APS4.

size and cluster charge respectively. The most probable value for the cluster size was found to be ≈ 6 pixels. The biggest clusters identified are exceeding 20 pixels in size, which are associated with particles entering the sensor at acute angles. The minimum cluster size was put to two pixels due to a large number of very noisy pixels being identified as seeds (was discussed in Section 4.1.3, page 67). This helped to exclude such pixels. The shape of distribution shown in Fig. 4.19 is not consistent with the convoluted Landau and Gaussian distribution. As was demonstrated in [45], such an approximation is only valid for the thin absorbers (of order of 1 μm), whereas the HEPAPS4 has a 20 μm sensitive layer. The most probable value for charge deposited by a MIP in the sensors is 1800 e^-. Considering 20 μm epi-layer thickness and the fact that a MIP traversing a silicon substrate generates ≈ 80 electronhole pairs per micron [45], one can expect the charge generated by a MIP to be 1600 e^-. The discrepancy observed can be
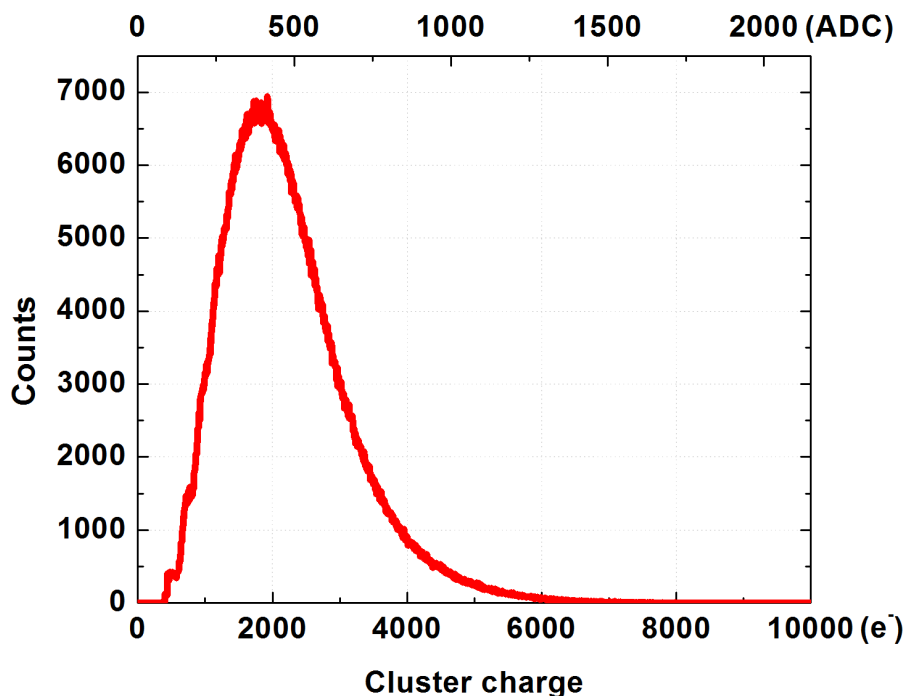
Figure 4.19: Cluster charge distribution from the ^{90}Sr MIPs source in HEPAPS4.

explained in two ways. The source was placed 10 *cm* from the sensor, which makes only a fraction of MIPs incident on the detector at a right angle increasing the amount of the deposited charge. At the same time the charge deposited outside the epi-layer in the bulk can diffuse back and be counted for increasing the total measured charge. The sensor S/N ration for the most probable charge value is found to be an acceptable value of 40.

4.1.5 HEPAPS4 conclusions

The HEPAPS4 family of CMOS MAPS was designed specifically for charged particle detection and has been proved to work well. A new firmware for the sensor has been developed, allowing comprehensive sensor characterisation. This includes two versions of CDS and trigger readout. Labview based optical characterisation as well MIPs setup were created, which enables fully automated

experiments to be carried out. All three sensors in the family were tested for gain, noise, linearity, dynamic range and dark current using visible light photons and MIPs. Close attention was paid to optimise the readout timing parameters of the sensors which allowed to gain extra $\approx 20\%$ in performance. The noise of the sensor was found to be in a good agreement with simulated data for "D1" and "D2" while for "D4" the measured values are better. Off-line CDS did not give anticipated noise improvements, which suggest that the noise of the system is dominated by the readout board, rather the sensor. The mean pedestal value instability remains a serious issue, preventing measurements, requiring long acquisition runs to be carried out effectively.

4.1.6 HEPAPS4 as a neutron detector

Motivation

Neutron imaging is a fast growing and powerful technique for non-destructive testing with unique features compared to roentgenography and other methods. The advantages include higher sensitivity to materials with a lower atomic number (*e*.g. hydrogen and carbon) and deeper penetration of thick objects made of heavy elements (*e*.g. lead and bismuth). Conventional tools, for example image plates for neutron radiography, show good results, though, there are many limitations. New imagers require higher performance parameters, especially with respect to more sophisticated functionality, time resolution, dynamic range and other properties. CMOS MAPS technology has already demonstrated several advantages over other existing technologies in particle tracking, imaging and radiation detection applications, with respect to functionality, power consumption, readout speed and fabrication costs. This subsection proves that CMOS MAPSs, if covered with an appropriate conversion material, are suitable for both thermal and fast neutron detection.

Adaptation for neutron detection

HEPAPS4 silicon sensor can hardly detect neutrons. In order to increase the detection efficiency two kinds of neutron converters were put on top of the chip. Approximately half of the sensor was left bare in order to estimate the detection efficiency of the silicon MAPS. The adaptation of the neutron converters corresponds to the design given in [46, 47].

Thermal neutron converter is based on ^6Li in a form of ^6LiF powder. The substance is mixed with polyvinyl alcohol binder, deposited on thin aluminium foil and put in close contact with the sensor surface. Neutrons react with light Li atoms in the following way:

$$_3^6Li \; + \; _0^1n \; \rightarrow \; _1^3H \; (2.72 MeV) \; + \; _2^4He \; (2.05 MeV) \tag{4.2}$$

This produces oppositely directed α-particle and triton, both of which can be detected by the sensor.

A 1.1 mm thick polyethylene (PE) plate was used as a converter of fast neutrons. Hydrogen enriched material has the highest cross section for detection of neutron with > 1 MeV energy. As a result of interaction, a recoil proton is produced by an elastic scattering on hydrogen, which can be traced in the sensor.

Experimental setup

The measurements were performed at the Czech Metrology Institute in Prague. Three neutron sources were used for the experiment. Thermal neutrons were generated by a fission reaction in a natural source and moderated by graphite to an average energy of 0.025 eV. The sensor was positioned on top of the opened reactor cavity. Fast neutrons were emitted from the point-like ^{252}Cf and $^{241}AmBe$ sources. In order to obtain a balance between interaction occupancies of the detector and reasonable count rate the sources were placed 5 and 10 cm from the sensor respectively.

A set of dark frames was accumulated before the data acquisition in order to calculate the pedestal frame. The data was accumulated over several hours. The default optimised sensor parameters were used. The cluster analysis algorithm (see Section 4.1.4, page 73) was applied to pedestal subtracted data frames in order to understand the response of the sensor to secondary particles. Fig. 4.20 shows a typical symmetrical tritium cluster of ~ 8 pixels in diameter. Tritium is lighter than α-particle and can pass the passivation layer as well as electronics of the sensor and deposits its energy in the epi-layer. The secondary protons, resulting from fast neutron interaction with hydrogen, can enter the sensor at acute angles and lose all their energy in the epitaxial silicon. Fig. 4.21 illustrated such an interaction, where the proton deposits its energy following the Bragg curve.
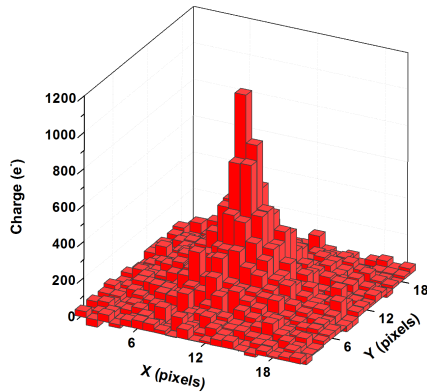
Figure 4.20: Typical cluster response resulting from the interaction of tritium in HEP-APS4.
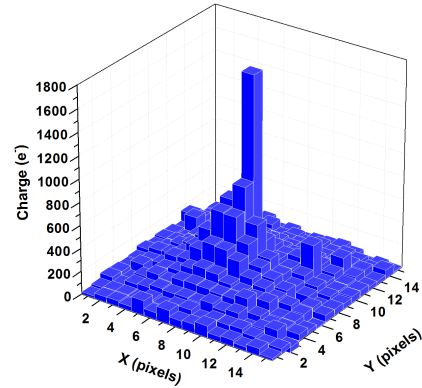
Figure 4.21: Bragg cluster resulting from particle energy deposition in the epi-layer of HEPAPS4.
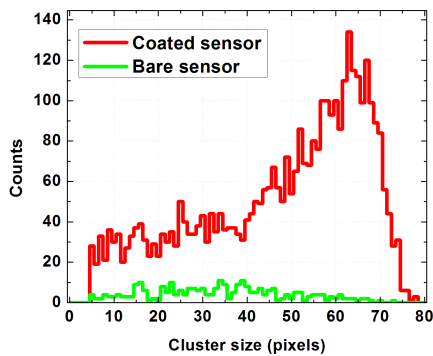
Figure 4.22: Cluster size distribution resulted from thermal neutron interactions in the ^6LiF converter and bare sensor.
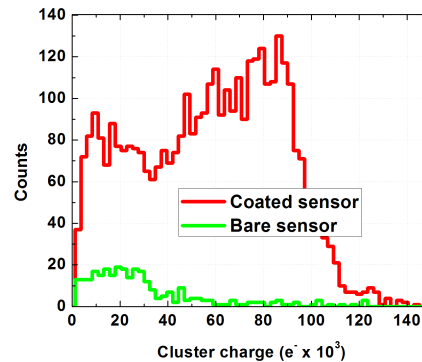
Figure 4.23: Cluster charge distribution resulted from thermal neutron interactions in the ^6LiF converter and bare sensor.

Thermal neutron response

The results from the cluster analysis indicated that the typical cluster size of the thermal neutron interaction product is $60 - 70$ pixels (Fig. 4.22). The cluster charge distribution shown in Fig. 4.23 suggests that both tritium and α-particles contribute to the signal as there are two energy peaks that can be identified. It is assumed that the higher-energy peak corresponds to ^3H, while the other is due to
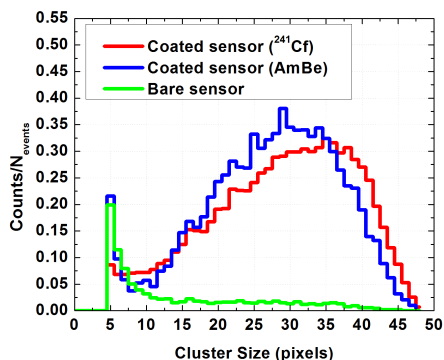
Figure 4.24: Cluster size distribution resulted from fast neutron interactions in the PE converter and bare sensor.
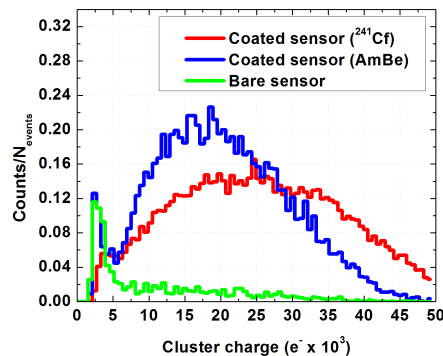
Figure 4.25: Cluster charge distribution resulted from fast neutron interactions in the PE converter and bare sensor.

α-particles. Such a spectrum could be the result of the overlapping of the Bragg curve from the tritium interaction in the epi-layer of the sensor with the end of the Bragg peak from the α-particle. A 2.72 MeV triton can travel up to 30 μm in silicon [48]. Taking into account that nearly right angle events are rare, one can assume that most of the charge is collected in the epi-layer or diffused back from the adjoining bulk. A 2.05 MeV α-particle, even if it enters the sensor at a right angle, will lose most of its energy in the converter, passivation layer and electronics ($\sim$ 6 μm in total). Fig. 4.23 reflects the spectrum from thick ^6LiF converter and a silicon diode [49].

Fast neutron response

Fig. 4.24 and Fig. 4.25 show the cluster size and cluster charge distributions normalised to the total number of events recorded for ^{252}Cf ($\approx$ 32000) and $^{241}AmBe$ ($\approx$ 10000). The range of the recoil protons ($\approx 1 - 4\ MeV$) in silicon is $\approx 90 - 110\ \mu m$ [48]. The geometry of the setup and kinematics of fast neutron interactions suggest that only a few protons (which enter the sensor at very acute angles) can deposit all their energy in the epi-layer. The energy loss of the recoiled protons are on average higher for ^{252}Cf due to the lower average kinetic energy

of neutrons.

Direct silicon interactions

Both fast and thermal neutrons can interact directly with silicon via elastic and inelastic $Si(n,p)$ and $Si(n,\alpha)$ scattering reactions. The cluster analysis was carried out in the region which was not covered with the converter in order to study these phenomena. The results from both fast and slow neutrons show that $\sim 10\%$ of all neutron interactions consist of the reactions in silicon. This has to be taken into account when the overall detection efficiency is calculated.

Fig. 4.23 shows that $\sim 50\%$ of charge deposited in the lower-energy end of the spectrum comes from the silicon interaction. This illustrates the idea that only α-particles entering the sensor at roughly right angles reach the epi-layer of the sensor.

Products of neutron reactions in silicon are shown for all ranges of cluster sizes identified (Fig. 4.22 and Fig. 4.24) with the highest contribution from fast neutrons products occurring in clusters of 4 - 10 pixels in size. This can be seen in the Fig. 4.24 for both ^{252}Cf and $^{241}AmBe$ where bare and coated parts of the sensor are compared.

Detection efficiency

Table 4.7 summarises detection efficiencies for both direct silicon interactions and via proton generation in the PE converter. The detection efficiency for thermal neutrons cannot be calculated due to inaccurately known neutron flux at the top of the graphite prism cavity where the sensor was placed. However following [46] and [47], thermal neutron detection efficiency is estimated to be $3-5\%$.

CMOS MAPS neutron detector discussion and conclusions

Recent advances in the development of CMOS MAPS as well as increased interest in the use of neutrons for material study [46, 50] give confidence that CMOS

	PE converter (%)	Silicon reaction (%)
$^{241}AmBe$	$(6 \pm 2) \times 10^{-2}$	$(0.15 \pm 0.05) \times 10^{-2}$
^{252}Cf	$(3 \pm 1) \times 10^{-2}$	$(0.50 \pm 0.15) \times 10^{-2}$

Table 4.7: Summary of HEPAPS4 fast neutron detection efficiency.

MAPS technology, combined with relatively uncomplicated post processing, will open a broad range of applications. This could include online beam diagnostics and monitoring at neutron scattering facilities. Tremendous flexibility of design options and standard CMOS fabrication processes allow task specific functionality integration on chip at no significant extra cost. Industrial quality control, security equipment and medical imaging also contribute to a long list of possible future applications for CMOS MAPSs as neutron detection systems.

We have successfully demonstrated that CMOS MAPSs, if covered with the appropriate conversion material, are suitable for γ-transparent fast and thermal neutron detection. The calculated conversion efficiency for fast neutrons is similar to hybrid pixel detector technology ($\sim$ 0.1%) [51]. Further irradiation experiments together with extensive simulations will be carried out in order to fully understand the spectra and performance capabilities. The results obtained pave the way to investigate an opportunity for a number of applications utilising all the advantages of the MAPS technology.

4.2 Vanilla

The PEAPS (Project Evaluation APS) or Vanilla is a general multi-purpose sensor developed within the MI^3 collaboration [52] (Multidimensional Integrated Intelligent Imaging) in order to evaluate the potential use of the technology in various applications. The sensor has 520×520 pixels at 25 μm pitch and was produced with two sensitive epi-layer thicknesses, 14 μm and 20 μm for noise evaluation purposes. Both versions of the sensor also come back-thinned in order to extend their sensitivity in the near ultraviolet region. Vanilla has two possible readout modes using either the standard off-chip ADC approach or an on-chip ADC to increase the readout speed. Reduced noise performance of the sensor is achieved by utilising a "flushed" reset approach, keeping image lag to a minimum, while "hard" and "soft" resets can be invoked for comparison. Conventional column shift registers are replaced by address decoders, which allows region of interest (ROI) readout in analog mode with 10-bit precision.

4.2.1 Vanilla acquisition system

Pixel architecture

The pixels of the sensor feature the standard 3MOS design (see Section 2.5.2, page 28). However, external column-based circuitry was implemented in order to evaluate the effects of different reset modes (Fig. 4.26). The conventional pixel can be reset in two reset modes, either soft or hard depending upon the voltage applied at the gate and the drain of the reset transistor.

In soft reset mode, the gate and the drain of the reset transistor are pulled to the fixed V_{dd} voltage, while the photo diode continues to charge up logarithmically above threshold voltage (Fig. 2.9 in Section 2.3.2, page 25). This means that in soft reset mode there is a residual charge on the photo diode left from the previous integration. This is known as image lag and is most pronounced when the scene taken strongly varies in contrast from frame to frame, resulting in a "ghost"
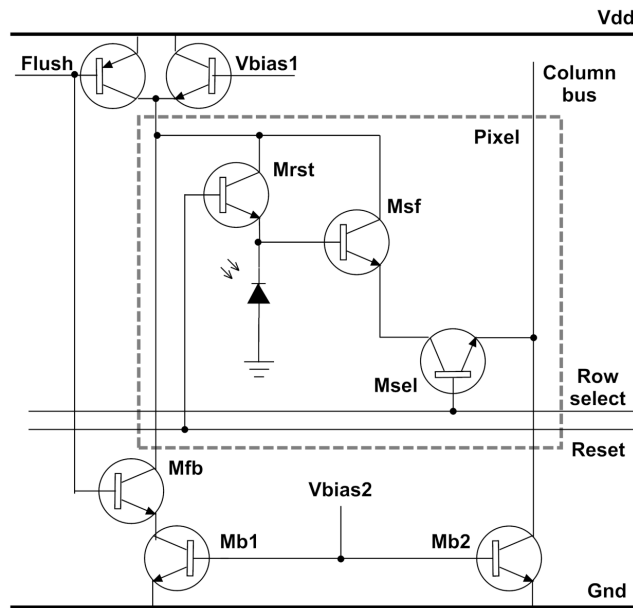
Figure 4.26: Vanilla pixel with column-based flushed reset circuitry.

image.

The pixel is reset in hard mode if the gate voltage of the reset transistor is higher than the drain voltage by more then the threshold voltage (see Section 2.3.2, page 23). The photo diode in this case is charged up to a fixed V_{dd} after the reset. This overcomes the problem of image lag. However, it has been shown that in this mode the reset noise is higher (see *e.g.* [53]).

It was demonstrated that, if the hard reset is followed by a soft reset, the image lag can be suppressed with a reduced reset noise [33]. This is known as a "flushed" reset. Fig. 4.27 shows the circuit configuration for Vanilla during hard and soft phases. The reset occurs as follows. The Flush strobe is pulled high to connect the reset voltage bus to M_{b1} and M_{b2} transistors via the M_{fb} switch (Fig. 4.27a). These two transistors are biased by V_{bias2} and pull the reset transistor drain to a voltage lower than V_{dd}. Hence, when the Reset strobe, equal to V_{dd}, is applied to the gate of M_{rst}, the transistor is overdriven and acts as a low resistance FET switch and the pixel is reset in hard mode.

The flush strobe is pulled low when the hard reset is accomplished. This

(a) hard reset activated.   **(b)** soft reset activated.
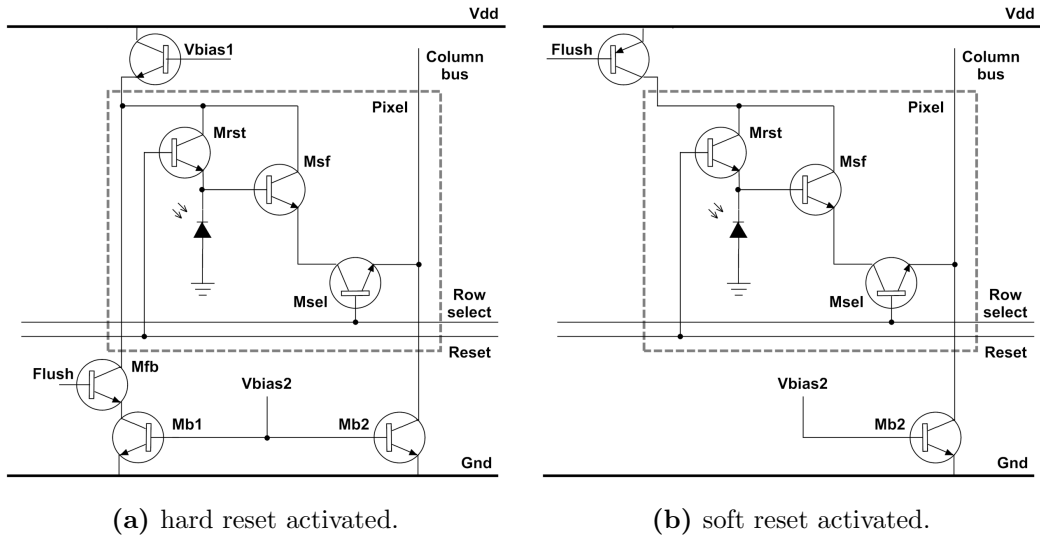
Figure 4.27: Vanilla flushed reset operating stages.

results in the configuration shown in Fig. 4.27b. The M_{b1} transistor is no longer connected to the Reset Voltage Bus, resulting in the reset transistor drain being pulled to V_{dd}. The gate of the M_{rst} is no longer higher than the drain voltage, which results in a soft reset.

Readout control

A general readout floor plan of the sensor is shown in Fig. 4.28. The sensor readout starts with a reset of the ADC and all the pixels, followed by setting up the bias generators. Vanilla can be read out in full frame mode or in ROI readout mode. Rows of the sensor are accessed by applying a 10 bit value to the address decoders. Having selected a row of pixels for reading, each column read line shows data from a corresponding pixel. In full frame mode the image can be digitised before the output. This is achieved by using an on-chip 12 bit successive approximation ADC [54]. Due to the size of the ADC it is possible to place only one ADC for every four columns, hence signals from the columns are multiplexed to ADCs. Following each column conversion the resulting digital value is stored in a 12 bit latch RAM until all sets of four columns are converted. The data is
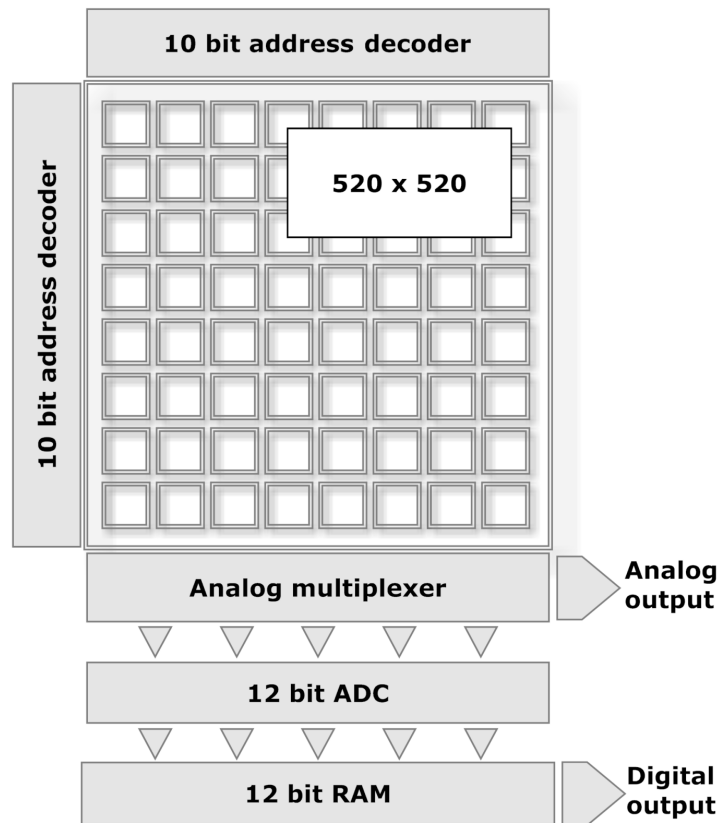
Figure 4.28: Vanilla readout floor plan.

then loaded in parallel into a shift register and clocked out to the digital output.

Alternatively the data from the sensor can be read out in analog mode, enhanced by the high speed ROI access capability. The data is output serially using two analog multiplexers. Each multiplexer drives the input to a buffer amplifier that provides a differential output from the chip. The outputs are connected to the off-chip ADCs where the data is digitised.

4.2.2 Vanilla optical characterisation

The Vanilla MAPS can work in analog and digital mode with hard, soft and flushed reset. All timing and biasing parameters were set to defaults. The characterisation of the sensor was fully accomplished in analog hard mode and the results were compared to other modes. The measurements were carried out using
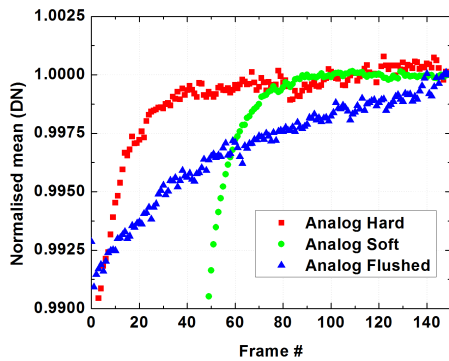
Figure 4.29: Vanilla sequence read stability in analog mode with three types of reset.
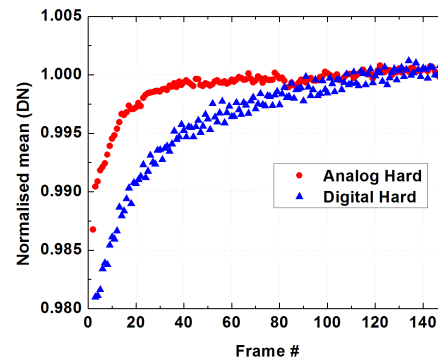
Figure 4.30: Vanilla sequence read stability in analog and digital readout mode with hard reset.

the setup described in Section 3.2.1, page 34.

Sequence read stability

Each type of sensor reset affects the data in one consecutive acquisition run in a different way. Due to the fact that the stabilised ADC level of the dark frame differs for every operation and reset mode, the data obtained was normalised to the ADC level of the last frame. Fig. 4.29 shows how the normalised dark mean signal depends on the frame number in consecutive acquisition run in analog readout mode. The nature of a hard reset makes it the most favourable in terms of speed of saturation. The signal becomes very stable after 40 frames. The readout stability in soft reset occurs after the $80th$ frame. Flushed reset is a combination of hard and soft resets, therefore the speed of saturation is also a trade off between the two. The mean signal does not become flat within first 150 frames. However, a deviation from the saturated level of less than 1% is achieved after $2-3$ frames only, which makes this reset mode competitive with the hard mode in terms of reading out a sequence of consecutive frames.

The hard reset approach was compared for analog and digital readout modes. The result is shown in Fig. 4.30. In the digital mode saturation occurs slower in
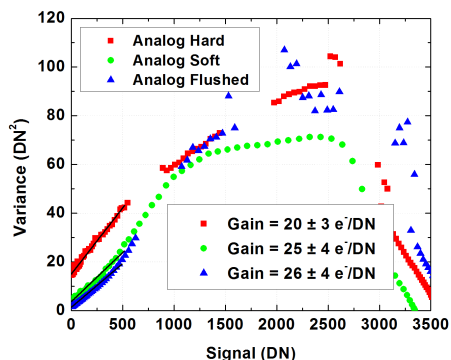
Figure 4.31: Vanilla PTC in analog mode with three types of reset.
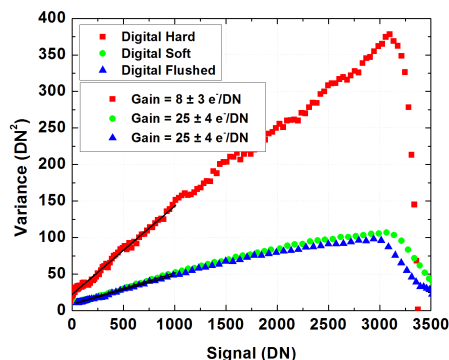
Figure 4.32: Vanilla PTC in digital mode with three types of reset.

comparison to the analog mode. A 1% deviation from unity occurs after the $20th$ frame only.

All the following measurements were accomplished taking into account the saturation stability issue. Therefore, the initial frames were always discarded. The deviation of accepted frames from the saturation level has to be less than 1%.

Gain

The PTC measurement for the Vanilla MAPS was accomplished by both "averaged" and "pixel-by-pixel" methods (see Section 3.2.2, page 35). Fig. 4.31 shows PTC plots and estimated gain for the analog readout mode with three types of reset. Averaged PTC was used to estimate the fit boundaries for the pixel-by-pixel PTC. The comparison of results between the two gain estimation methods show that they are consistent, the latter one also giving gain (FPN). The averaged PTC shows significant deviation from the linearity in the shot noise limited region for soft and flushed reset. This is attributed to the inherent non-linearity of the MAPS and photo diode sensitivity in particular [55]. It arises due to the fact that the capacitance of the p-n junction diode is dependent on the bias applied to it. A technique for compensating this phenomenon was developed [55] and proved to be valid [56]. It was shown that the conventional gain estimation
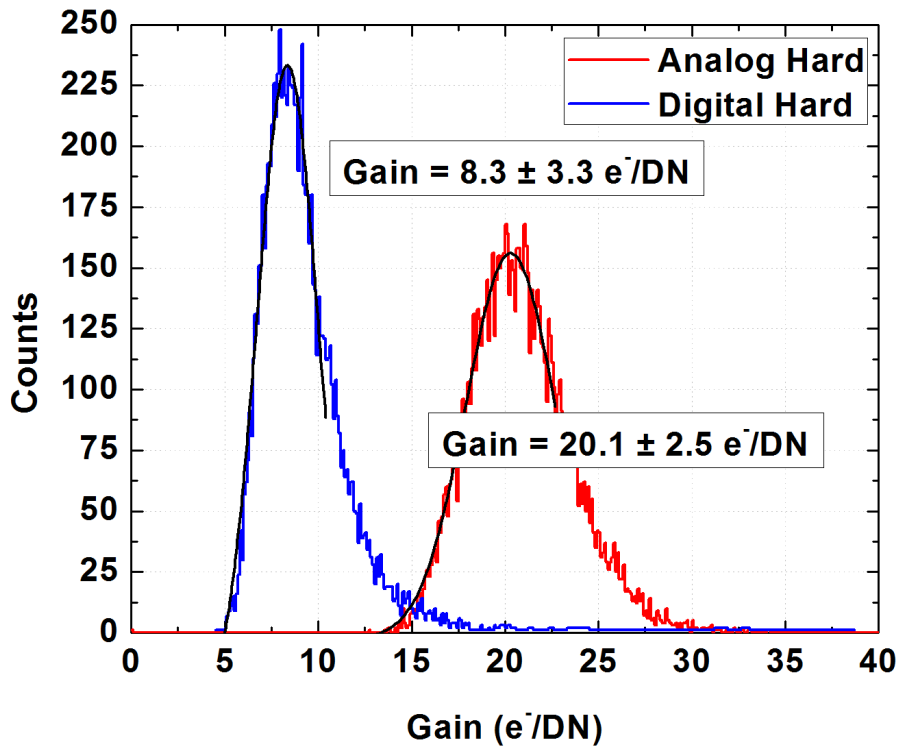
Figure 4.33: Vanilla gain distribution for analog and digital readout modes with hard reset.

method underestimates the gain in analog mode with hard reset by $\sim 13\%$ [56].

The PTC for the digital readout mode is shown in Fig. 4.32. The digital hard mode PTC behaves exceptionally linearly from the read noise to the full well of the sensor. At the same time both soft and flushed reset modes do not show significant non-linearity in the shot noise limited region as was observed for the analog mode. These observations suggest that the non-linearity in the Vanilla sensor not only comes from the inherent p-n diode capacitance change, but is also due to the off-chip ADC. The embedded nature of the readout system does not allow separate study of the off-chip ADC in order to quantify the effect of its non-linearity.

The comparison histogram between analog and digital modes with hard reset is shown in Fig. 4.33. A small "tail" can be observed in the digital mode, showing
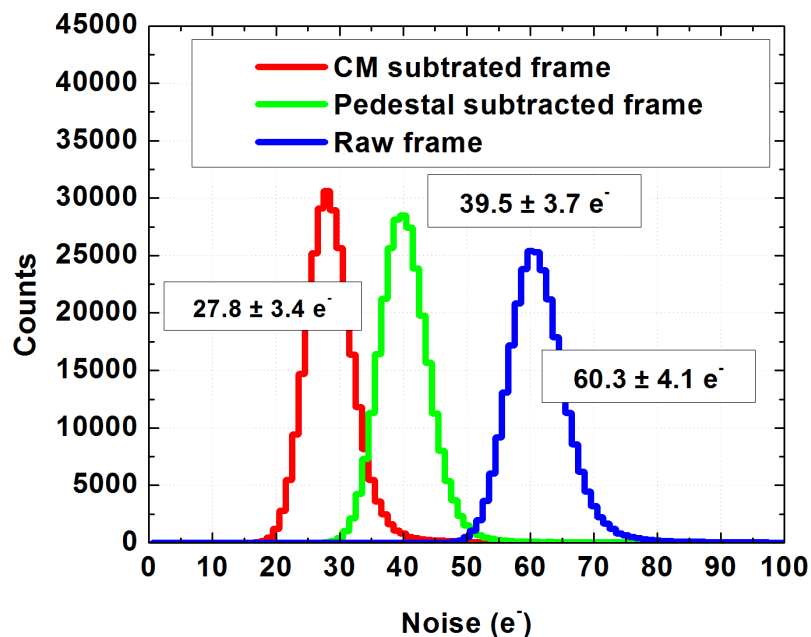
Figure 4.34: Vanilla noise before and after FPN removal in analog mode with hard reset.

higher gain FPN.

Fixed pattern noise correction

Each pixel in the sensor responds differently to incident uniform light. This is due to fixed pattern noise (FPN) (see Section 3.2.6, page 40). Fig. 4.35a shows an example of a typical dark frame image of the sensor and its histogram. The standard deviation of the histogram distribution is a measure of dark FPN $\approx$ 1000 e^-. A pedestal subtraction technique usually removes FPN. The histogram in Fig. 4.35b shows that the FPN is reduced by a factor of 10 when the pedestal is subtracted. However, the image in Fig. 4.35b reveals an additional spatially fixed non-uniformity of the sensor. This is attributed to the rolling shutter readout approach in analog mode and is usually referred to as the *common mode (CM) noise.* Knowing the nature of the noise source, the output of the sensor can be corrected. A correction algorithm was developed in order to take this

issue into account. It calculates an average pixel value in each row and sutbracts this value from all pixels in the row. Fig. 4.35c shows an image and histogram of a corrected frame. The resulting image does not contain the sinusoidal artifact and the FPN is reduced by a further factor of two to $\approx 30\ e^-$.

(a) Raw dark frame.

(b) Pedestal sutbracted dark frame.

(c) Pedestal sutbracted dark frame.
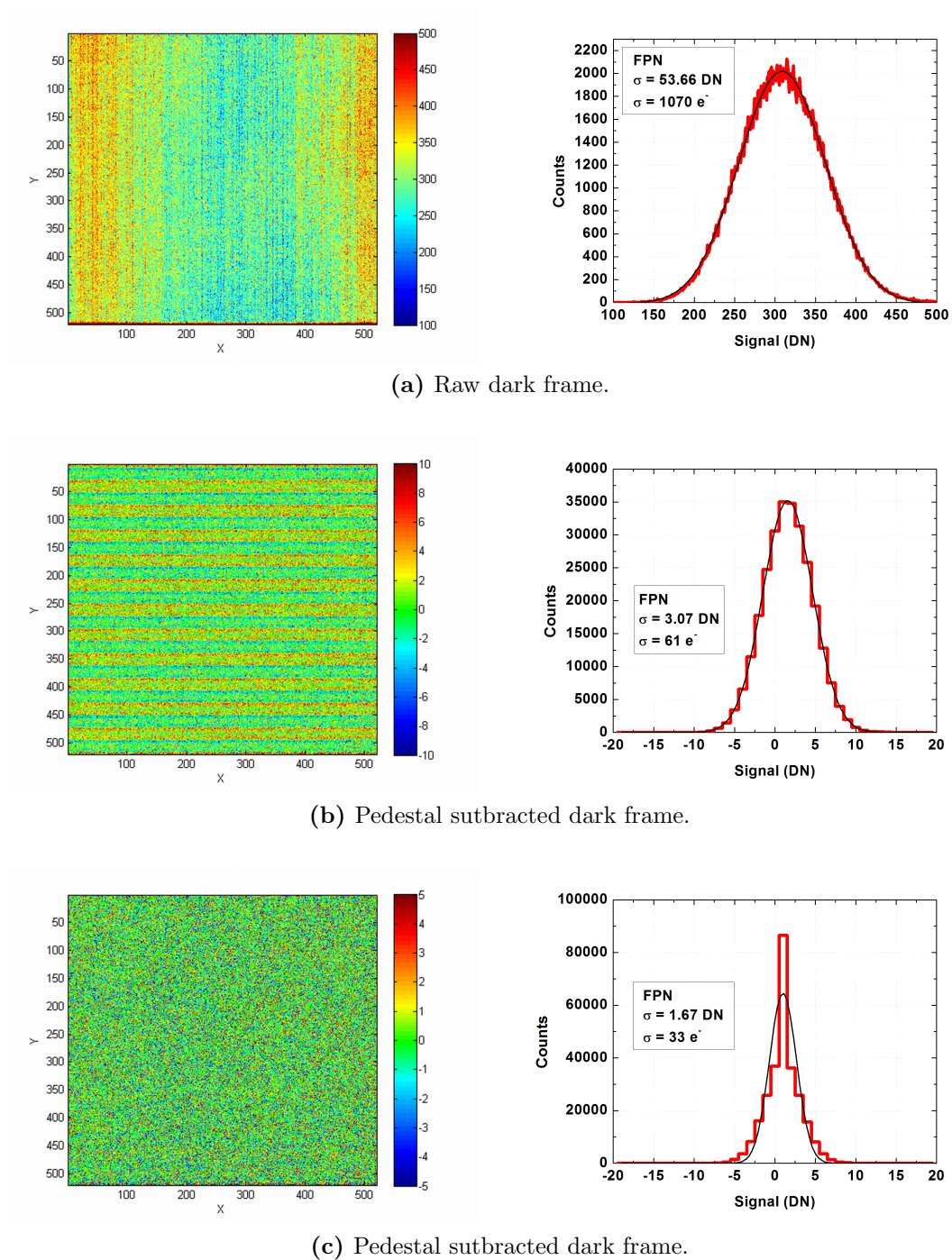
Figure 4.35: Vanilla dark frame before and after FPN removal.

(a) Before   **(b)** After
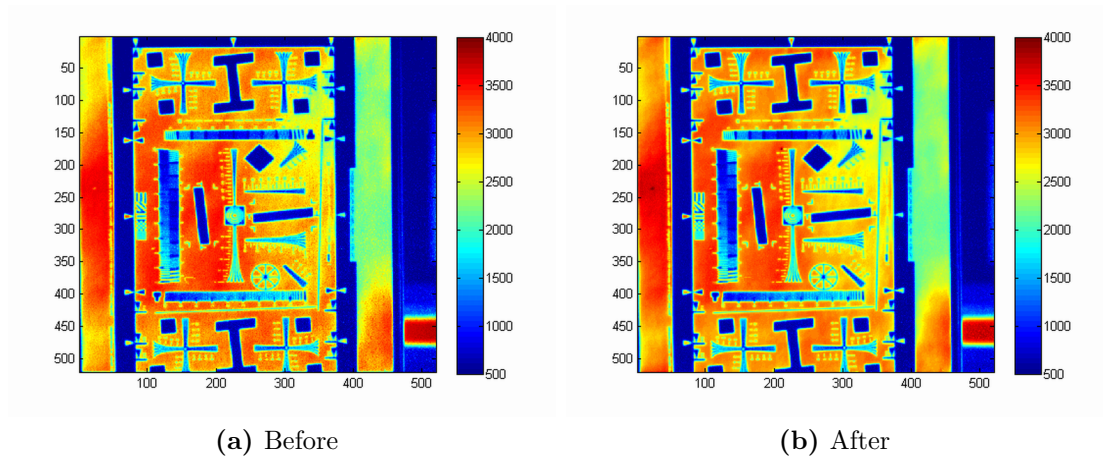
Figure 4.36: Flat field correction of an image taken with Vanilla.

Applying pedestal subtraction and CM correction techniques consecutively also dramatically reduces the noise of the sensor. Fig. 4.34 compares the noise of the sensor from 150 frames with different corrections. The correction applied reduces the noise of the sensor from 60 e^- to 28 e^- in analog mode with hard reset.

Flat field correction

The correction method described above removes FPN to a large extent. However, real time application of both pedestal subtraction and CM correction imposes extensive additional computational requirements. At the same time, this type of CM correction can be applied only for particle detection with very low occupancy, *e.g.* protons, α-particles, MIPs, *etc.* It is not suitable for imaging applications due to the nature of the algorithm.

Flat field correction (see Section 3.2.11, page 44) is an alternative to the pedestal subtraction technique and is applicable to real time imaging. The flat field image was calculated as a mean of 150 frames. A diffusion sheet was placed in front of the sensor, which was uniformly illuminated in the middle of its dynamic range ($\approx 2500\ DN$). Once the flat field image is obtained, it can be applied to
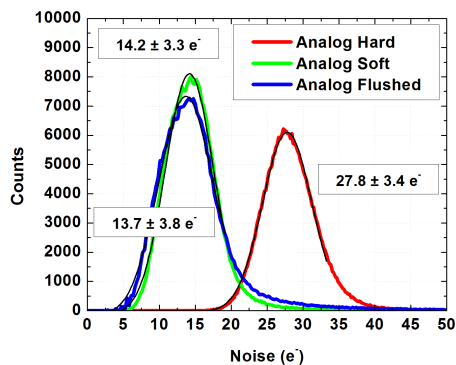
Figure 4.37: Vanilla noise distribution for analog mode with hard, soft and flushed reset.
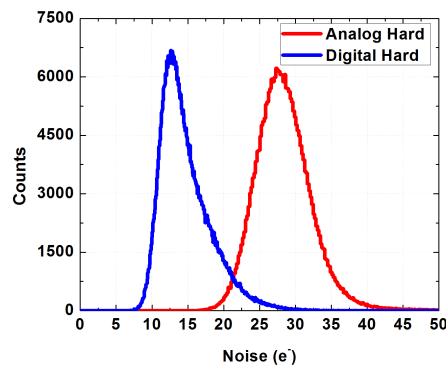
Figure 4.38: Vanilla noise distribution for analog and digital with hard mode of reset.

an imaging measurement. Fig. 4.36 demonstrates a comparison between raw and flat field corrected image. The latter shows much smoother transition between colour tones and the image looks less "grainy". The flat fielding was also applied to dark frames and the noise and FPN was calculated. The FPN after correction is similar to the pedestal subtraction, however the sinusoidal pattern remained clearly visible. The noise level of the sensor is $\approx 60~e^-$ and similar to the raw frame noise as expected.

Read noise

The noise of the sensor was calculated from 150 frames as described in Section 3.2.8, page 42, neglecting the first several frames that deviate more than 1% from the saturation level (see Section 4.2.2, page 89). Pedestal subtraction and common mode noise correction were also applied before the noise calculation, giving the best achievable noise level. Fig. 4.37 compares noise for Vanilla MAPS working in analog mode with three types of reset. As was anticipated, the highest noise level is measured with hard reset, which is dominated by the reset kTC noise. The lowest noise of $14~e^-$ is achieved by utilising either soft or flushed reset. The latter however benefits from suppressed image lag.
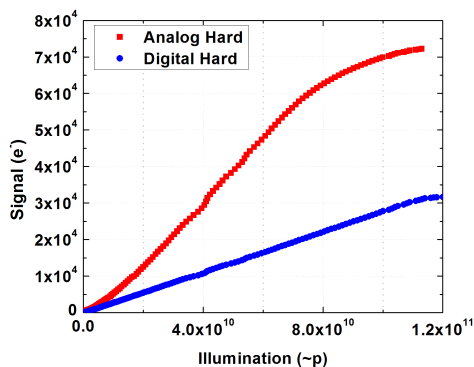
Figure 4.39: Vanilla linearity for analog and digital mode with hard reset.
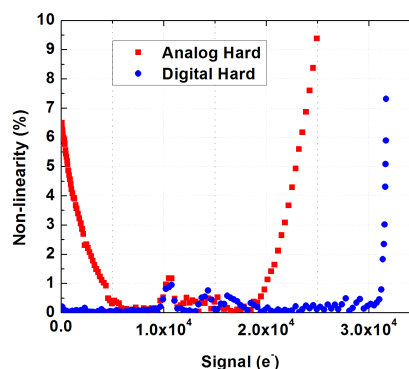
Figure 4.40: Vanilla non-linearity for analog and digital mode with hard reset.

The mean noise level in digital mode is lower for all types of reset and considerably lower with hard reset. However, common mode correction did not remove all the components of systematic noise present in digital mode. Thorough analysis of different possible noise components suggests that the noise is uncorrelated and does not follow a Gaussian distribution, having a "tail". This cannot be easily subtracted (Fig. 4.38).

Noise was also compared between the 20 μm and 14 μm epi-layer versions of the sensor. The measurements demonstrated that the mean noise level and the FPN of both sensors do not depend on the thickness of the sensitive layer, making the 20 μm sensor attractive for HEP applications demanding low noise.

Linearity

The linearity of the sensor was compared in analog and digital mode with hard reset. Fig. 4.39 shows the signal of the sensor in e^- vs. number of incident photons on the sensor. Digital mode demonstrates significantly better linear behaviour over a broader incident photon number range. The non-linearity is quantified in Fig. 4.40. In digital mode it does not exceed 1% before the sensor reaches saturation of the signal.
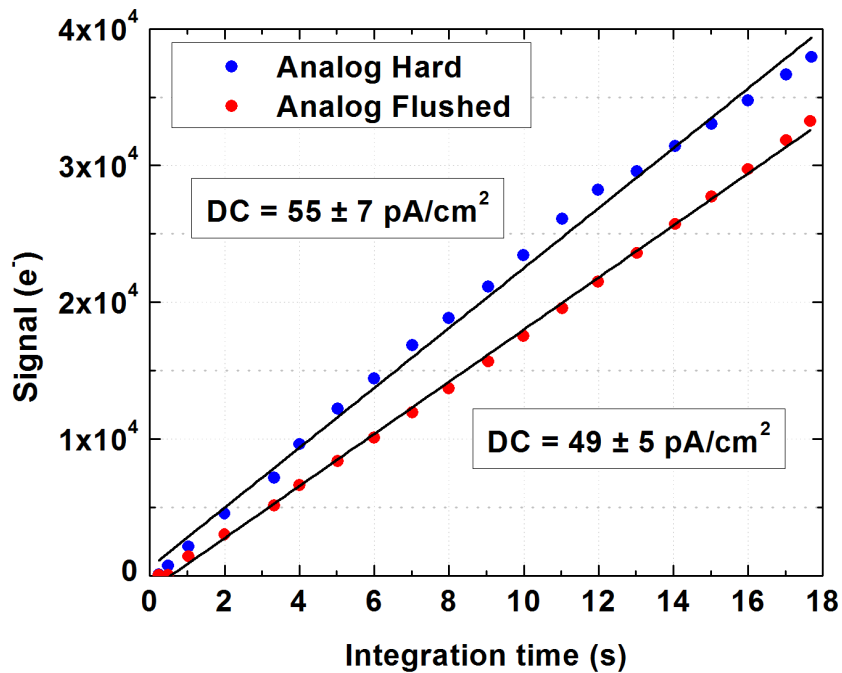
Figure 4.41: Vanilla dark current for analog mode with hard and flushed reset.

Dark current

The dark current of the sensor was measured in analog mode with hard and flushed reset (Fig. 4.41). The data was accumulated at room temperature. The dark current of the sensor was found to be $\approx 50\ pA/cm^2$ and independent of the of the pixel reset type applied.

Spectral response

A spectral response measurement was carried out for the $20\ \mu m$ epi-layer Vanilla. The sensor was placed in a light tight box. An optical fibre was used to guide the light from the light source to the monochromator and then to the sensor. A light de-intensifying filter was used to reduce the intensity of the light source. The scan was performed using light with wavelengths in the range between $200\ nm$ and $800\ nm$. A calibrated photo diode was used to measure the light output of
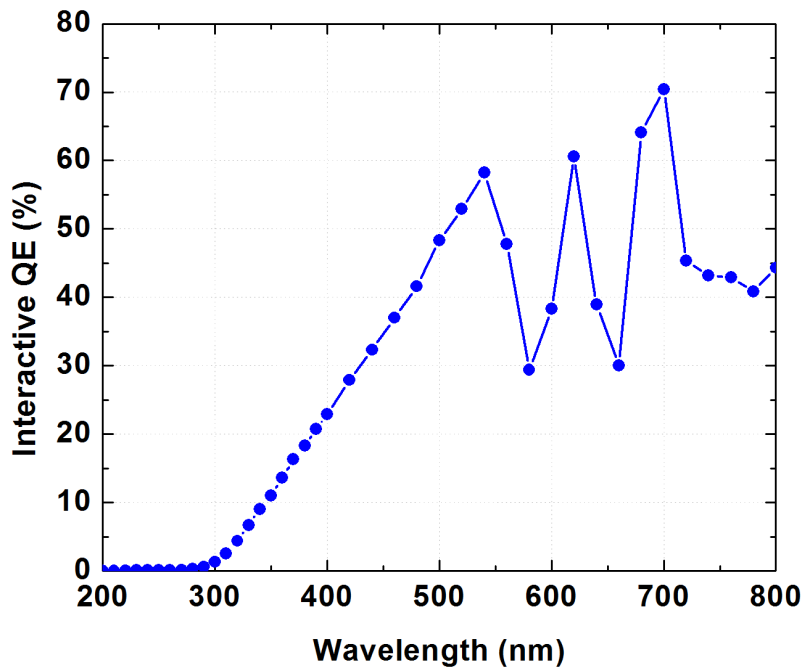
Figure 4.42: Vanilla spectral response.

the system at different wavelengths. The interacting quantum efficiency (QE) of
the Vanilla sensor was calculated as described in Sec. 3.2.9. The resulting plot
is shown in Fig. 4.42. The peak QE reaches 52% at 520 nm. The QE drops
in UV region (below 350 nm) due to the high absorption of UV photons in the
transistors and metal layers of the sensor. The photons in the near infrared region
pass the epi-layer and have higher probability to be absorbed in the bulk, giving
reduced QE as well.

Operation stability

The Vanilla acquisition system was tested for stability of operation over a long
time period [57]. This is required for several potential applications of the sensor,
including autoradiography [58] and astronomy [59]. A module for the Labview
readout interface was developed that allows continuous data acquisition with a
variable time delay between runs. Mean dark values were calculated by averaging
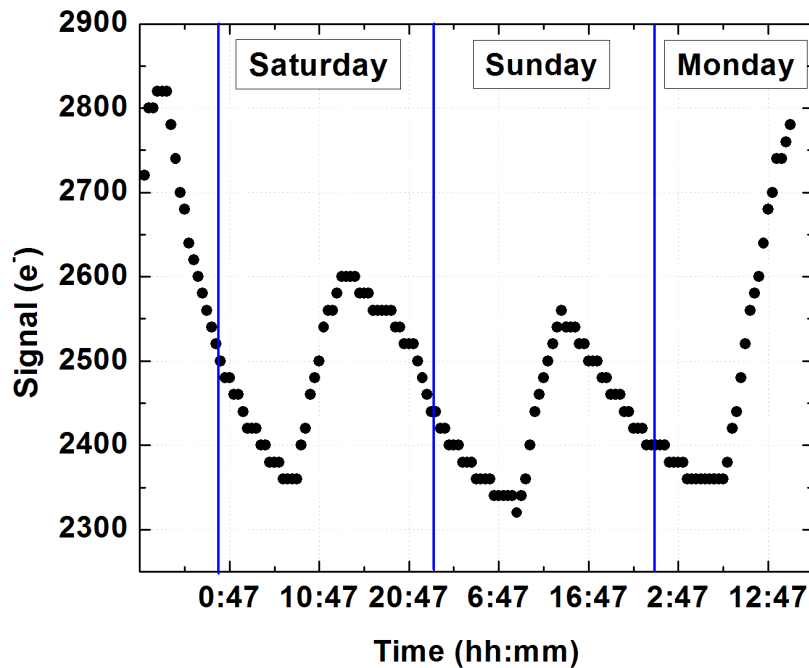
Figure 4.43: Vanilla long-time operation stability.

50 frames taken every 30 minutes for 72 hours. There was no indication that the acquisition system developed has any stability issues. The result presented in Fig. 4.43 shows a small variation of 15% in the mean dark value. It is attributed to the change in the ambient temperature of the sensor and repeats daily. This is explained by the variation of leakage current in the pixel, which doubles for every 7 K temperature increase in silicon [45]. Two higher peaks at the beginning and at the end of the acquisition show that the lab heating was turned off during the weekend when the measurement took place. The results obtained suggest temperature correction algorithms have to be applied for high accuracy experiments, unless a suitable chamber is used to maintain constant temperature.

4.2.3 Back-thinned Vanilla

Back-thinning is the process by which a sensor is mounted upside down on a supporting substrate and the bulk silicon is removed. This allows incident photons to directly reach the sensitive epi-layer avoiding intervening oxide, metal and transistor layers. The back-thinning dramatically improves quantum efficiency of the sensor in the UV region.

A typical thinning process starts with mounting a wafer with set of sensors upside down on a supporting wafer. The substrate is then mechanically ground down in a fast rough grind. This is followed by a slower fine grind step. In order to remove the damage induced, a wet/dry etch is applied after the grinding. The Vanilla sensor was back-thinned by e2V Technologies [60].

The back-thinned Vanilla was fully characterised in analog mode with flushed reset and the performance parameters were compared to a standard 20 μm epi-layer version of the sensor.
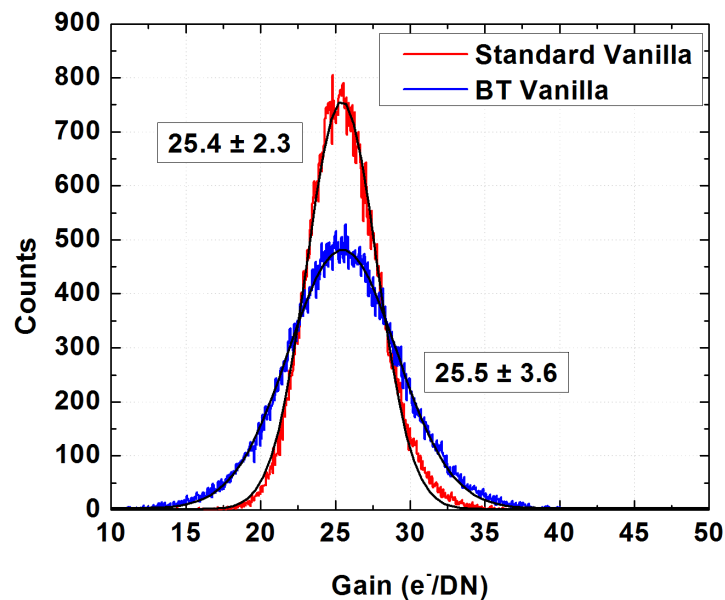
Figure 4.44: Gain distribution for standard and BT Vanilla in analog flushed mode.

Gain

The PTC curves were produced for both sensors as described in Section 3.2.2, page 35, from 50 illumination steps with 100 frames per step. The average PTC was calculated for each of the sensors and the boundaries for the fit in the shot noise limited region were determined. Finally, a pixel-by-pixel PTC was created for the full frame. The gain distribution across the pixel matrix can be seen in Fig. 4.44.

The back-thinning procedure does not strongly influence the gain of the sensor, which changed by 3%, a margin which is within the error of calculation. However, the gain FPN increased, suggesting that the back-thinning affects the uniformity of the conversion constant of the pixel matrix.

Noise

The back-thinned Vanilla was compared to the standard one in terms of noise and dark FPN. The data was accumulated from 150 frames, taken under the same ambient conditions and readout system settings. The sensor noise is slightly higher for the back-thinned version (see Fig. 4.45), while the dark FPN remains almost the same for both variants of the sensor.

Dark current

The data for the dark current measurement were accumulated for the range of integration times between 250 ms and 18 s as described in Section 3.2.7, page 41. The comparison results obtained show that the dark current almost doubles from 49 to 87 pA/cm^2 for the back-thinned version of the sensor in comparison to the standard one (Fig. 4.46). During the back-thinning process the substrate of the sensor is removed up to the epi-layer. This causes some surface damage to the charge sensitive area, which increases the surface leakage current. The contribution of this increased current gives rise to the total leakage through the pixel.

Spectral response

Back-thinning and back illumination of the CMOS sensor is the most efficient way to increase its sensitivity to UV light. The comparison of the quantum efficiency between back-thinned and standard Vanilla was performed for the wavelength range between 200 and 500 nm. The back-thinned version of the sensor showed a considerable increase in interactive QE for the wavelengths below 380 nm (Fig. 4.47). Standard Vanilla becomes insensitive at smaller wavelengths due to the absorption of the UV photons in the transistor layers of the sensor. The back-thinned sensor is illuminated from the back side, therefore incident blue photons can reach the sensitive epi-layer more effectively. The interactive QE in the UV region of the spectrum was found to be between $10 - 20\%$.

4.2.4 Vanilla conclusions

Vanilla MAPS was fully characterised. The sensor was designed to evaluate several novel technologies. It features three types of pixel reset as well as analog and digital readout modes. Table 4.8 compares the key sensor parameters for three types of reset as well as the digital hard readout mode. The read noise
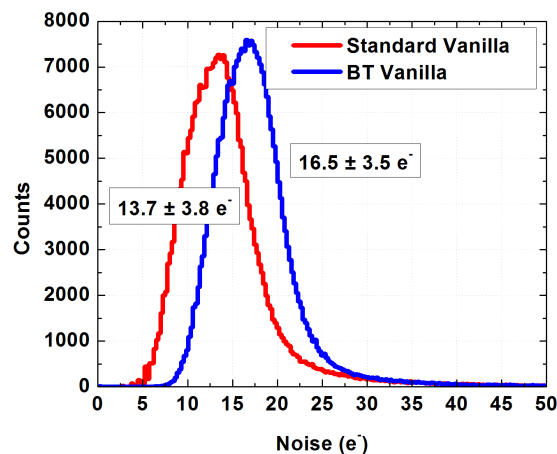
Figure 4.45: Noise distribution for standard and BT Vanilla in analog flushed mode.
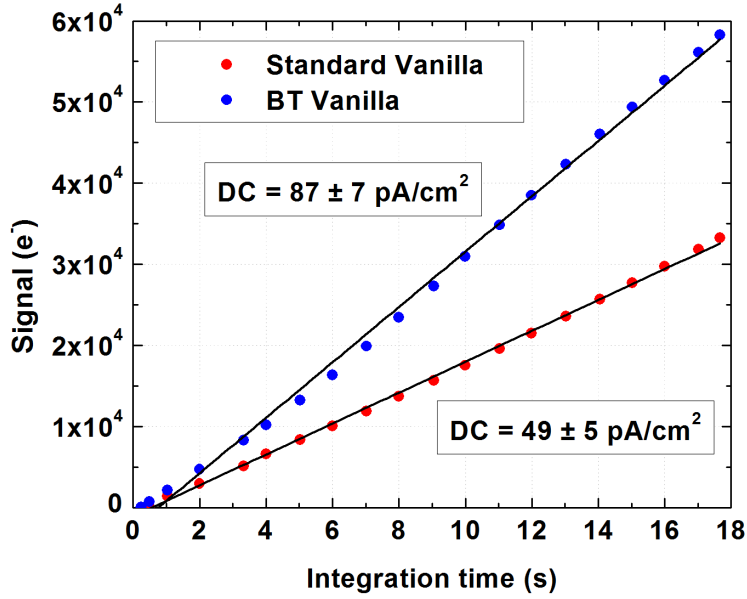
Figure 4.46: Dark current comparison for standard and BT Vanilla in analog flushed mode.

Performance parameter	Analog Hard	Analog Soft	Analog Flushed	Digital Hard	Units
Gain	20 ± 3	25 ± 4	26 ± 4	8 ± 3	e^-/DN
Read noise	28 ± 3	14 ± 4	14 ± 4	12 ± 4	e^-
Dark current	55 ± 7	-	49 ± 5	-	pA/cm^2
Full well capacity	50000	62000	65000	24000	e^-
Dynamic range	63	62	61	70	dB
Non-linearity	< 5	-	≈ 5	< 1	$\%$
QE @ 520 nm	52	-	-	-	$\%$

Table 4.8: Key performance parameters of the Vanilla MAPS.

using flushed reset was found to have halved in comparison to the hard one, while the image lag was considerably reduced. The sensor read noise can be lowered by a factor of three if noise reduction algorithms are applied. For real time or imaging applications, flat fielding can be effectively applied to correct the fixed pattern noise.

The digital readout mode demonstrated lower noise, higher dynamic range and very high linearity. At the same time on chip ADCs enable readout speeds
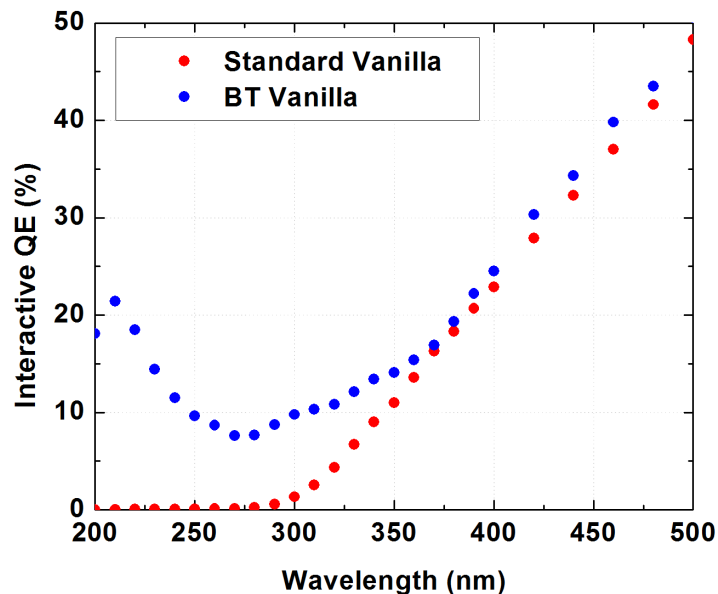
Figure 4.47: Spectral response comparison between BT and standard Vanilla in analog flushed mode.

Performance parameter	Standard Vanilla	BT Vanilla	Units
Gain	26 ± 4	26 ± 4	e^-/DN
Read noise	14 ± 4	17 ± 4	e^-
Dark current	49 ± 5	87 ± 7	pA/cm^2
Full well capacity	65000	66000	e^-
Dynamic range	61	60	dB
Non-linearity	5	6	$\%$
QE @ 520 nm	52	53	$\%$
QE @ 220 nm	0	20	$\%$
Fill factor	75	100	$\%$

Table 4.9: Key performance parameters comparison between BT and standard Vanilla in analog flushed mode.

as fast as 150 frames per second, even though the region of interest readout is unavailable for digital mode by design.

Back-thinned Vanilla was fully characterised in analog mode with flushed reset. The results were compared to the standard version of the sensor working under similar ambient conditions with the same parameters. The comparison

of the performance parameters is shown in Table 4.9. The back-thinning of the Vanilla MAPS has not dramatically degraded the performance of the sensor. Parameters of the sensor such as non-linearity, dynamic range and full well capacity remained unchanged. However, a slight degradation in noise performance was observed. This was attributed to increase in the dark current of the detector resulting from the thinning process. The back-thinned sensor was found to have almost double the dark current. The interactive QE dramatically increased in the UV wavelength region, which makes the sensor very attractive for applications requiring UV sensitivity.

4.3 eLeNA

eLeNA (e^- Low e^- Noise APS) is the most recent parametric sensor designed by the Microelectronics Design Group at RAL. It employs a novel 0.18 μm INMAPS CMOS (Isolated N-well) fabrication process. This allows nMOS and deep p-well shielded pMOS transistor implementation in the pixel structure. This permits more complex pixel architectures to be implemented, while the shielding prevents unwanted charge collection. The sensor features 15×15 μm pixels and has two epi-layer thicknesses, 5 and 12 μm. There are four groups of test structures implemented in the sensor. All but one are devoted to evaluation of different approaches for noise reduction. The other has standard 3MOS architecture and provides a benchmark.

4.3.1 INMAPS technology

The INMAPS process is a standard 0.18 μm CMOS imaging sensor technology with the addition of high energy deep p-well implants [61]. The use of pMOS transistors in conventional MAPS is limited due to the fact that charge generated in the epi-layer should be collected in the n-well of the transistor (see Section 2.3.2, page 22). Therefore, the presence of pMOS would split generated charge dramat-
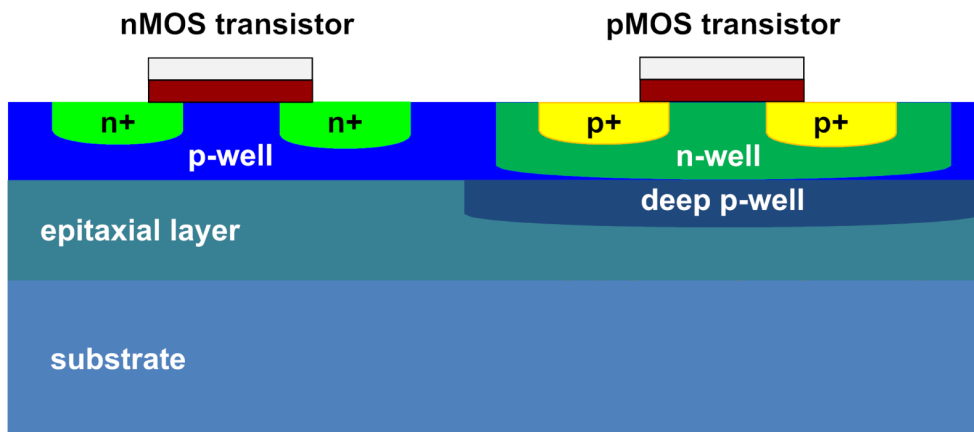
Figure 4.48: CMOS MAPS pixel cross-section implemented in INMAPS technology.
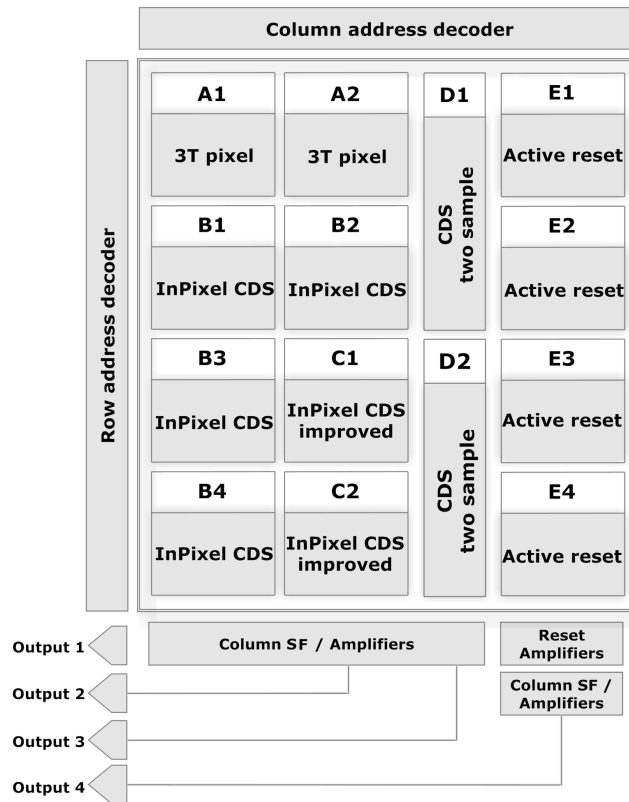
Figure 4.49: eLeNA general readout floorplan.

ically. By implanting the deep p-well under the pMOS device area (Fig. 4.48), charge generated in the epi-layer is reflected and can only be collected by the photo diode. The use of pMOS devices extends the functionality, which can then be implemented at the pixel level, while reducing the power consumption (see Section 2.4, page 2.4). It should be noted that the additional deep implant must not be too small to shield the n-well completely. This imposes limitations on the pixel size and therefore affects the suitability of this technology for applications demanding small pixel pitch.

4.3.2   eLeNA pixel architectures

The sensor organisation is shown in Fig. 4.49. There are 14 different pixel configurations which are split into four groups, each with its own output providing the option of independent readout. Group A consists of a standard 3MOS pixel de-

sign and is used as a reference for parameter characterisation. Group B features simple in-pixel Correlated Double Sampling (CDS). Group C includes improved CDS pixels, while Group D employs a novel "CDS two sample" architecture. Finally, Group E has active reset architectures with in-column reset amplifiers. The test structures A, B, C and E feature 128×128 pixels, while structure D is 256×64 pixels. A more detailed description of the pixel architectures is given in the following sections.

Group A: 3MOS conventional pixel

Two different 3MOS layouts were implemented (A1 and A2). The A1 layout was provided by the sensor foundry and features a standard diode with $\approx$ 67% fill factor. A2 is a typical 3MOS pixel implemented with standard transistors and a n-well p-substrate diode. This group of pixels allows the INMAPS technology evaluation and a direct comparison of the standard 3MOS pixel with more sophisticated noise reduction architectures.

Group B: in-pixel CDS

The schematic of the InPixel CDS pixel is shown in Fig. 4.50. It consists of the photo diode with capacitance C_d, its reset M_{rst}, two source followers, a coupling capacitor C_{coupl}, second reset switch and the row access transistor M_{sel}. When the $Reset1$ is applied, the coupling capacitor C_{coupl} between the two source followers is also held in reset (Fig. 4.51). At time T_1 the kTC noise from M_{rst} is stored on the photo diode capacitance, and is also presented as an offset between the C2 capacitor terminals. When the second reset ($Reset2$) is released (T_2), the reset sample from the diode node is stored on both sides of the capacitor. At the end of the integration period, the diode voltage, which retains the diode reset sample and the relevant signal, is read out through the coupling capacitors. As the reset sample from the diode was already stored but on the opposite side of the capacitor, effective cancellation of the reset sample is performed. As was
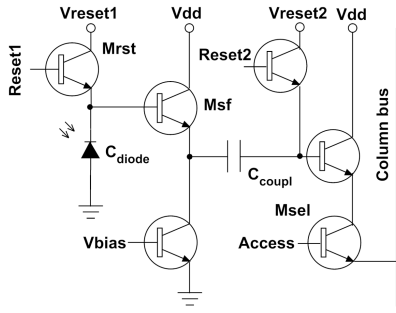
Figure 4.50: In-pixel CDS (group B) pixel architecture.
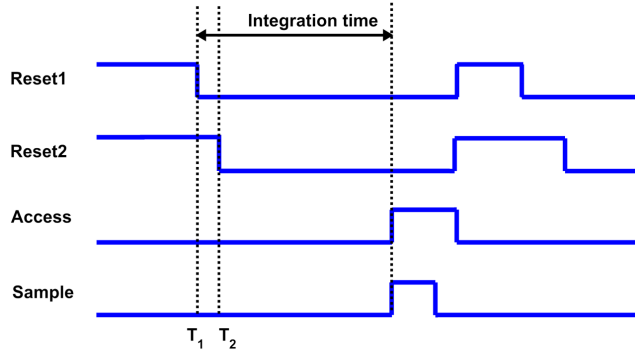
Figure 4.51: In-pixel CDS (group B) pixel timing diagram.

shown in [62], the overall reset noise is reduced by a factor $\sqrt{C_{coupl}/C_{diode}} \cdot A_{SF1}$, where A_{SF1} is the gain of the first source follower M_{sf}. Note that by swapping the falling edges of the reset signals, the CDS operation can be cancelled and the full kTC noise is presented at the output, allowing direct comparisons.

The noise reduction factor suggests that an increase of the coupling capacitance reduces the noise. However, addition of the extra capacitor in the pixel also introduces another source of kTC noise, so the size of the capacitor has to be balanced. There are four different pixel configurations implemented, which vary in coupling capacitor and photo diode sizes. The summary is given in Table 4.10.

The architecture of Group B pixels is expected to suffer from some inherent drawbacks. The extra source follower combined with the single ended readout makes this architecture more prone to pixel-to-pixel non-uniformities. The second problem comes from the increased leakage current in the pixel, which comes from both source follower transistors as well as the coupling capacitor. The design also makes the first source follower transistor active at all times making the architecture less power efficient. The fill factor of the sensor suffers due to increased number of devices per pixel, but this can be overcome by back-thinning. To tackle some of the above mentioned limitations the Improved InPixel CDS architecture is introduced.

Pixel	Comments on layout	Fill factor
B1	NMOS gate capacitor, standard NMOS diode	$\approx 29\%$
B2	Accumulation capacitor, standard NMOS diode	$\approx 35\%$
B3	NMOS gate capacitor, ip-diode	$\approx 29\%$
B4	MIM capacitor, standard NMOS diode	$\approx 9\%$

Table 4.10: In-pixel CDS (group B) pixel implementation summary.

Group C: improved in-pixel CDS

In this group of pixels an additional switch is introduced (Fig. 4.52). This allows the first source follower to be active only when needed, reducing the leakage current as well as the power consumption in comparison to Group B. The C1 matrix comes with the accumulation coupling capacitor and $\approx$ 35% fill factor while the C2 pixels have MIM capacitor and $\approx$ 8% fill factor.
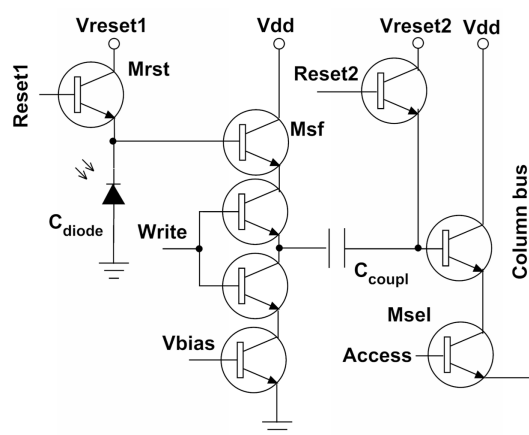
Figure 4.52: Improved in-pixel CDS (group C) pixel architecture.

Group D: two sample CDS

The two sample CDS test structure implements the concept of reading out the reset value before the photo diode and the off-pixel subtraction (Fig. 4.53). The reset value is sampled on an in-pixel storage capacitor by pulling the write transistor high just after the reset occurs (Fig. 4.54). The reset value is sampled to the column level capacitor at the end of the integration time and then the photo diode voltage with reset is sampled as well. The two stored values are read out in parallel, where the off-chip differential amplifier provides the difference of two values. This approach gives true CDS readout with the reset kTC noise reduced. Two variants of the structure were produced, with the only difference being the size of the in-pixel sampling
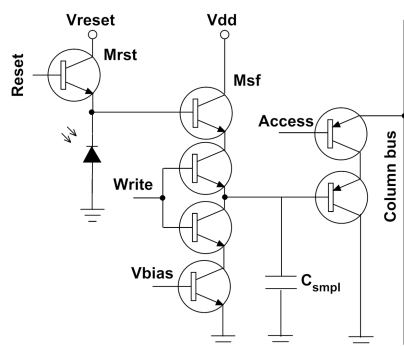
Figure 4.53: Two sample CDS (group D) pixel architecture.
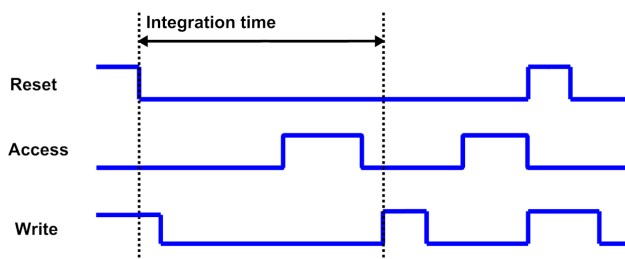
Figure 4.54: Two sample CDS (group D) pixel timing diagram.

capacitor. The disadvantages of this structure include reduced readout time due to double pixel readout, increased pixel complexity, small fill factor ($\approx 8\%$) and possible additional current leakage through the capacitor. However, this test structure eliminates FPN to a higher extent since it takes into account all the pixel component mismatches.

Group E: active reset

The active reset architecture is another way of reducing the reset noise. The principal pixel diagram is depicted in Fig. 4.55. This architecture was first proposed in [63] and then improved in terms of image lag suppression in [64]. It is based on the amplification of the feedback capacitance and hence the increase in the effective capacitance on the photo diode during the reset because of the Miller effect. This dramatically reduces the reset noise, bringing the kTC noise down to the level of the in-pixel transistor noise. At the same time, the diode capacitance is not affected during the integration and readout time and therefore the source follower charge to voltage conversion gain remains high.

The readout of the pixel starts as in the standard 3MOS sensor (see Section 2.5.2, page 28), as at this stage the feedback circuitry is disconnected. Following this, the reset is accomplished in two stages – the "hard reset" is followed

Figure 4.55: Active reset (group E) pixel architecture.

Figure 4.56: Active reset (group E) timing diagram.

by the "feed-back reset". The hard reset occurs when the M_{flush} and M_{init} transistors are clocked high (Fig. 4.56), pulling the photo diode voltage to V_{reset}. The column feedback is then activated by the feedback switch. The operational amplifier reference voltage, V_{dd}, is controlled by the RC-network. As it charges up, the amplifier continuously adjusts the feedback reset voltage to hold the differential input of the amplifier at virtual ground. The photo diode voltage does not reach V_{dd} and the "feedback reset" of the pixel occurs. Taking the Miller effect into account the equivalent effective capacitance of the pixel decreases, giving reduced reset kTC noise.

4.3.3 eLeNA optical characterisation

The characterisation of the sensor was performed at RAL, using a commercial custom setup [65] similar to one described in Section 3.2.1, page 34, and the procedure employed for the previously described sensors, HEPAPS4 and Vanilla. The measurements were accomplished on an evaluation board which uses one ADC operating at a 1 MHz sampling rate. The board was based on discrete components in order to minimise the noise contribution of the evaluation readout

Figure 4.57: eLeNA read-out board linearity.
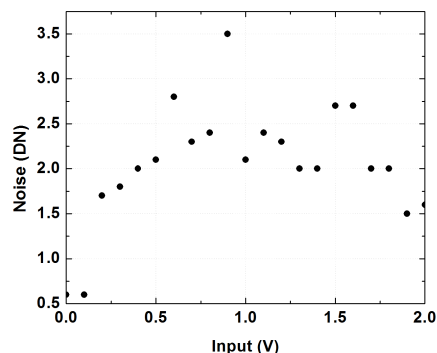
Figure 4.58: eLeNA read-out board noise.

system. The design of the board allows its characterisation in terms of linearity and thermal noise, both of which were measured and accounted for during the test structure characterisation. The eLeNA sensor comes in two variants with $5 \ \mu m$ and $12 \ \mu m$ epi-layer thicknesses. Both variants were fully characterised for gain, noise, linearity, dynamic range and QE.

The readout parameters for all test structures were set to default values extracted from the design simulations. In the following sections only major results are highlighted along with a discussion of the most interesting details.

Readout board evaluation

The eLeNA sensor was designed to achieve single digit electronic noise. In order to achieve this, not only the sensor but also the readout electronics has to have the same or lower order of magnitude noise level, which has to be estimated and taken into account for the sensor measurements. The design of the board made linearity and noise testing possible. Fig. 4.57 shows the dependence of the output signal on the input. The system behaves linearly for input voltages between $0 \ V$ and $1.7 \ V$, which covers almost the whole range of pixel output voltages. The noise of the board is shown in Fig. 4.58. The result show that the board noise is not strongly dependent on the input voltage sweep.
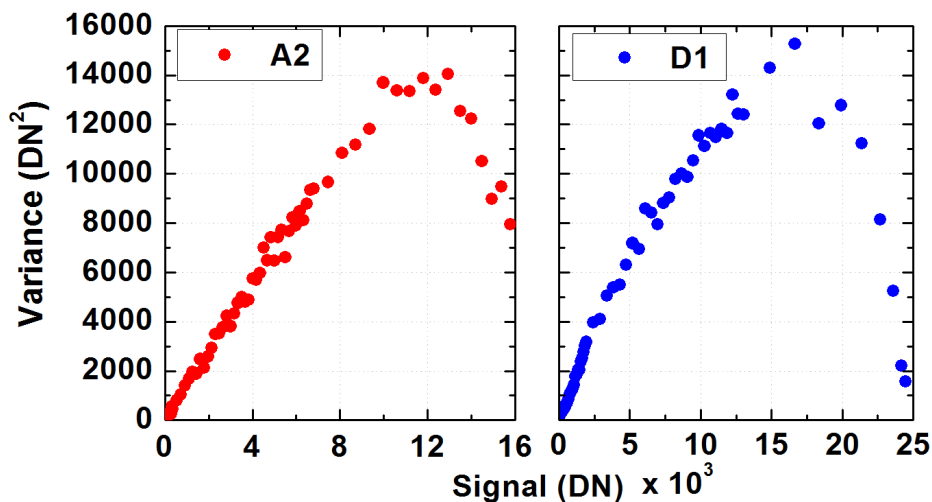
Figure 4.59: Example of averaged PTC for A2 and D1 test structures.

Gain

The gain measurements were performed for all test structures in two stages. The average PTC was plotted and the rough gain was estimated. At the same time this allowed the careful selection of the fit region for the pixel-by-pixel PTC as some test structures showed a large deviation from the linear dependence in the shot noise limited region. Fig. 4.59 shows an example of such a behaviour for D1 test structure as well as an "ideal" PTC plot for A2. Pixel-by-pixel PTC is calculated after the fit region is determined. Fig. 4.61 summarises the gain values for different test structures. All variants of the pixel design show Gaussian-like gain distribution across the matrix indicating an excellent uniformity between pixels for most architectures in this respect. However, $\sim 10\%$ D1 and D2 pixels show significant deviation from the mean value (Fig. 4.60), which is associated with several misbehaving rows at the edge of the structure.

Noise

The noise was calculated using the same method as for the other two sensors. A series of dark frames were taken, with the standard deviation from the mean
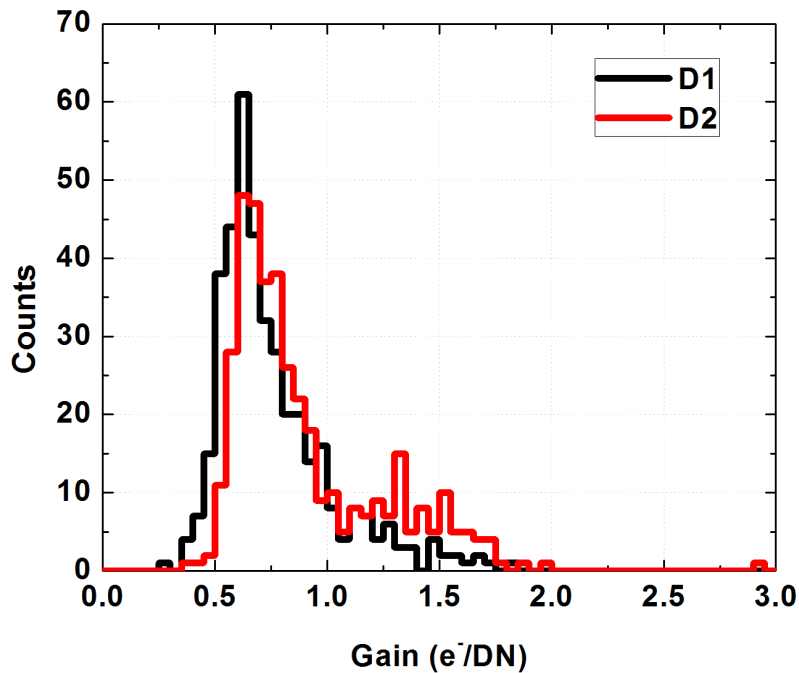
Figure 4.60: Example of gain distribution for D1 and D2 test structures.

value for each pixel giving the noise on that pixel. The result is presented in the form of a histogram. Fig. 4.62 shows a summary of the noise measurements for the test structures. All designs show acceptable noise level and do not exceed 27 e^- even for the standard 3T pixel. Group B and C show very similar noise values, apart from B3 which is $\sim 40\%$ better as a result of a combination of slightly higher gain and lower noise (in ADC units). At the same time these values are within the error from one of the benchmark test structures. Groups D and E demonstrate sub-ten electrons noise making these test structures the most promising in terms of noise performance.

The sensor was also characterised for the dark FPN (see Section 3.2.6, page 40). Fig. 4.63 summarises these results. Pixels of group B and C show relatively high FPN due to the drawbacks described in Section 4.3.2, page 108. Exceptionally low dark FPN is achieved by group D as was anticipated in Section 4.3.2, page 110. This makes such a design combined with the back-thinning process

Gain (e⁻/ADC)

A1	3T	A2	3T			E1	Active reset
	0.42 ± 0.16		0.72 ± 0.08	D1	CDS 2 sample		N/A
B1	InPixel CDS	B2	InPixel CDS		0.76 ± 0.26	E2	Active reset
	0.84 ± 0.11		0.82 ± 0.13				0.73 ± 0.45
B3	InPixel CDS	C1	InPixel CDS improved			E3	Active reset
	0.54 ± 0.09		0.84 ± 0.11	D2	CDS 2 sample		N/A
B4	InPixel CDS	C2	InPixel CDS improved		0.91 ± 0.30	E4	Active reset
	0.76 ± 0.16		0.80 ± 0.13				N/A

Figure 4.61: Summary of the gain performance for eLeNA sensor.

Noise (e⁻)

A1	3T	A2	3T			E1	Active reset
	18 ± 3		27 ± 2	D1	CDS 2 sample		N/A
B1	InPixel CDS	B2	InPixel CDS		6 ± 2	E2	Active reset
	16 ± 4		15 ± 4				8 ± 2
B3	InPixel CDS	C1	InPixel CDS improved			E3	Active reset
	10 ± 2		14 ± 4	D2	CDS 2 sample		N/A
B4	InPixel CDS	C2	InPixel CDS improved		9 ± 3	E4	Active reset
	16 ± 4		14 ± 4				N/A

Figure 4.62: Summary of the noise performance for eLeNA sensor.

Dark FPN (e⁻)

A1	3T	A2	3T			E1	Active reset
	215		10	D1	CDS 2 sample		N/A
B1	InPixel CDS	B2	InPixel CDS		20	E2	Active reset
	295		305				110
B3	InPixel CDS	C1	InPixel CDS improved			E3	Active reset
	175		325	D2	CDS 2 sample		N/A
B4	InPixel CDS	C2	InPixel CDS improved		25	E4	Active reset
	250		310				N/A

Figure 4.63: Summary of the dark FPN performance for eLeNA sensor.

very promising for charged particle detection [66].

The comparative analysis of sensors with two epi-layer thicknesses revealed that FPN is very similar for both versions, while the noise tends to be $10 - 20\%$ lower for devices on the 12 μm epi-layer.

Full well capacity (e⁻)

A1 3T		**A2** 3T				**E1** Active reset
9500		8600		**D1** CDS 2 sample		N/A
B1 InPixel CDS		**B2** InPixel CDS		12500		**E2** Active reset
18700		18500				25000
B3 InPixel CDS		**C1** InPixel CDS improved				**E3** Active reset
23700		17300		**D2** CDS 2 sample		N/A
B4 InPixel CDS		**C2** InPixel CDS improved		12200		**E4** Active reset
17100		17500				N/A

Dynamic Range (dB)

A1 3T		**A2** 3T				**E1** Active reset
54		50		**D1** CDS 2 sample		N/A
B1 InPixel CDS		**B2** InPixel CDS		66		**E2** Active reset
62		62				70
B3 InPixel CDS		**C1** InPixel CDS improved				**E3** Active reset
72		63		**D2** CDS 2 sample		N/A
B4 InPixel CDS		**C2** InPixel CDS improved		62		**E4** Active reset
61		62				N/A

Figure 4.64: Summary of the full well capacity performance for eLeNA sensor.

Figure 4.65: Summary of the dynamic range performance for eLeNA sensor.

Full well capacity and dynamic range

The full well (FW) capacity and dynamic range (DR) were calculated as described in Section 3.2.3, page 37. The test structures B, C and E demonstrate a relatively high ability to hold the charge in the pixel, while the FW for D structure is almost twice as low (Fig. 4.64). However, group D has the lowest noise, which compensates for the DR. Fig. 4.65. This parameter is uniform across the sensor and reaches the highest value of 72 dB for B3.

Linearity

The linearity of the sensor was measured by varying the illumination level while keeping the integration time constant (see Section 3.2.4, page 38). Both the A2 and B2 groups of pixels show very linear behaviour up to the full well. B4 test structure suffers quite a sharp bend at 9000 e^- (Fig. 4.66). This is associated with the pronounced inherent gain non-linearity (discussed in Section 3.2.4, page 118), which can be observed from the average PTC, where the shot noise limited region also bends after 9000 e^-. The non-linearity of the group C and D becomes
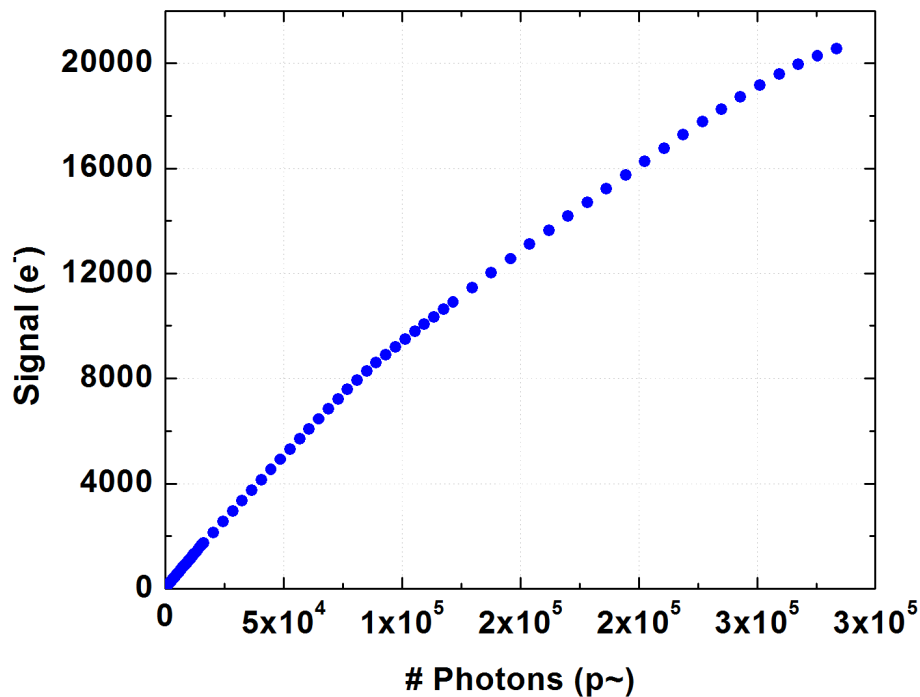
Figure 4.66: Linearity of the B4 test structure.

excessive only after the full well when the sensor saturates.

Signal-to-noise performance

The signal-to-noise performance of the sensor was calculated for each illumination level as for the HEPAPS4 and Vanilla and presented in dB. Fig. 4.67 shows a typical response. The SNR is low at small illumination levels and reaches its maximum at saturation. Values between 35 dB for E2 structure and 44 dB for C and D at full well are obtained for all tests structures. The maximum values exceed $55 - 60$ dB for almost all devices.

Quantum efficiency

The quantum efficiency (QE) estimation was accomplished in a slightly different way in comparison to Vanilla (see Section 4.2.2, page 97). A broad range light
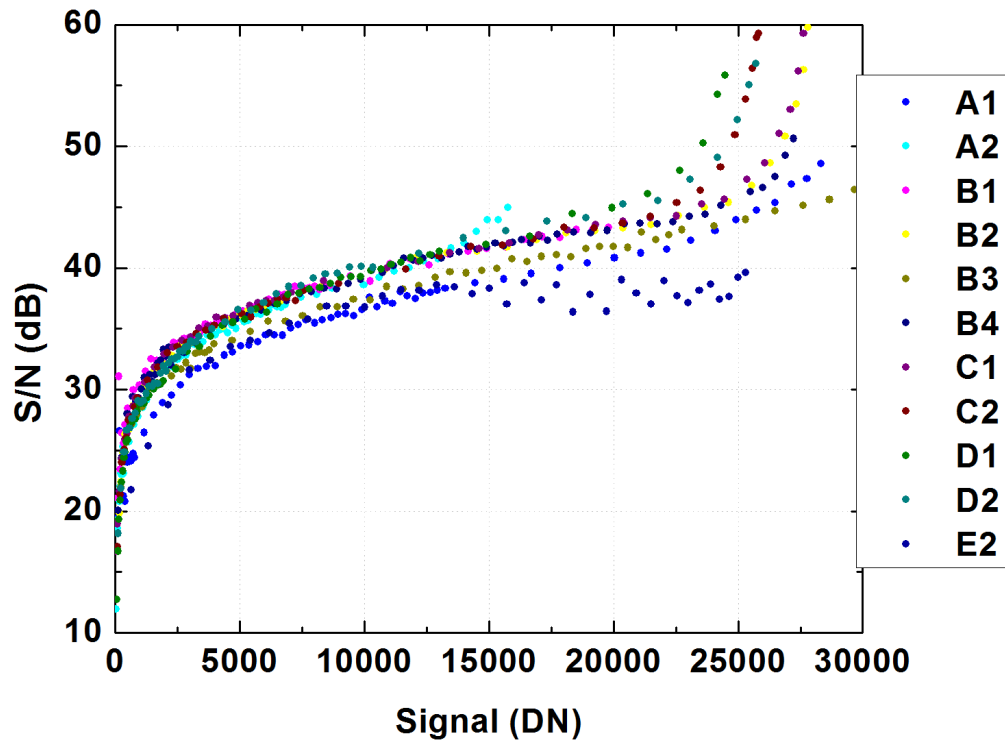
Figure 4.67: Signal-to-noise performance for eLeNA sensor.

emission lamp and monochromator were not available for the setup provided. Blue (470 *nm*), green (546 *nm*) and red (635 *nm*) LEDs were used instead. Fig. 4.68 shows an example of the quantum efficiency results for all pixel groups characterised at green wavelength. Most of the test structures show reasonably high QE. However, it tends to be low for pixels with small fill factor, *e.g.* D1 and D2. It was also noticed that the QE gets worse for pixels with metal capacitors such as C2.

The comparison between the two epi-layer thicknesses did not show any significant discrepancy in QE, which indicates that most of the visible light photons are absorbed either in electronics or within the first 5 *μm* of the epi-layer. However, this is not the case for soft X-rays or charged particles, where the thickness of epi is crucial for effective particle detection.

Quantum efficiency (%)

A1 3T		**A2** 3T			**E1** Active reset	
R 41 G 45 B 27		R 36 G 37 B 27	**D1** CDS 2 sample		N/A	
			R 3 G 4 B 4			
B1 InPixel CDS		**B2** InPixel CDS			**E2** Active reset	
R 25 G 29 B 20		R 25 G 40 B 20			R 20 G 13 B N/A	
B3 InPixel CDS		**C1** InPixel CDS improved			**E3** Active reset	
R 44 G 46 B 36		R 42 G 55 B 46	**D2** CDS 2 sample		N/A	
			R 1 G 1 B 1			
B4 InPixel CDS		**C2** InPixel CDS improved			**E4** Active reset	
R 10 G 12 B 8		R 7 G 8 B 6			N/A	

Figure 4.68: Summary of the QE performance at 546 *nm* for eLeNA sensor.

4.3.4   eLeNA conclusions

eLeNA, a parametric sensor designed to evaluate noise reduction architectures, was characterised with optical methods using default acquisition parameters. The experimental results suggest that the sensor achieves low noise at the expected level. Test structures D1 and D2 (CDS 2 sample) achieve as low as $6 \ e^-$ temporal noise and exceptional FPN noise of $20-25 \ e^-$, but at the expense of poor quantum efficiency due to their low fill factor. However, this drawback can be overcome by sensor back-thinning. Test structure E (active reset) also demonstrated promising results in terms of low noise. Each of the characterised structures can find its application depending on the requirements, whether it is low noise, low FPN or higher QE. Extensive studies of the sensor will be continued as optimisation and tuning of the readout parameters can significantly improve overall performance of the system.

Chapter 5

Medipix applications

This chapter is devoted to the hybrid single photon counting detector Medipix. Section 5.1 briefly describes the chip architecture, peripheral electronics and read-out interface as well as the threshold equalisation procedure. A comprehensive description of the chip can be found in [67], detailed simulations of performance and characterisation in [68] and the description of the readout interface in [69]. Section 5.2 discusses the application of a set of such detectors in the ATLAS detector and the surrounding cavern. The motivation for the installation of the system is explained, the work of the author on the project is described and the preliminary results and conclusions on commissioning are drawn. Section 5.3 reports on the application of Medipix in the focal plane of a mass spectrometer. A brief introduction into the problem is given. Potential benefits of using the Medipix chip are discussed. Finally, the results of the characterisation of the chip are reported and the prototype system improvements are discussed.

5.1 Medipix chip

The Medipix project was undertaken by the microelectronics group at CERN with the aim of transferring the know-how gained in HEP pixel detectors to design a

general purpose pixellated X-ray imaging detector [68]. The resulting Medipix1 photon counting chip [70] was used in a wide range of applications [71, 72, 73]. The resolution of the system was limited by the pixel size of $170 \times 170 \ \mu m$, however the photon counting concept demonstrated excellent noise and dynamic range characteristics. This encouraged the development of a second generation chip, Medipix2, which reaped the benefits of both the experience gained in the design and application of the first generation chip, and the progress made in new fabrication technologies. The following main shortcomings of the Medipix1 were addressed:

- relatively large pixel size $170 \times 170 \ \mu m$ by going to $55 \times 55 \ \mu m$;

- a preamplifier sensitive to positive input charge only. New design allows both polarities at the preamplifier;

- leakage current compensation implemented on a column level only. This was extended to individual pixels;

The Medipix2 chip was designed in $0.25 \ \mu m$ CMOS technology. It contains a matrix array of 256×256 pixels at $55 \ \mu m$ pitch. Increased density of components not only decreased the pixel size but also allowed new functionality to be implemented. Improvements included:

- a charge sensitive preamplifier able to collect both electrons and holes, allowing alternative detection materials to be used;

- DC leakage current compensation implemented in each pixel leading to higher uniformity of the detector;

- three side buttable packaging allowing large area detection system to be built [74];

- high and low energy thresholds for energy window discrimination;

- high speed serial and parallel readout;
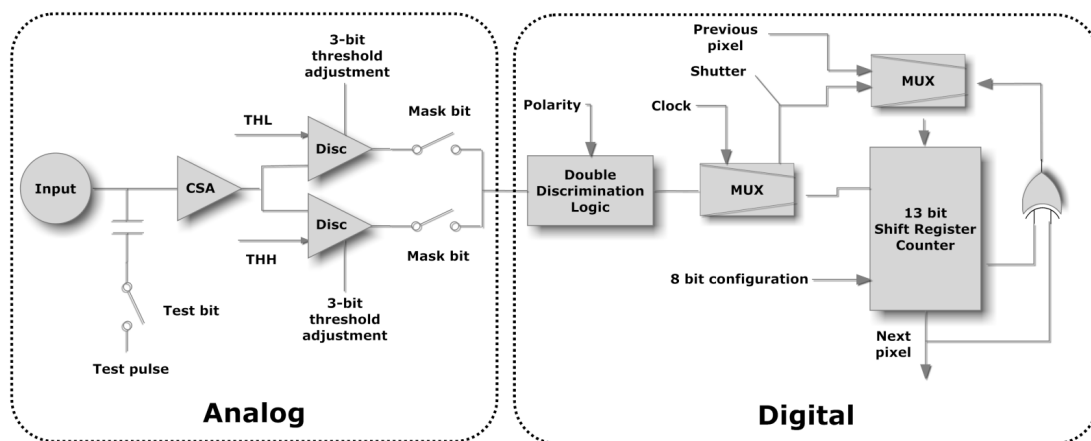
Figure 5.1: Medipix2 pixel schematics.

5.1.1   Pixel architecture

Each pixel in the matrix comprises analog and digital parts as shown in Fig. 5.1 with ~ 500 transistors. The analog part of the pixel consists of a charge sensitive amplifier (CSA) and two discriminators. The digital side has Double Discriminator Logic (DDL), a shift register and digital logic for counting and data shifting.

Each pixel operates in an acquisition mode, where the 13-bit shift register acts as a counter with a dynamic range of 8001 counts. The DDL functions as a clock for the counter in this case. In the shift mode an external clock is used to transfer the data from pixel to pixel through the shift register.

Analog part. X-ray photons interacting in the detection material deposit a charge. The charge drifts towards a collection electrode because of the external electric field applied to the detector. The CSA integrates and shapes the charge. Sophisticated feedback circuitry rejects substrate and power supply noises as well as compensating for the DC leakage current from the detector. Either positive or negative polarity of collection can be selected by choosing the appropriate DAC control signal. The output of the CSA is fed into two identical discriminators which form an energy window. The incoming pulse height is compared simultaneously with the low threshold level, THL, and high threshold level, THH. Excessively noise pixels can be discounted from the matrix by use of the mask

bit. Each pixel contains an injection capacitance connected to the CSA to allow it to be independently probed using a test voltage pulse.

Digital part. The two analog outputs from the discriminators are buffered at the input of DDL. The DDL logic uses the pulse from the discriminators to generate an output pulse of adjustable width. It can be operated in two modes: single threshold mode or energy window mode. The chip works in single threshold mode if THH level is set lower than THL; otherwise the energy window is formed. For each event a pulse of length corresponding to the incoming pulse height is generated at the output of DDL. In this approach the dead time between two events can be minimised by setting a relevant pulse length as well as keeping the relation between count and true event rate unambiguous. The output of the DDL is used to increment the counter in the Shift Register / Counter. The counter is 8001 counts deep. The device works as a pseudo-random counter when the Shutter strobe is low. Otherwise the counter content is shifted out serially to the next pixel until the end of the column is reached. The shift register is also used to set all configuration bits.

5.1.2 Peripheral circuitry

The periphery of the Medipix2 chip provides analog biasing, generates digital control signals to the pixel matrix and communicates with the readout system. It consists of the following:

- 13 8-bit DACs;

- A 256-bit Shift Register / Counter;

- I/O logic;

- Low Voltage Differential Signalling (LVDS) transceivers;

There is an End-of-Column logic that links the peripheral circuit with the pixel matrix via a buffer block. The 13 8-bit DACs set voltages and currents to bias the

analog and digital circuitry in the pixels. The data are sent into the configuration registers and the output of the counters on a row-by-row basis. It is organised in 256 columns of 256×13 bits, with a total of 851968 bits to be transmitted for any I/O operation. LVDS transceivers allow serial low power consumption single channel data transmission. An alternative 32-bit single-ended CMOS bus is also provided for high speed readout.

5.1.3 Readout interface

There are several Medipix2 readout interfaces available. The earlier readout system Muros2 [75] interfaces the Medipix2 chipboard with the commercial data acquisition system NI PCI-6533. Despite high readout speeds, the system has several disadvantages. External power supplies for the Muros2 interface and detector bias are needed. The application range of the Medipix2-Muros system is limited due to the large dimensions of external circuitry, limited cable length and lack of portability of the system.

A new USB interface has been recently developed [76]. The Medipix-USB readout system utilises a USB 1.1 interface to run the Medipix2 chip. The readout clock is limited to 20 MHz and the system can perform real-time acquisition at a maximum frame rate of ~ 5 Hz. The Medipix-USB system can be solely powered from a single 5 V 500 mA USB port allowing a high degree of portability. The detector bias voltage of up to 100 V can be internally generated, making the Medipix-USB system extremely portable. The work in this chapter was done using this system.

5.1.4 Threshold equalisation

Each pixel in the matrix responds in a slightly different way to incident radiation due to transistor fabrication mismatches and non-uniformities of the detector. In order to obtain better and more uniform response, the narrowest possible distribution of pixel threshold levels across the chip has to be found. The threshold
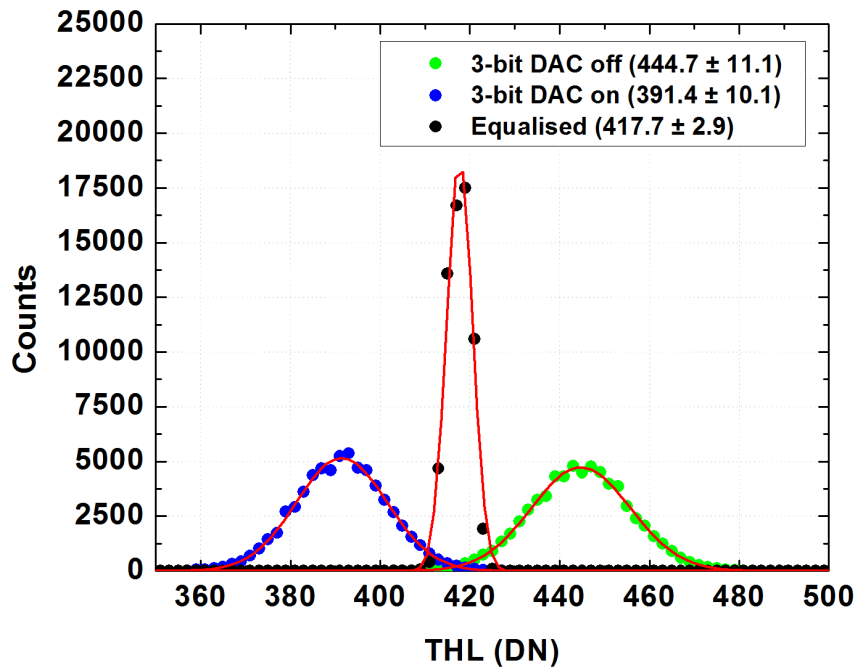
Figure 5.2: Medipix2 threshold equalisation using noise floor of the chip.

of the chip is set globally via dedicated peripheral DACs, controlled by THL and
THH for low and high thresholds respectively. However, the discriminator in each
pixel of the matrix has a 3-bit threshold adjustment DAC.

The fine-tuning of the low threshold of the chip can be done utilising three
possible sources of the input signal. A fixed height input can be obtained from a
monochromatic radioactive source. However, the activity of any portable source
is very low, which makes the equalisation procedure extremely time consuming.
A constant known input signal can be injected into the preamplifier through the
test capacitance (Fig. 5.1). Even though this makes equalisation faster and easier,
it is not possible to ensure equivalent charge is injected into every pixel due to
large variations in input capacitances. Alternatively, the noise floor of the analog
part of the pixel can be used as a reference signal. This provides a sourceless,
fast and reliable method to equalise the pixel matrix threshold. The noise floor
edge approach was used for all experiments described in this chapter.

The threshold is defined as the DAC value at which 50% of the applied pulsed signal is counted. A scan of the low threshold DAC (THL) is then performed across the input signal with 3-bit adjustment DAC opened (set to 000) and closed (set to 111) for all pixels in the matrix. This results in two distributions shown in Fig. 5.2 (left and right). The threshold adjustment DAC is now used to compensate the relative position of the Gaussian distribution for each pixel, which gives the value of the threshold closest to mean of the averaged distribution. This results in an equalised threshold for all pixels (see middle distribution in Fig. 5.2). The sigma of the final distribution is ≈ 3.5 times better than that of the non-equalised distributions.

5.1.5   Medipix2MXR

The Medipix2 chip demonstrates a very good performance as a photon counting hybrid pixel detector [67]. Small pixel size and very small input pixel capacitance make it a power efficient, portable high resolution radiation detector. However, several limitations of design were found and new ideas for improvements were generated during the characterisation period [67]. The voltage DACs showed a relatively high temperature dependence and a non-optimal linearity. The pixel counter was reinitialised every time it overflowed. The radiation hardness was at least one order of magnitude lower than expected from the fabrication technology [77].

These and other issues motivated a chip redesign, which resulted in Medipix2-MXR chip bringing enhanced functionality and a higher level of robustness. Radiation hardness was dramatically improved by using enclosed geometry transistors [39] for the sensitive nodes. An overflow bit was added and the capacity of the counter was increased to 11810 counts. The linearity of the DACs was improved by more careful design while their resolution was increased to 10-bits.

These and other improvements led to new applications, which were impossible with the original chip design. Two such applications are described in the following

sections.

5.2 ATLAS radiation monitoring system

5.2.1 Motivation

ATLAS is a large detector, recently installed underground at the Large Hadron Collider (LHC). Extensive simulations of the radiation environment in and around the experiment have been carried out in order to ensure safety of personnel as well as the safe operation of the detector [78]. However, the important task of verifying those estimations with *in situ* measurements had not been accomplished. The precise evaluation of the composition of the radiation environment inside and outside the detector is essential in order to understand the performance of the various detector systems and to predict their useful lifetime. It is important in particular to understand the background in the early stage of operation at low beam energies. Understanding this background is difficult because many measurement devices are not well suited to low doses and usually do not provide information on the precise composition of radiation [79]. The measurements at such background levels may help to give important feedback for data analysis and improvements on data taking strategy.

A number of devices are foreseen for this purpose [80]. However, these are often either passive or unable to easily provide real time information on the flux and flux distribution of different particles.

There are a number of general tasks that can be identified for the real time monitoring system. This includes radiation background monitoring with respect to X-rays, γ-rays, neutrons, protons and ions. The system should provide real time information about generated background radiation and validate simulation studies, as well as monitor the evolution of activation during beam-on periods and background studies during the beam-off periods. A number of specific measurements inside the detector cavern can be described as follows:
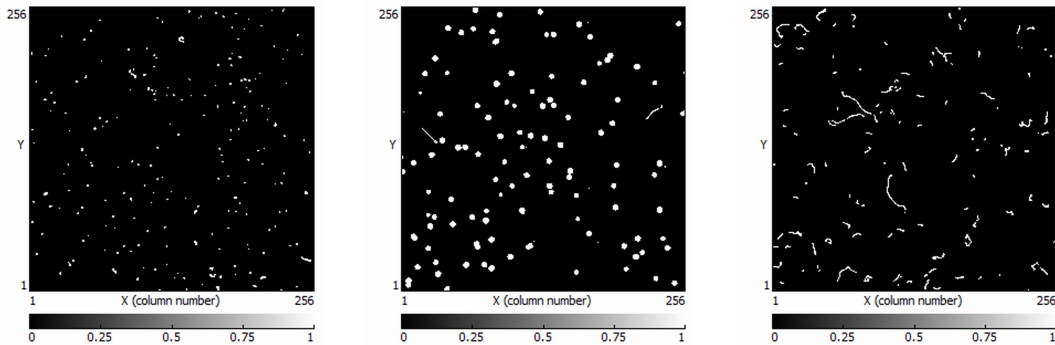
Figure 5.3: Examples of traces recorded with Medipix2MXR detector. Left to right: low energy X-rays, α-particles, electrons.

- personal and operational dosimetry in and around the ATLAS cavern;

- direct measurements of neutron fluxes and impact studies on detectors and accompanying electronics;

- study particle leakage from calorimeters.

The experimental data obtained at low and later high luminosity runs can also contribute to the preparation, planning and benchmarking of the LHC for the foreseen luminosity upgrade. It could give the necessary information about the radiation background in the detector and cavern, as well as indicating specifications for the shielding upgrade.

5.2.2 Data acquisition and evaluation strategy

Several operation modes were suggested to run the monitoring network.

Counting mode is appropriate for high detection rates when the number of interactions in individual pixels is determined at different threshold levels, giving information about radiation deposited in the detector.

Tracking mode is most suitable at low radiation rates or at very short acquisition times. Each kind of radiation leaves a unique track in the detector. This allows cluster analysis algorithms to be applied in order to quantify the number of interactions, as well as to determine the particle type if the tracks do

not excessively overlap. Fig. 5.3 shows typical Medipix2 responses to X-rays, α-particles and electrons. Low energy X-rays usually deposit all their energy in one or two pixels, while energetic γ-rays can form a cluster up to four pixels in size. α-particles deposit a large amount of energy in a confined space, resulting in big, up to 10 pixels in diameter, symmetrical blobs. Electrons leave long, erratically curved tracks. Protons usually leave comet-like traces in the detector because they lose their energy following the Bragg curve (see Section 2.1.1, page 7). In rare cases muons can be seen in the detector. They are identified as straight lines crossing the sensor from one side to another.

Low threshold operation. The devices operate at the highest sensitivity of $\approx 10~keV$ and accumulate maximum information from the surrounding radiation field.

High threshold operation. In the high threshold operation mode ($\approx 250~keV$) all tracks induced by light particles are excluded. This significantly decreases number of counts per pixel, while only particles that lose their energy following the Bragg curve are detected. Therefore the sensitivity of the device is limited to neutrons (slow and fast) and protons.

5.2.3   Energy calibration

X-rays calibrations of all devices were performed at the Institute of Experimental and Applied Physics of Czech Technical University in Prague [47] using the technique developed in [81]. Two sources were used: ^{55}Fe with 6 keV energy line of interest and two energy lines of ^{241}Am, 60 keV and 14 keV. Due to the very low emission rate of 14 keV X-rays in ^{241}Am, this energy was used to calibrate a few devices only and was mainly employed for cross-checking purposes. The detector was placed in a light tight box at room temperature and uniformly exposed to the radioactive source. The devices were set to operate in a single threshold mode. The preliminary threshold scan was accomplished in order to estimate the position of the energy peaks in ADC units. After such an estimation for one device,
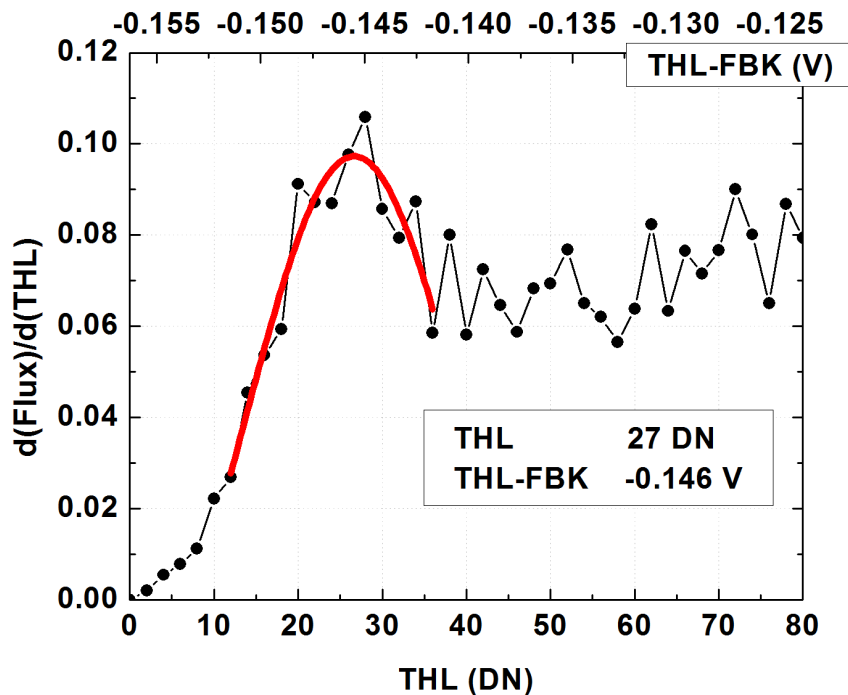
Figure 5.4: Example of energy calibration for a typical ATLAS-Medipix device with 60 keV X-rays.

the data for each of the 15 detectors were accumulated for 7-10 hours per peak. The start and end threshold was set to the levels where the peak was anticipated to increase statistics. An example of such a scan for ^{241}Am 60 keV is shown in Fig. 5.4. The 6 keV peak is very close to the noise level of the device, therefore for some detectors extra calibration point were needed. A typical calibration plot is presented in Fig. 5.5. In the region $6 - 60$ keV the Medipix2 detector has a linear dependence on the energy. The calibration curves remain consistent within $5 - 10\%$ for all 15 devices characterised.

5.2.4 Neutron detection efficiency

Neutron detection efficiency measurements were performed at the Czech Metrology Institute and Charles University in Prague [51]. Three types of neutron sources were used. Thermal neutrons were generated by a fission reaction in a
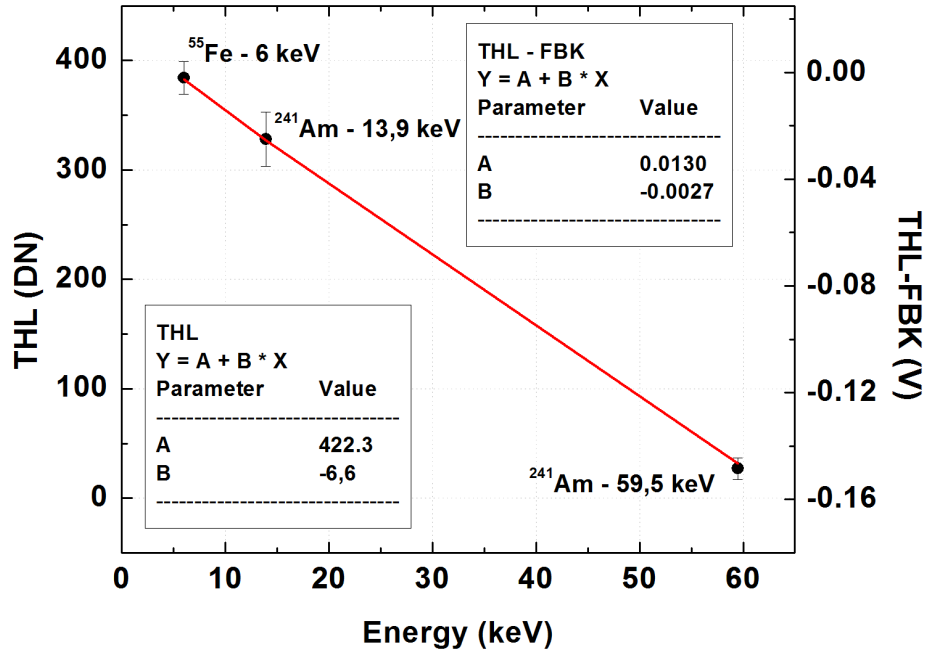
Figure 5.5: X-rays calibration curve for a typical ATLAS-Medipix device.

natural source and moderated by graphite to an average energy of $0.025\ eV$. All detectors, one by one, were placed in the middle of a cavity where the neutron flux per square centimetre was known. ^{252}Cf ($2\ MeV$ mean energy) and $^{241}AmBe$ ($4\ MeV$ mean energy) point-like sources were used to produce fast neutrons. The detectors were placed 10 - 50 cm from the source in order to achieve a balance between uniformity of illumination, reasonably low occupancy (for single track identification) and high enough statistics. 14 MeV neutrons were produced in a Van der Graaff accelerator.

Four dominant reactions were considered for neutron detection. Thermal neutrons interact with ^6Li by nucleus capture with the emission of heavy charged particles:

$$^6Li\ +\ ^1n\ \rightarrow\ ^4\alpha\ +\ ^3H \tag{5.1}$$

Fast neutrons interact dominantly by elastic scattering from nuclei producing a
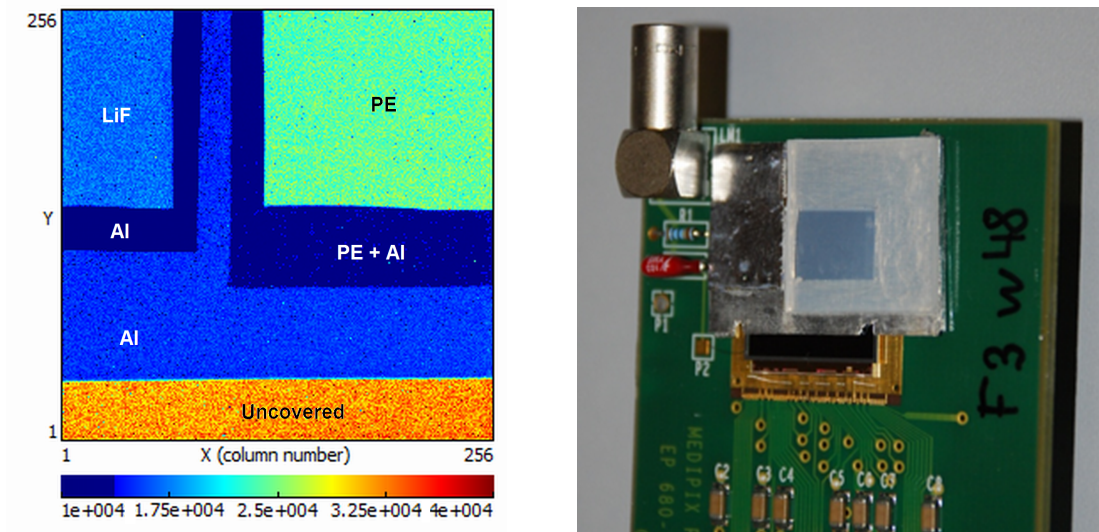
Figure 5.6: X-rays image and photograph of Medipix2MXR detector with neutron converters.

recoil proton:

$$^2H \ + \ ^1n \ \rightarrow \ ^1p \ + \ ^2H \tag{5.2}$$

Fast neutrons also can react directly with silicon atoms causing activation:

$$^{28}Si \ + \ ^1n \ \ \rightarrow \ \ ^4\alpha \ + \ ^{25}Mg \tag{5.3}$$

$$^{28}Si \ + \ ^1n \ \ \rightarrow \ \ ^1p \ + \ ^{28}Al \tag{5.4}$$

The Medipix2 devices were covered with several types of converters. Fig. 5.6 shows both an X-rays image of the device as well as a photograph. An aluminium frame was used to support the detection materials above the detector. The following areas can be identified:

1. a ^6Li based thermal neutron converter in the form of fine ^6LiF powder (enrichment 89%, density $\sim 5 \ mg/cm^2$) mixed with polyvinyl alcohol as a binder (less than 5% of weight) enables the detection of thermal neutrons, using the reaction in Eq. 5.1;

2. a polyethylene plate (1.3 mm thickness) enables the detection of fast neutrons via the reaction in Eq. 5.2;

3. PE + Al (1.3 mm thick polyethylene layer on top of $\sim$ 100 μm thick aluminium support);

4. Al ($\sim$ 100 μm thickness) energetic electrons and X-rays attenuate in this layer;

5. thick Al (100 μm + 50 μm thickness) the same as 4;

6. an uncovered area enables detection of low energy electrons, X-rays and γ-rays. Neutrons can also react here by direct nuclear reactions in Eq. 5.4.

The high threshold operation mode was chosen in order to exclude tracks induced by light particles. The acquisition time was set short enough to ensure tracks were not overlapping. Separated tracks were then counted and the efficiencies calculated as follows for each of the regions:

$$\epsilon_{n-Si} = \frac{\frac{N_n}{S_n} - \frac{N_{Si}}{S_{Si}}}{\Phi t} \qquad (5.5)$$

where N_n and N_{Si} are the number of tracks in the n-th and uncovered regions, S_n and S_{Si} are the respective areas, Φ is the neutron flux incident on the sum of the corresponding two areas and t is the integration time.

Neutron detection efficiency significantly depends on the geometry and shape of the conversion material as well as the quality of the converter or uniformity of the solution deposited (for ^6LiF). Therefore the calibrations were performed for all devices to be installed in the ATLAS detector. The results are summarised in Table 5.1. The error in % reports on the standard tolerance for all calibrated devices.

Angular detection efficiency

One ATLAS-Medipix device was exposed to two fast neutron sources at different angles ranging from 0° (sensing area is at right angle to the beam) to 180° (the detector is irradiated from the back side). The results are presented in Fig. 5.7 in

	Thermal	^{252}Cf	$^{241}AmBe$	*VDG*
^6LiF	1.0e-2 ± 25%	9.9e-5 ± 75%	2.4e-5 ± 77%	1.2e-3 ± 17%
Al	3.8e-6 ± 80%	7.1e-5 ± 100%	2.3e-4 ± 38%	1.0e-3 ± 18%
ThickAl	2.8e-4 ± 60%	6.9e-5 ± 100%	2.2e-4 ± 39%	1.0e-3 ± 17%
PE	2.5e-6 ± 50%	4.0e-4 ± 35%	9.8e-4 ± 20%	2.8e-3 ± 15%
PE + Al	2.6e-6 ± 70%	1.0e-4 ± 65%	4.2e-4 ± 30%	2.4e-3 ± 16%
Uncovered	3.1e-6 ± 85%	8.5e-5 ± 100%	2.3e-4 ± 40%	9.8e-4 ± 20%

Table 5.1: Summary of the neutron detection efficiencies and tolerance for all ATLAS-Medipix devices characterised.

the form of a polar graph. The detection efficiency in the polyethylene region was compared to the one in the uncovered region. The efficiency drops significantly beyond $\sim 90°$ and only interactions in silicon take place. Neutrons from ^{252}Cf are detected most efficiently at acute angles, while faster neutrons from $AmBe$ have a higher probability to interact if the travel distance in PE is longer, which suggests that a slight increase in PE thickness should increase the detection efficiency by $\sim 10\%$.

5.2.5 Connection structure of the network

Each of the 15 installed devices is connected to one of three control computers, depending on the physical location in the ATLAS detector. The data is accumulated locally and copied over to the data storage computer in the ATLAS computer hall. The user can have online access to the system and the visual data via a dedicated online web interface.

5.2.6 Medipix-ATLAS background radiation monitoring system conclusions.

The network of 15 Medipix2 devices was installed in the ATLAS detector and surrounding cavern. Four detectors are placed between the moderator shielding and the Liquid Argon (LAr) calorimeter. Two devices are installed on the TileCal, one on each side. Four devices are located near the muon chambers and two close
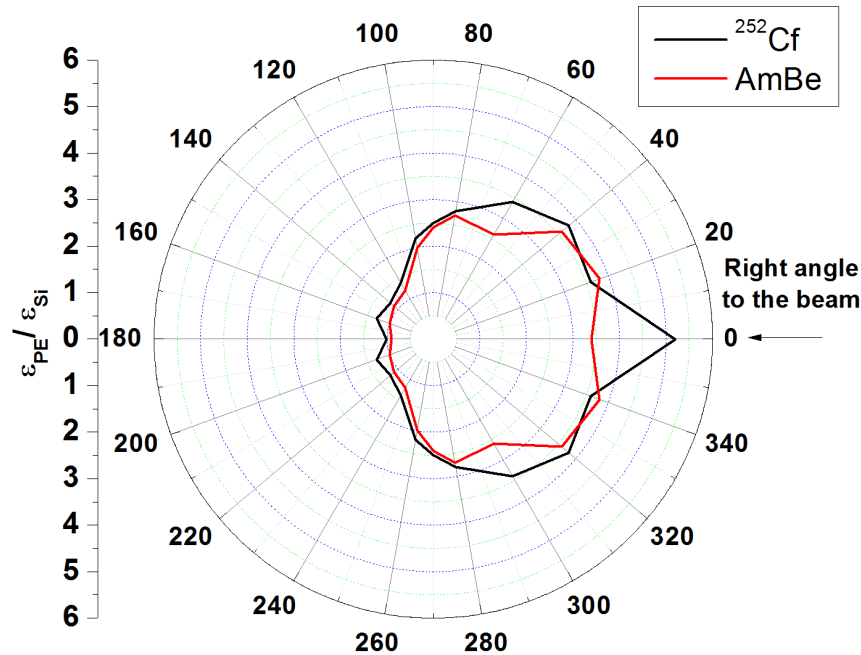
Figure 5.7: Angular neutron detection efficiences of the Medipix2 detector.

to very forward shielding. The last two detectors are placed on the cavern wall and on a staircase [81]. The system is capable of performing real-time dose and flux measurements of X-rays, γ-rays, fast and thermal neutrons, electrons and heavy charged particles. During the early stages of LHC commissioning the network will be used for:

- analysis of the neutron contribution to the background signal in the forward Inner Detector, forward regions of the LAr calorimeters, Tile calorimeter and Muon Chambers;

- monitoring of γ-rays, neutrons, electrons and heavy charged particles and the radiation field determination around the moderator shielding region as well as estimation of its effectiveness;

- study of leakage from the calorimeters, including monitoring of the her-
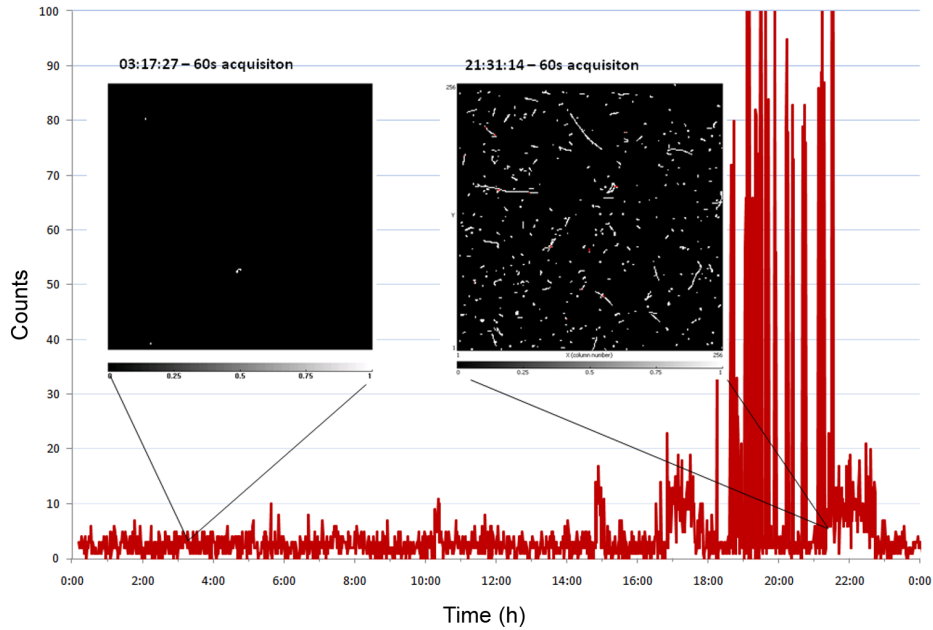
Figure 5.8: ATLAS-Medipix monitoring network activity recorded the day before and day of the LHC start up.

meticity of the LAr calorimeters, estimation of the hadron leakage into the muon detector system and evaluation of the muon detection efficiency due to residues of hadronic showers.

The system was proven to work very well during the first LHC test run on the 10th of September 2008. Fig. 5.8 demonstrates the difference in the total number of registered and recognised events the day before and on the day of the start up. The data were recorded with the device located in the forward part of the ATLAS detector, $\sim 5\ m$ from the beam line.

One issue has been identified and is now fixed. The PCs running the network, which are located in the ATLAS detector, sometimes suffered sudden reboot. This was found to be due to the superconducting magnets being switched on and off. It is believed that improving the magnetic shielding of the PCs will fix this problem.

5.3 Medipix in the focal plane of a mass spectrometer

Mass Spectrometry (MS) is a powerful technique for the analysis of the elemental composition of a sample. It is an important tool in many fields of science and industry, which is employed to analyse biomolecules and single cells [82] as well as to explore samples from other planets [83]. Environmental and forensic analytics, quality control of drugs and polymers: these are some examples of activities that heavily rely on MS.

The basic principle of MS is to generate ions from a compound material (either organic or inorganic) by any suitable method, to separate these ions by their mass-to-charge ratio and to analyse them qualitatively and quantitatively. All mass spectrometers consist of three main parts: an ionisation block, analyser or separation block and detector. Once a sample is introduced into the mass spectrometer, molecules of the sample are ionised. These ions are then extracted by an electric field into the analyser region where they are separated according to their mass-to-charge rations. The separated ions are detected and the data are presented in the form of mass-to-charge ratio versus number of counts reporting on the relative abundance of the components.

Ion generation and separation blocks received significant attention from research communities. The most common source of ions is the electron impact ionisation source, but many other sources have been developed for particular applications. At the same time a range of analysers have been developed, including time-of-flight, electrodynamic, magnetic and combined devices [84].

5.3.1 Motivation

The advances in detection technologies, in contrast, were occurring very slowly, borrowing detector systems from other technologies as they became available. Only a few truly new detection approaches have been devised. The first array

detector used in MS was the photographic plate. However, the photographic emulsion has many weaknesses. It has limited sensitivity, very low linear dynamic range and numerical analysis of the data is time consuming, inefficient and costly. The first electronic alternative to the photographic plate was the electro-optical ion detector (EOID) [85]. This contained a multichannel plate (MCP), a phosphor screen, a tapered fibre optic imaging bundle and a video camera tube system[1]. Ions were converted to electrons, which in turn were converted to photons and then detected by the camera and again converted into electrons to produce a spectrum. Such a system was an inefficient combination with poor performance characteristics but allowed digital storage of data.

The explosion of CCDs in detector applications led them to become the most common detector found in MS systems. Over the last decade CMOS MAPSs also attracted attention as an alternative to CCDs because of a number of advantages such as low cost, monolithic integration, low power consumption, *etc.* [86].

Despite the progress in the development of detectors over the past century, they still suffer from several shortcomings experienced with photographic plate and later CCDs and MAPSs. The dynamic range in modern detection systems can hardly exceed four orders of magnitude in the linear range [83]. Noise performance improvement is also required for low mass, low energy analysis applications. Biological MS demands an ability to uniformly detect ions over very high mass-over-charge ranges. Truly simultaneous high resolution detection remains crucial for analytical chemistry [84].

Medipix2, with its single photon counting approach, promises to overcome some of the above mentioned drawbacks. Setting an appropriate threshold level makes acquisition free of background noise. The minimum signal that can be detected by Medipix2MXR is $\sim 5~keV$, allowing noiseless measurements to be carried out for ion energies exceeding this level. Medipix2MXR has a fast recovery time of $\sim 1~\mu s$, which leads to a MHz readout rate per pixel. The system has

---

[1]The video camera tube or vidicon was used in video cameras before the first CCDs were invented. It is a type of vacuum tube containing an electron gun and a fluorescence screen.
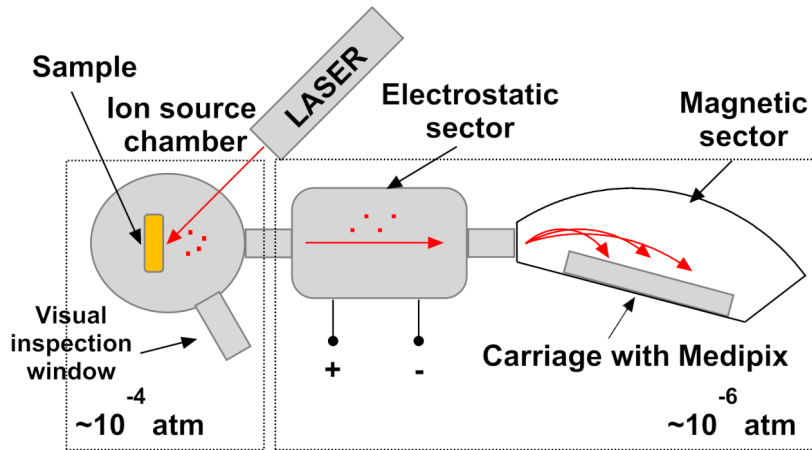
Figure 5.9: Schematics of the prototype laser mass-spectrometer MC3103.

high dynamic range and is able to count up to 11810 hits per acquisition.

5.3.2 Mass spectrometer description

The measurements were performed at Institute of Applied Physics, Sumy, Ukraine. A principal schematic of the prototype mass spectrometer MC3103 is shown in Fig. 5.9. The ion source chamber holds a sample. The laser source generates $2 \ ns$ pulses at $50 \ Hz$ repetition rate, which strike the sample through a small window in the chamber. This process can be visually inspected using an optical system on the other side of the chamber. The laser pulse knocks out positively charged ions from the sample, which reach the electrostatic sector through the object slit. The ions are accelerated in this block to the energy determined by the applied electric field. Accelerated ions from the electrostatic sector enter the magnetic sector where the ions of different masses are deflected along circular paths of different radii. Medipix2MXR was placed in the focal plane of the mass spectrometer. The radius of the incoming ion beam can be altered by adjusting the current in the magnet. The detector was mounted on the carriage. The move-

ment of the carriage is externally controlled by a system based on the AT89S8252 microcontroller and a stepping motor with a 7 μm step size. The detector can be moved along the focal plane of the mass spectrometer as well as tilted around the long axis of the detector.

Active volumes of the mass spectrometer were held in vacuum. Free ions are very reactive and short lived. They can interact with every molecule on their way, which significantly changes their energy and direction. There are two vacuum blocks in the mass spectrometer. The analyser (electrostatic and magnetic sectors) was kept at a high vacuum of $10^{-5} - 10^{-6}$ atm, while the source chamber vacuum was 10^{-4} atm. This approach allows time efficient sample change in the mass spectrometer: the analyser vacuum can reach the desired level in $8 - 12$ h, in contrast the sample chamber vacuum is achieved in $2 - 3$ h only.

5.3.3 Experimental results

Ion beam tuning

A two dimensional online acquisition system has never been implemented in this type of mass spectrometer before. The first test runs using Medipix2MXR showed focusing problems of the ion beam incident on the detector. Fig. 5.10 shows the results obtained from the Cu sample with two isotope lines, ^{63}Cu and ^{65}Cu. Two anomalies can be seen in the left figure. The focussing magnets should be set to focus the ion beam into a one dimensional planar beam with a Gaussian spread in the lateral direction. It is this lateral spread which influences the spatial resolution of the system. Using the Medipix detector, the beam was imaged in two dimensions showing the deviation of the beam from the planar. This deviation decreases the accuracy of measurements. The intensity along the beam line is also shown to be highly asymmetrical. This is caused again by errors in the focussing magnet arrangement, which makes the beam bounce from the top of the magnet cavity resulting in an intense blob and stripe separated by a gap. The

(a) Before   (b) After
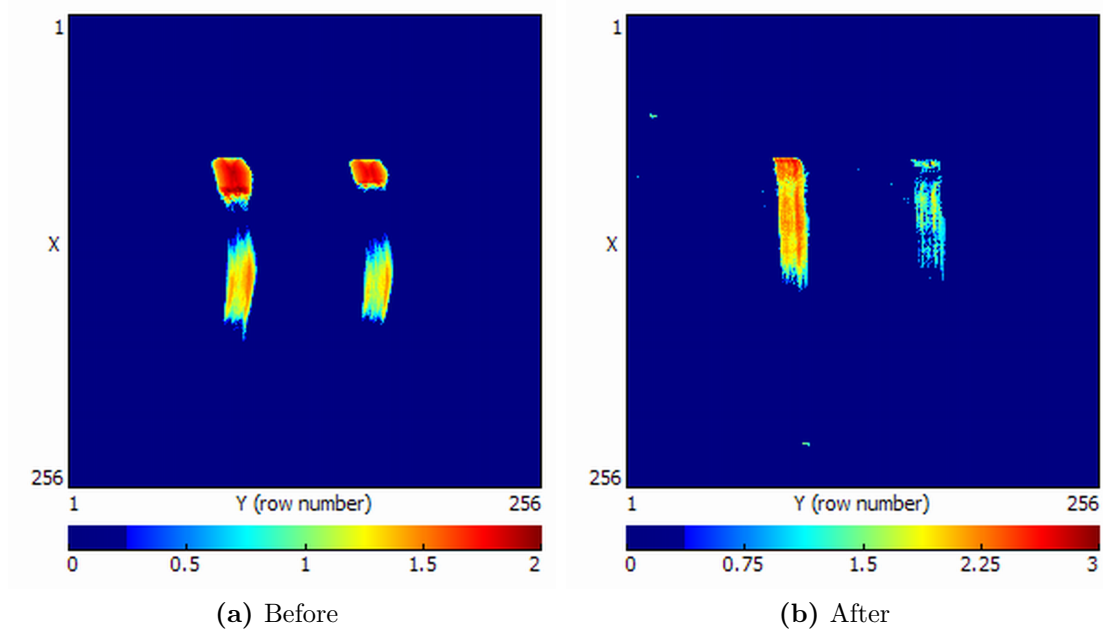
Figure 5.10: Online tuning of the ion beam using two dimensional representation.

online nature of data acquisition allowed careful magnet tuning in all directions, resulting in better two dimensional beam representation (Fig. 5.10).

Energy

The measurement of the response of the Medipix2MXR detector with respect to ion energy was carried out using a standard Cu sample. The laser power density was tuned to produce Cu^{2+} ions, which was anticipated to give a relatively high signal at low energies. The ion energy was varied by changing the electric field in the electrostatic sector of the mass spectrometer. The threshold of the detector was set just above the noise level. The results were plotted as a total number of counts recorded by the pixel matrix versus ion energy. Fig. 5.11 shows that Medipix2MXR is capable of detecting ions of as low as $5\ keV$ energy. However, it was noticed that when the detector is in operation for a long period of time (more than $\sim 1\ h$), the minimum detectable energy increases ($\sim 6 - 8\ keV$) due to a
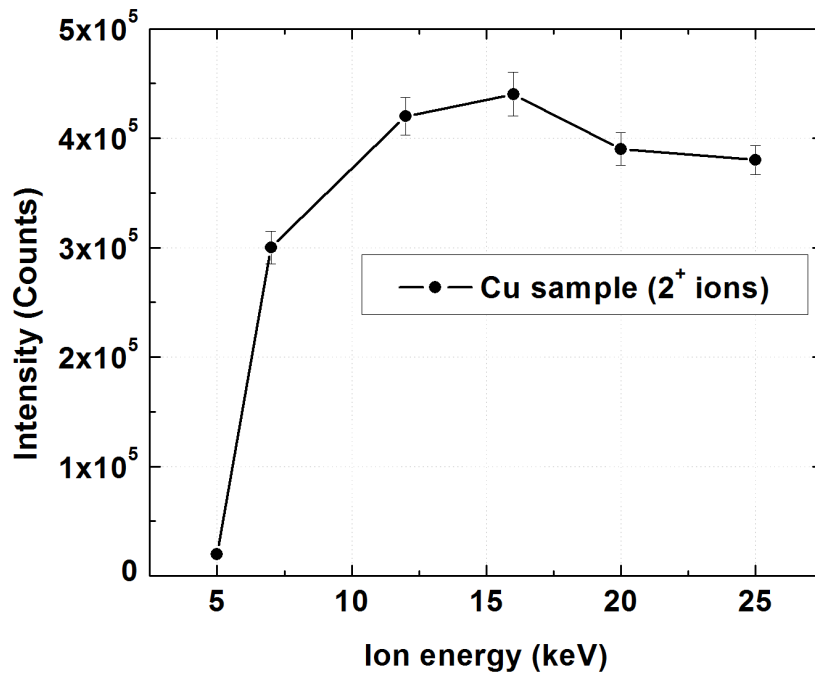
Figure 5.11: Relative detection efficiency of the Medipix2MXR detector to the different ion energies.

higher noise level. This is because, when in a vacuum, power dissipation from the detector is limited, which steepens the temperature gradient of the readout chip. The number of counts recorded starting from $\sim 12 \; keV$ becomes independent of the ion energy.

Isotopes

The Medipix2MXR detector in the focal plane of the mass spectrometer was tested using a compound sample with known element abundances (Table 5.2). Fig. 5.12 shows an example of a mass spectrum of the double charged isotopes of lead. This element has four stable isotopes, $^{204}Pb - 1.4\%$, $^{206}Pb - 24.1\%$, $^{207}Pb - 22.1\%$, $^{208}Pb - 52.4\%$, which can be clearly distinguished. The relative abundances of the isotopes, represented by a relative number of counts, matches the table data well. The system can detect as low as 1% of the relative isotope
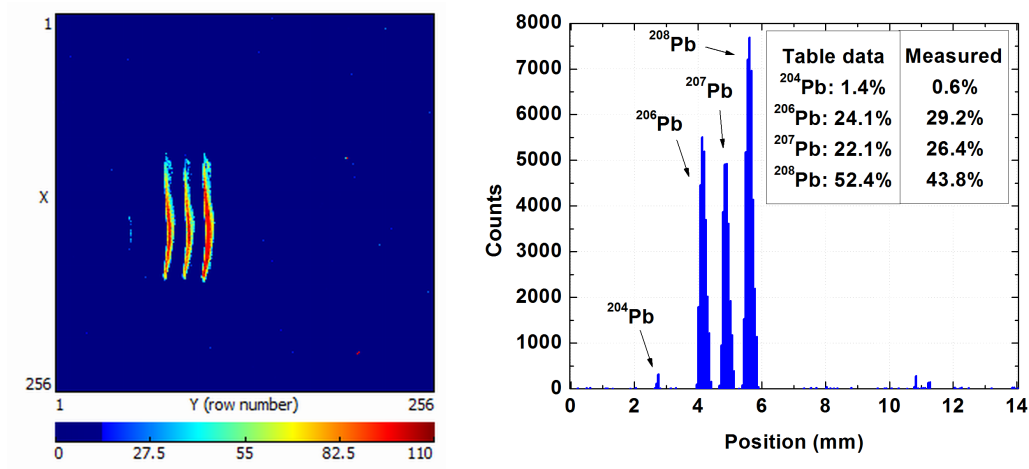
Figure 5.12: Example of the mass spectrum of the double charged isotopes of lead of 12.1 keV energy.

Element	Abundance (%)
Cu (Fe)	87.53
Zinc (Zn)	4.93
Lead (Pb)	4.40
Tin (Sn)	3.05
Iron (Fe)	0.02
Antimony (Sb)	0.003

Table 5.2: Relative abundance of the elements in the sample S662.

abundance. However, the ^{208}Pb peak was expected be twice as high as the ^{207}Pb and ^{206}Pb peaks. This suggests that the relative sensitivity of the detector varies spatially.

Fig. 5.13 shows another interval of the sample mass spectrum, which include double charged ions of tin, single charged ions of copper and zinc. Tin has the following stable isotopes: $^{112}Sn - 0.97\%$, $^{114}Sn - 0.66\%$, $^{115}Sn - 0.34\%$, $^{116}Sn - 14.54\%$, $^{117}Sn - 7.68\%$, $^{118}Sn - 24.22\%$, $^{119}Sn - 8.59\%$, $^{120}Sn - 32.58\%$, $^{122}Sn - 4.63\%$ and $^{124}Sn - 5.79\%$. ^{115}Sn cannot be seen due to very small abundance and hence low intensity. The relative quantity of all isotopes agrees well (within 10%) with the expected values. Also very good spatial resolution is demonstrated. An estimate shows that $\sim 10^4$ single-charged ions are required to
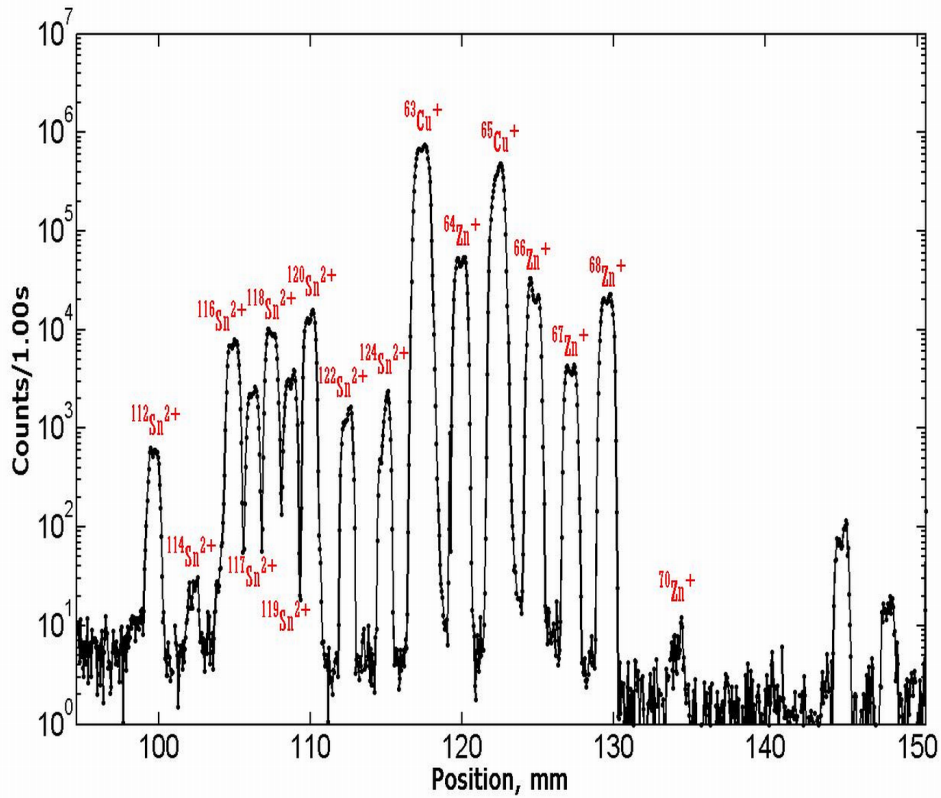
Figure 5.13: Example of the mass spectrum of the composition of elements from the sample S662.

be incident on the detector to trigger one pixel count.

The mass spectrometer was tuned to produce ions with several charges. Fig. 5.14 shows mass spectra from a Zr sample. The natural abundance of the isotopes in the sample is as follows: $^{90}Zr - 51.45\%$, $^{91}Zr - 11.22\%$, $^{92}Zr - 17.15\%$, $^{94}Zr - 17.15\%$, $^{96}Zr - 2.80\%$. ^{93}Zr decays into the stable isotope ^{93}Nb, which can be also seen in the figure. The measured abundances agree within 10% if compared to the table data for ions of 2^+, 3^+ and 4^+ charge. Single charged ion detection efficiency is much lower, while the deviation from the table data is higher (Fig. 5.14a).

(a) Zr^{1+}

(b) Zr^{2+}

(c) Zr^{3+}

(d) Zr^{4+}
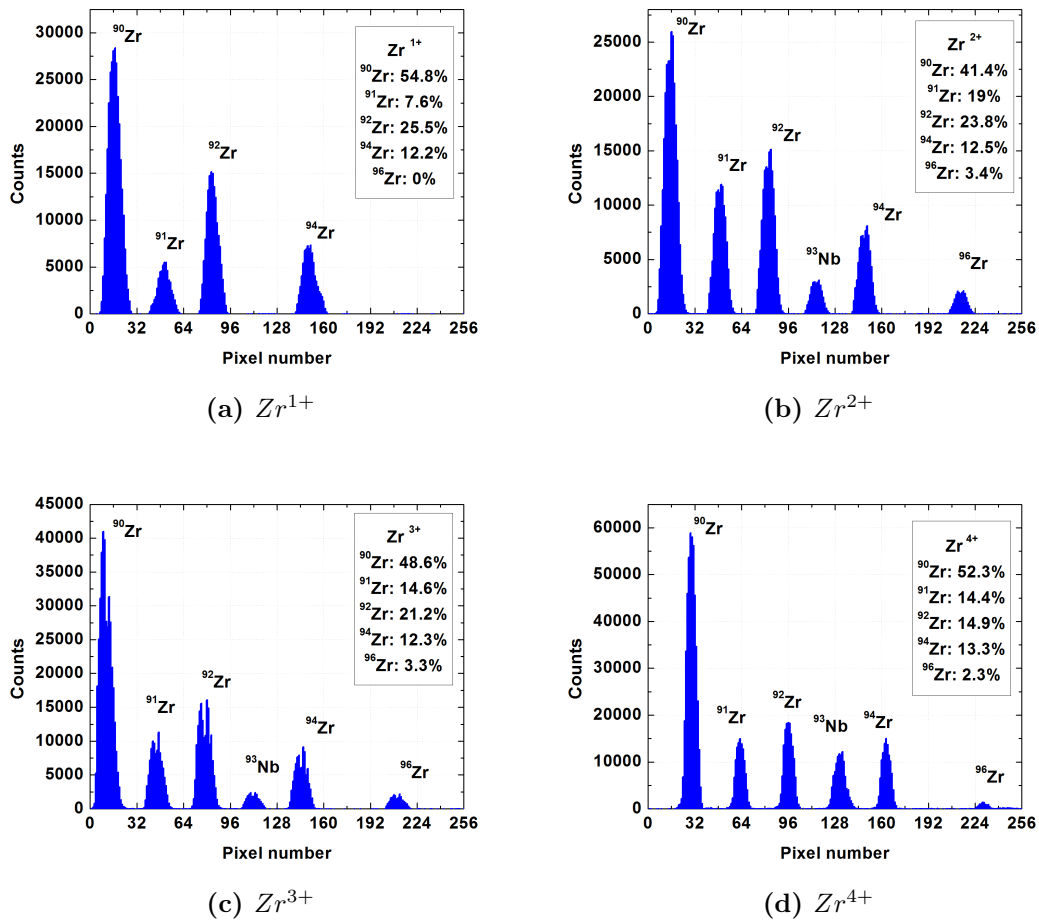
Figure 5.14: Count rate comparison of the mass spectrum of differently charged zirconium isotopes.

Spatial non-uniformity

The spatial uniformity response of the Medipix2MXR detector was tested with a Cu sample. The ion beam position was fixed. The sensor was moved in the focal plane in such a way as to project the Cu isotope lines onto the nine segments of the sensing area: left, middle, right, top, centre and bottom. Figure 5.15 shows the 2D representation and 1D projection of the scan through the centre of the detector. Table 5.3 summarises the relative abundance of the ^{63}Cu and ^{65}Cu isotopes and compares the results to the table data. Each area of the
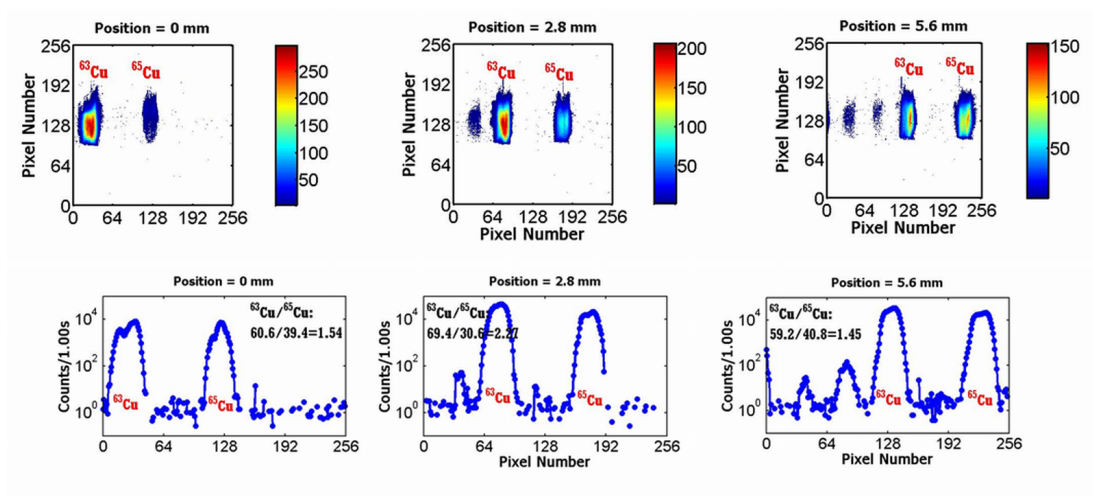
Figure 5.15: Example of the Cu sample scan of the Medipix2MXR detector over several segments for spatial non-uniformity estimation.

	Left	Centre	Right	True value
Top	2.24	1.99	1.49	
Middle	1.54	2.27	1.45	2.24
Botton	3.60	2.24	1.20	

Table 5.3: Relative abundance of the ^{63}Cu and ^{65}Cu isotope response of the nine segments in the Medipix2MXR detector.

Medipix2MXR detector produced a slightly different response. The highest non-uniformity was observed at the bottom corners of the detector. However, for the routine mass spectra measurements the detector can be corrected for non-uniformity by careful calibration.

Bare chip measurements

The Medipix2MXR chip with a silicon detector bump-bonded to it was shown to work very well in the focal plane of the mass spectrometer. However, such a detection system suffers from spatial non-uniformity. Tests on a bare Medipix2MXR chip were also carried out. This configuration has several advantages. An intense ion beam can cause permanent damage to the detector in the form of a deposited layer of sample material or induce ion implantation beneath the surface of the de-

(a) Zr^{2+}

(b) Zr^{3+}
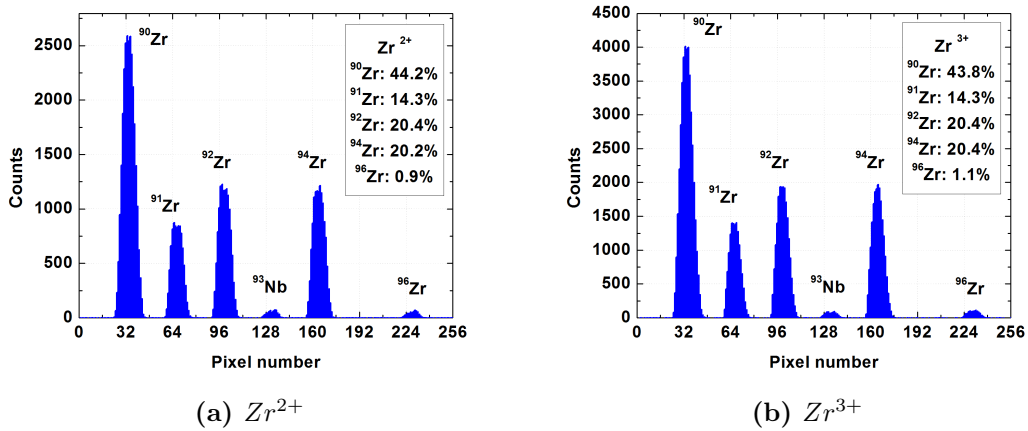
Figure 5.16: Example of the mass spectra of zirconium isotopes recorded with bare Medipix2MXR chip.

tector. The bare chip has higher radiation tolerance as well as lower risk of static charge accumulation, reducing the risk of possible shorts in the circuit. Metal octagonal electrodes for bump bonding the detector were used as the collecting anodes.

Fig. 5.16 shows the spectrum of a Zirconium sample with double and triple charged ions. The results obtained agree well with the natural isotope abundance table. However, the detection efficiency of the bare chip is one order of magnitude lower in comparison to the chip with a detector. The area of the pixel is $\approx$ 3000 μm^2, while the area of the metal contact is $\approx$ 100 μm^2. This means that only a fraction of the pixel area is sensitive to an incident ion, reducing the sensitivity of the bare chip.

5.3.4 Medipix in the focal plane of a mass spectrometer conclusions

The Medipix2MXR detector as well as the bare chip were tested in the focal plane of a mass spectrometer. The system provides a two dimensional image of an ion beam and surveys as an "electronic plate". This was proven to be extremely
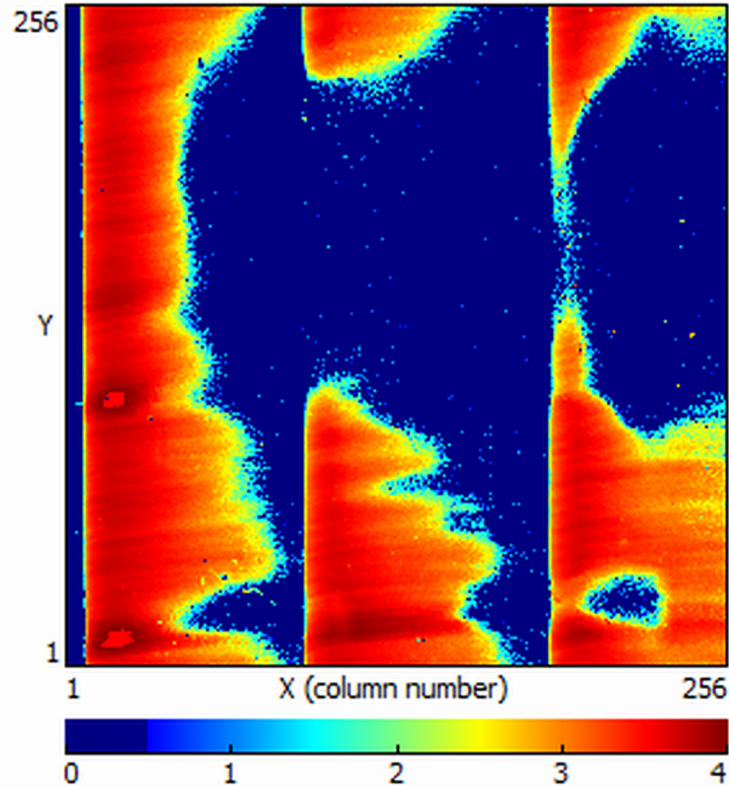
Figure 5.17: Response of the Medipix2MXR detector to the Cu sample damaged with intensive ion beam [87].

useful for tuning of the mass spectrometer. The detector can be used as an on-line diagnostic tool for various purposes, including beam focusing, alignment, magnetic and electric field stability and uniformity monitoring. The system was shown to be able to detect low energy ions in the range of $5 - 25 \ keV$. A broad range of isotope masses from Cu to Pb were used to characterise the detector. The results obtained showed very good agreement of the measured abundances of the elements with the table data. The system adequately responds to single, double, triple and quadruple ions with a reasonable efficiency of $\sim 10^4$ ions per count. The response uniformity of the detection area remains an issue. However, this can be fixed off-line by applying a calibration correction technique.

The bare sensor showed ~ 10 times lower sensitivity to ions in comparison to the chip with detector, which is mainly due to a smaller sensitive area. This

issue can be addressed by replacing the silicon sensor with a pixellated metal plate. This should improve the sensitivity of the chip to incident ions. The uniformity of the response will be dramatically improved. At the same time the detector lifetime will be increased. Fig. 5.17 shows an example of the detector response to an incident Cu ion beam after a long exposure to He and H_2 ions at an isochronous cyclotron. The figure presents a sum of the results of consecutive scan of the Cu sample beam across the detector. A blue area demonstrates zero count rate. The affected pixels became insensitive to low energy ions, remaining active to X-rays. This suggests that ion implantation took place, making the surface of the detector insensitive.

Chapter 6

Summary and conclusions

The research and development of two classes of CMOS pixellated radiation detector technologies is presented in this thesis. The first class is the science grade Monolithic Active Pixel Sensors. Thanks to recent advances in standard VLSI CMOS technology, MAPSs are now seriously considered as an alternative to CCDs in many applications. One of the main advantages of MAPSs is a dramatic reduction in fabrication costs as they do not require specialised foundry facilities. The technology also allows custom designs tailored to suit specific applications. Being fabricated in a standard CMOS process, the sensors can be integrated on a single chip with data post-processing electronics and storage, bringing a new level of portability and reduced power consumption.

The first sensor characterised - HEPAPS4 - was developed for charged particle detection applications. The technology is envisaged for potential large scale application in the vertex detector of the International Linear Collider or similar experiments. The sensor firmware and prototype acquisition system were built and showed a high level of reliability. The ideas used to create firmware can be adapted to other acquisition systems and sensors. Three versions of the sensor featuring several design concepts were fully characterised using photonic techniques. The "D1" version of the sensor, with enclosed geometry transistors, was

found to have a gain of $5.5 \pm 0.5 \, e^-/DN$. The noise level of $35 \pm 5 \, e^-$ agrees well with simulated data. Off-chip CDS implemented in the firmware showed that the noise is dominated by the system noise of the readout board. This should be taken into consideration when developing a new generation of sensors. It is suggested to design a "dummy" sensor at the development stage in order to quantify noise from each component in the acquisition chain. The dark current density of 175 pA/cm^2 remains relatively high in comparison to modern CCDs, making the technology not yet competitive in applications where long integration times are required. It was proven that careful tuning of the acquisition parameters can significantly improve the overall performance of the system. Essential research still to be carried out on the sensor includes a calculation of the minimum ionising particles detection efficiency and a study of the sensor resolution. The latter is of vital importance for tracking applications in particle physics. The radiation hardness of the "D1" version with enclosed geometry transistors should be quantified and compared to standard pixel designs.

The HEPAPS4 sensor was adapted to make neutron detection possible. The measurements performed showed that the technology is well suited for thermal and fast neutron detection, with efficiencies ($\sim 0.01\%$ for fast neutrons) comparable to other similar technologies [88]. The spectra from these events were structurally complex and would benefit from thorough Monte-Carlo simulations to understand more clearly all the mechanisms that contribute to this complexity. It is also essential to understand the response of the sensor to protons with energies comparable to those from neutron reactions as well as the response to α-particles and tritium nuclei with corresponding energies. Dramatic improvements in the performance of the MAPSs as a thermal neutron detectors are anticipated for back-thinned devices, which lack the many layers of electronics, oxide and passivation. The future work on this subject should not only include intensive simulation studies, but investigation of new possible designs and alternative conversion materials. The research carried out in this thesis proved the concept

of combining CMOS MAPS and a converter for possible applications in neutron imaging applications. This is anticipated to be carried forward as only a few publications are available to date which propose CMOS MAPS as a neutron imaging detector.

The second device characterised is known as the Vanilla sensor, which was designed to evaluate several new techniques. It features both analogue and digital readout. In digital mode the sensor utilises on-chip ADCs, which dramatically speed up the readout (up to 150 full frames per second). In analogue mode there is an option to read out part of the frame - region of interest readout. All pixels in the senor can be reset in three modes: hard, soft and flushed. This allows a direct comparison of reset types. The flushed reset was shown to have the lowest noise of $14 \pm 4 \ e^-$ while keeping the image lag low. The sensor has dark current density of $50 \ pA/cm^2$ which is three times lower than in the previous generation of sensors, HEPAPS4.

The back-thinned (BT) version of the sensor was characterised and the comparison was made to the standard version of the sensor. The back-thinning process did not dramatically degrade the performance of the sensor. The noise remained the same while the dark current was increased by a factor of two only. This is attributed to the surface damage caused by grinding, etching and polishing. The quantum efficiency of the BT sensor dramatically improved in the UV region, from 0% to 20% at 220 nm. Future avenues of research include the areas where the potential of the back-thinned sensor can be fully exploited. For example, increased α-particle detection efficiency should be quantified and compared to the non back-thinned sensor, which will give grounds to develop for example improved atmospheric radon monitoring systems [89]. Fast ROI readout capability combined with increased UV sensitivity can find applications in bio-science, such as optical tweezers and autoradiography [90].

eLeNA is the most recent parametric sensor designed to evaluate noise reduction architectures. The most promising test structures have as low as 6 e^-

temporal noise and 20 e^- fixed pattern noise. The price is low QE ($< 4\%$) due to the small fill factor. However, this can be overcome by back-thinning. The test structures can find many applications, depending on the requirements. For example, MIPs detection applications can benefit from the 12 μm epi-layer thickness, giving an anticipated SNR performance of 160. The full potential of the sensor is still to be fully explored. Careful tuning of the readout parameters can help drive the noise of the sensor even lower. Currently available CCDs show noise values of < 1 e^-, and it seems that CMOS MAPS technology is not far behind.

The second class of pixellated radiation detectors explored is the hybrid pixel detector Medipix, working in the single photon counting mode. The Medipix readout chip was designed for X-ray detection working in counting mode. This approach has several advantages such as "noiseless" readout and a large dynamic range. The detector has found a variety of applications in X-rays imaging, computer tomography and electron microscopy amongst others. In this thesis the system was used in two applications.

The Medipix detector, if covered with an appropriate conversion material, is suitable for detection of thermal and fast neutrons. A portable readout system combined with excellent detector performance made the Medipix2-USB very attractive for use as the ATLAS background monitoring system. 18 devices were adapted, characterised and calibrated; several were left as a benchmark, while 15 were installed in the ATLAS detector and surrounding cavern. X-ray calibration showed very similar response to incident X-rays for all detectors. The response to fast and thermal neutrons varies largely from device to device. This is due to the fact that the converters were custom made and the detection efficiencies vary dramatically with the thickness and enrichment of the material. The detection was found to be $\sim 1\%$ efficient for thermal neutrons and $\sim 0.1\%$ for fast neutrons. Studies were performed to assess angular fast neutron detection efficiency. The commissioning of the system has begun. It was demonstrated that the monitoring network performs well and the first results were recorded during the LHC

startup. Data recorded with the system will give invaluable information on the distribution of radiation in the ATLAS detector, and will help to understand and improve many systems for a future LHC upgrade.

The second application of Medipix was mass spectrometry (MS). Again, the chip offers very high dynamic range because of the single photon counting approach, which is a crucial requirement in MS. The 2D representation of data is also of great advantage. The Medipix detector was placed in the focal plane of the instrument. The measurements performed on a prototype mass spectrometer instantly revealed problems with beam focusing. This can be corrected online with the Medipix acquisition system. It was demonstrated that the system is capable of detecting ions in the range of $5 - 25 \ keV$. Several isotopes from Cu to Pb were used to characterise the detector. The results obtained show very good agreement with reference data. The response of the detector to incident ions is not uniform across the pixel matrix. This should be taken into account during data analysis. More studies have to carried out in order understand this phenomenon. The bare sensor showed ~ 10 times lower sensitivity to ions in comparison to the chip with detector. This suggests research and development should be carried out to investigate new detector formats for use in this application. The radiation hardness of the system has to be studied in order to understand the long term effects of the heavy ions incident on the detector and readout electronics.

Bibliography

[1] W. Roentgen. A new kind of rays. *Nature*, 53:274 – 276, 1896. [cited at p. 1]

[2] Donald A. Glaser. Some effects of ionizing radiation on the formation of bubbles in liquids. *Phys. Rev.*, 87(4):665, Aug 1952. [cited at p. 1]

[3] Yu. K. Akimov. Silicon radiation detectors. *Instruments and Experimental Techniques*, 50(1):1–28, Feb 2007. [cited at p. 2]

[4] George E. Smith. The invention and early history of the ccd. *Nucl. Instr. and Meth. A*, In press, 2009. [cited at p. 2]

[5] C. J. S. Damerell. Charge-coupled devices as particle tracking detectors. *Review of Scientific Instruments*, 69(4):1549–1573, 1998. [cited at p. 2]

[6] C. Da Vi, M. Campbell, E. H. M. Heijne, and G. Stefanini. Imaging of visible photons using hybrid silicon pixel detectors. *Nucl. Instr. and Meth. A*, 355(2-3):414 – 419, 1995. [cited at p. 2]

[7] J Ponpon. Semiconductor detectors for 2d x-ray imaging. *Nucl. Instr. and Meth. A*, 551:15–26, October 2005. [cited at p. 2]

[8] D Pennicard. *3D Detectors for Synchrotron Applications*. PhD thesis, University of Glasgow, 2009. [cited at p. 3]

[9] A Nomerotski. Silicon detectors for tracking and vertexing. *Nucl. Instr. and Meth. A*, 598:33–40, January 2009. [cited at p. 3]

[10] G Mettivier, M Montesi, and P Russo. A digital autoradiography system based on the medipix2 chip: images of 3h and 14c microscales. *Nucl. Instr. and Meth. A*, 518:404–405, February 2004. [cited at p. 3]

[11] A.; Sopczak, S.; Aoulmit, K.; Bekhouche, C.; Bowdery, C.; Buttar, C.; Damerell, D.; Djendaoui, L.; Dehimi, T.; Greenshaw, M.; Koziel, D.; Maneuski, A.; Nomerotski, K.; Stefanov, T.; Tikkanen, T.; Woolliscroft, and S.; Worm. Radiation hardness studies in a ccd with high-speed column parallel readout. *Journal of Instrumentation*, 3, 2008. [cited at p. 3]

[12] D Maneuski. Simulation of the charge transfer inefficiency of column parallel ccds. *Nucl. Instr. and Meth. A*, 591:252–254, 2008. [cited at p. 3]

[13] A; Sopczak, S; Aoulmit, K; Bekhouche, C; Bowdery, C; Buttar, C; Damerell, D; Djendaoui, L; Dehimi, T; Greenshaw, M; Koziel, S; Maneuski, A; Nomerotski, K; Stefanov, T; Tikkanen, T; Woolliscroft, and S; Worm. Modeling of charge transfer inef ciency in a ccd with high-speed column parallel readout. *IEEE Nuclear Science Symposium Conference Record*, pages 2645–2649, 2008. [cited at p. 3]

[14] International Linear Collider. http://www.linearcollider.org/. [cited at p. 3]

[15] Case for Support. Linear collider flavour identification. Lcfi proposal, p306/d89506, LCFI, 15 July 2005. [cited at p. 3]

[16] Glenn F. Knoll. *Radiation detection and Measurement.* John Wisley and Sons, New York, 1979. [cited at p. 6, 7, 9]

[17] G. Lutz. *Semiconductor Radiation Detectors.* Springer-Verlag, Berlin Heidelberg, 1999. [cited at p. 6, 16]

[18] S. M. Sze. *Physics of semiconductor devices.* John Wisley and Sons, New York, 1985. [cited at p. 6, 24, 39]

[19] C. Amsler and et. al. *Physics Letters B667.* Wiley-IEEE, 2008. [cited at p. 10]

[20] Arthur H. Compton. A quantum theory of the scattering of x-rays by light elements. *Phys. Rev.*, 21(5):483–502, May 1923. [cited at p. 12]

[21] Roland Albert Levy. *Microelectronic Materials and Processes.* Springer, New York, 1989. ISBN 0792301544. [cited at p. 14]

[22] Process and Device Simulation Tools. http://www.synopsis.com/tools/tcad/. [cited at p. 20]

[23] Michael Pecht. *Integrated circuit, hybrid, and multichip module package design guidelines: a focus on reliability.* Wiley-IEEE, 1994. ISBN 0471594466. [cited at p. 27]

[24] T Michel and J Durst. Evaluation of a hybrid photon counting pixel detector for x-ray polarimetry. *Nucl. Instr. and Meth. A*, 594:188–195, September 2008. [cited at p. 27]

[25] M.G. Bisogni, G.a.P. Cirrone, G. Cuttone, a. Del Guerra, P. Lojacono, M.a. Piliero, F. Romano, V. Rosso, V. Sipala, and a. Stefanini. Medipix2 as a tool for proton beam characterization. *Nucl. Instr. and Meth. A*, pages 3–5, March 2009. [cited at p. 27]

[26] J. Dammer, P.M. Frallicciardi, J. Jakubek, M. Jakubek, S. Pospisil, E. Prenerova, D. Vavrik, L. Volter, F. Weyda, and R. Zemek. Real-time in-vivo μ-imaging with medipix2. *Nucl. Instr. and Meth. A*, pages 3–5, March 2009. [cited at p. 27]

[27] R. Turchetta, J. D. Berst, B. Casadei, G. Claus, C. Colledani, W. Dulinski, Y. Hu, D. Husson, J. P. Le Normand, J. L. Riester, G. Deptuch, U. Goerlach, S. Higueret, and M. Winter. A monolithic active pixel sensor for charged particle tracking and imaging using standard vlsi cmos technology. *Nucl. Instr. and Meth. A*, 458(3):677 – 689, 2001. [cited at p. 28, 45, 46]

[28] James. R. Janesick. *Photon transfer DN - λ*. SPIE Press, 2007. [cited at p. 28, 33, 40]

[29] Morley M. Blouke, John Canosa, and Nitin Sampat, editors. *Lux transfer: CMOS versus CCD*. SPIE, 2002. [cited at p. 28]

[30] James R. Janesick. Lux transfer: Complementary metal oxide semiconductors versus charge-coupled devices. *Optical Engineering*, 41(6):1203–1215, 2002. [cited at p. 29, 31, 41]

[31] EMVA. Emva standard. Technical report, European Machine Vision Association, 2005. [cited at p. 34]

[32] James. R. Janesick. *Scientific charge-coupled devices*. SPIE Press, 2005. [cited at p. 36]

[33] B Pain, G Yang, TJ Cunningham, C Wrigley, and B Hancock. An enhanced-performance cmos imager with a flushed-reset photodiode pixel. *IEEE Transactions on electron devices*, 50(1):48–56, JAN 2003. [cited at p. 39, 86]

[34] A. Laing, L. Eklund, D. Maneuski, R. Turchetta, and J.J. Velthuis. First particle results for the hepaps4 characterisation. *Nucl. Instr. and Meth. A*, 604(1-2):262 – 264, 2009. PSD8 - Proceedings of the 8th International Conference on Position Sensitive Detectors. [cited at p. 46, 73]

[35] L. Eklund, A. Laing, L. Jones, D. Maneuski, R. Turchetta, and F. Zakopoulos. First results from the hepaps4 active pixel sensor. *Nucl. Instr. and Meth. A*, 598(1):64 – 66, 2009. Instrumentation for Colliding Beam Physics - Proceedings of the 10th International Conference on Instrumentation for Colliding Beam Physics. [cited at p. 48]

[36] D. Maneuski, L. Eklund, A. Laing, R. Turchetta, and V. O'Shea. Characterisation of hepaps4 – a family of cmos active pixel sensors for charged particle

detection. *Nucl. Instr. and Meth. A*, 604(1-2):404 – 407, 2009. PSD8 - Proceedings of the 8th International Conference on Position Sensitive Detectors. [cited at p. 48]

[37] JJ Velthuis, PP Allport, G Casse, A Evans, R Turchetta, A Tyndel, and G Villani. Characterization of active pixel sensors in 0.25 μm cmos technology. *IEEE Transactions on Nuclear Science*, 52(5, Part 3):1887–1891, OCT 2005. [cited at p. 48]

[38] JJ Velthuis, PP Allport, G Casse, A Evans, R Turchetta, and G Villani. A monolithic active pixel sensor for particle detection in 0.25 μm cmos technology. *Nucl. Instr. and Meth. A*, 560(1):40–43, MAY 1 2006. 13th International Workshop on Vertex Detectors, Menaggio, ITALY, SEP 13-18, 2004. [cited at p. 48]

[39] D.G. Mavis and D.R. Alexander. Employing radiation hardness by design techniques with commercial integrated circuit processes. *Digital Avionics Systems Conference, 1997. 16th DASC., AIAA/IEEE*, 1:2.1–15–22 vol.1, Oct 1997. [cited at p. 49, 127]

[40] Leo H. C. Braga, Suzana Domingues, Milton F. Rocha, Leonardo B. Sa, Fernando S. Campos, Filipe V. Santos, Antonio C. Mesquita1, Mrio V. Silva, and Jacobus W. Swart. Layout techniques for radiation hardening of standard cmos active pixel sensors. *Analog Integrated Circuits and Signal Processing*, 57(1-2):129–139, Nov 2008. [cited at p. 49]

[41] P.P. Allport, R. Bates, G. Casse, J. Crooks, A. Evans, L. Jones, V. O'Shea, R. Turchetta, M. Tyndel, J.J. Velthuis, G. Villani, and F. Zakopoulos. R&d on monolithic active pixel sensors (maps): Towards large-area cmos sensors for particle physics. *Nucl. Instr. and Meth. A*, 573(1-2):16 – 18, 2007. Proceedings of the 7th International Conference on Position-Sensitive Detec-

tors - PSD-7, 7th International Conference on Position-Sensitive Detectors. [cited at p. 49, 66, 69]

[42] www.ni.com/labview. [cited at p. 57]

[43] Randolph E. Longshore, editor. *CCD/CMOS hybrid FPA for low light level imaging.* SPIE, 2005. [cited at p. 72]

[44] Jan T. Bosiers, Inge M. Peters, Cees Draijer, and Albert Theuwissen. Technical challenges and recent progress in ccd imagers. *Nucl. Instr. and Meth. A*, 565(1):148 – 156, 2006. Proceedings of the International Workshop on Semiconductor Pixel Detectors for Particles and Imaging - PIXEL 2005. [cited at p. 72]

[45] Hans Bichsel. Straggling in thin silicon detectors. *Rev. Mod. Phys.*, 60(3):663–699, Jul 1988. [cited at p. 76, 99]

[46] J. Jakubek, T. Holy, E. Lehmann, S. Pospisil, J. Uher, J. Vacik, and D. Vavrik. Spatial resolution of medipix-2 device as neutron pixel detector. *Nucl. Instr. and Meth. A*, 546(1-2):164 – 169, 2005. Proceedings of the 6th International Workshop on Radiation Imaging Detectors - Radiation Imaging Detectors 2004. [cited at p. 79, 83]

[47] Z. Vykydal, J. Bouchami, M. Campbell, Z. Dolezal, M. Fiederle, D. Greiffenberg, A. Gutierrez, E. Heijne, T. Holy, J. Idarraga, J. Jakubek, V. Kral, M. Kralik, C. Lebel, C. Leroy, X. Llopart, D. Maneuski, M. Nessi, V. O'Shea, M. Platkevic, S. Pospisil, M. Suk, L. Tlustos, P. Vichoudis, J. Visschers, I. Wilhelm, and J. Zemlicka. The medipix2-based network for measurement of spectral characteristics and composition of radiation in atlas detector. *Nucl. Instr. and Meth. A*, In Press, 2009. [cited at p. 79, 83, 130]

[48] D.J. Skyrme. The passage of charged particles through silicon. *Nucl. Instr. and Meth. A*, 57:61 – 73, 1967. [cited at p. 82]

[49] S. Pospisil, B. Sopko, E. Havrnkov, Z. Janout, J. Konicek, I. Mcha, and J. Pavlu. Si Diode as a Small Detector of Slow Neutrons. *Radiation Protection Dosimetry*, 46(2):115–118, 1993. [cited at p. 82]

[50] M. W. Johnson, S. Manolopoulos, N. J. Rhodes, E. M. Schooneveld, R. Turchetta, and M. R. Daymond. Silicon aps detectors for neutron scattering. *Nucl. Instr. and Meth. A*, 501(1):72 – 79, 2003. Proceedings of the 10th International Workshop on Vertex Detectors. [cited at p. 83]

[51] D. Greiffenberg, M. Fiederle, Z. Vykydal, V. Krl, J. Jakubek, T. Hol, S. Pospsil, D. Maneuski, V. O'Shea, M. Suk, M. Krlk, C. Lebel, and C. Leroy. Detection efficiency of atlas-mpx detectors with respect to neutrons. *Nucl. Instr. and Meth. A*, 607(1):38 – 40, 2009. [cited at p. 84, 131]

[52] Multidimensional Integrated Intelligent Imaging Consortium. http://mi3.shef.ac.uk/what.html, 2004 - 2008. [cited at p. 85]

[53] Sarah E. Bohndiek, Costas D. Arvanitis, Gary J. Royle, Robert D. Speller, Andy T. Clark, Jamie P. Crooks, Mark L. Prydderch, Renato Turchetta, Andrew Blue, and Val O'Shea. Characterization studies of two novel active pixel sensors. *Optical Engineering*, 46(12):124003, 2007. [cited at p. 86]

[54] Zhimin Zhou, B. Pain, and E.R. Fossum. Cmos active pixel sensor with on-chip successive approximation analog-to-digital converter. *Electron Devices, IEEE Transactions on*, 44(10):1759–1763, Oct 1997. [cited at p. 87]

[55] Morley M. Blouke, Nitin Sampat, and Ricardo J. Motta, editors. *Accurate estimation of conversion gain and quantum efficiency in CMOS imagers.* SPIE, 2003. [cited at p. 90]

[56] S.E. Bohndiek, A. Blue, A.T. Clark, M.L. Prydderch, R. Turchetta, G.J. Royle, and R.D. Speller. Comparison of methods for estimating the conversion gain of cmos active pixel sensors. *Sensors Journal, IEEE*, 8(10):1734–1744, Oct. 2008. [cited at p. 90, 91]

[57] A. Blue, R. Bates, A. Laing, D. Maneuski, V. O'Shea, A. Clark, M. Prydderch, R. Turchetta, C. Arvanitis, and S. Bohndiek. Characterisation of vanilla - a novel active pixel sensor for radiation detection. *Nucl. Instr. and Meth. A*, 581(1-2):287 – 290, 2007. VCI 2007 - Proceedings of the 11th International Vienna Conference on Instrumentation. [cited at p. 98]

[58] J. Cabello, A. Bailey, I. Kitchen, A. Clark, J. Crooks, R. Halsall, M. Key-Charriere, S. Martin, M. Prydderch, R. Turchetta, and K. Wells. Digital autoradiography using ccd and cmos imaging technology. *Nuclear Science Symposium Conference Record, 2006. IEEE*, 4:2607–2612, 29 2006-Nov. 1 2006. [cited at p. 98]

[59] David A. Dorn and Andrew D. Holland, editors. *Evaluation and observation of CMOS imager as detector for astronomy.* SPIE, 2006. [cited at p. 98]

[60] e2V Technologies. http://www.e2v.com/. [cited at p. 100]

[61] J.A. Ballin, J.P. Crooks, P.D. Dauncey, A.-M. Magnan, Y. Mikami, O.D. Miller, M. Noy, V. Rajovic, M.M. Stanitzki, K.D. Stefanov, R. Turchetta, M. Tyndel, E.G. Villani, N.K.Watson, and J.A. Wilson. Monolithic active pixel sensors (maps) in a quadruple well technology for nearly 100 percent fill factor and full cmos pixels. *Sensors (Peterborough, NH)*, 2008. [cited at p. 106]

[62] S Kleinfelder, F Bieser, YD Chen, R Gareus, HS Matis, M Oldenburg, F Retiere, HG Ritter, HH Wieman, and E Yamamoto. Novel integrated cmos sensor circuits. *IEEE Transactions on Nuclear Science*, 51(5, Part 1):2328–2336, OCT 2004. IEEE Nuclear Science Symposium/Room-Temperature Semiconductor Detector Workshop/Symposium on Nuclear Power Systems (2003 NSS/RTSD/SNPS), Rome, ITALY, NOV 15, 2003. [cited at p. 109]

[63] B Fowler, MD Godfrey, J Balicki, and J Canfield. Low noise readout using active reset for cmos aps. In *proceedings of SPIE*, volume 3965, pages 126–135, 2000. [cited at p. 111]

[64] B Pain, TJ Cunningham, B Hancock, G Yang, S Seshadri, and A Ortiz. Reset noise suppression in two-dimensional CMOS photodiode pixels through column-based feedback-reset. In *International electron devices 2002 meeting, technical digest*, pages 809–812, 2002. IEEE International Electron Devices Meeting, San Francisco, CA, Dec 08-11, 2002. [cited at p. 111]

[65] http://www.aspect-sys.com. [cited at p. 112]

[66] R. Turchetta, T. Anaxagoras, J. Crooks, A. Godbeer, N. Allinson, T. Pickering, A. Blue, D. Maneuski, and V. OShea. Reset noise reduction architectures for the detection of charged particles. In *International Image Sensor Workshop*, 2009. [cited at p. 116]

[67] X. Llopart. *Design and Characterization of 64K Pixels Chips Working in Single Photon Processing Mode*. PhD thesis, Mid Sweden University, http://cdsweb.cern.ch/record/1056683/files/thesis-2007-062.pdf, 2007. [cited at p. 121, 127]

[68] L. Tlustos. *Performance and limitations of high granularity single photon processing X-ray imaging detectors*. PhD thesis, Vienna University of Technology, http://cdsweb.cern.ch/record/846447/files/thesis-2005-032.pdf, 2005. [cited at p. 121, 122]

[69] Zdeněk Vykydal. Microprocessor controlled usb interface for medipix2 detector. Master's thesis, Czech Technical University, 2005. [cited at p. 121]

[70] M. Campbell, E.H.M. Heijne, G. Meddeler, E. Pernigotti, and W. Snoeys. A readout chip for a 6464 pixel matrix with 15-bit single photon counting. *Nuclear Science, IEEE Transactions on*, 45(3):751–753, Jun 1998. [cited at p. 122]

[71] Jan Jakubek, Stanislav Pospisil, Josef Uher, Jiri Vacik, and Daniel Vavrik. Single neutron pixel detector based on medipix-1 device. *Nuclear Science Symposium Conference Record, 2003 IEEE*, pages 1444–1447, 2004. [cited at p. 122]

[72] C Bert, D Niederlohner, J Giersch, K-F Pfeiffer, and G Anton. Computed tomography using the medipix1 chip. *Nucl. Instr. and Meth. A*, 509:240–250, August 2003. [cited at p. 122]

[73] J Watt, D Davidson, C Johnston, C Smith, L Tlustos, B Mikulec, K Smith, and M Rahman. Dose reductions in dental x-ray imaging using medipix. *Nucl. Instr. and Meth. A*, 513:65–69, November 2003. [cited at p. 122]

[74] A. Fornaini, T. Boerkamp, R. de Oliveira, and J.L. Visschers. A tiled array of hybrid pixel detectors for x-ray imaging. *Nuclear Science, IEEE Transactions on*, 51(4):1824–1828, Aug. 2004. [cited at p. 122]

[75] David San Segundo Bello, Martin van Beuzekom, Peter Jansweijer, Hans Verkooijen, and Jan Visschers. An interface board for the control and data acquisition of the medipix2 chip. *Nucl. Instr. and Meth. A*, 509(1-3):164 – 170, 2003. Proceedings of the 4th Internatonal Workshop on Radiation Imaging Detectors. [cited at p. 125]

[76] Zdenek Vykydal, Jan Jakubek, and Stanislav Pospisil. Usb interface for medipix2 pixel device enabling energy and position-sensitive detection of heavy charged particles. *Nucl. Instr. and Meth. A*, 563(1):112 – 115, 2006. Proceedings of the 7th International Workshop on Radiation Imaging Detectors - IWORID 2005. [cited at p. 125]

[77] X. Llopart, M. Campbell, R. Dinapoli, D. San Segundo, and E. Pernigotti. Medipix2: A 64-k pixel readout chip with 55-?m square elements working in single photon counting mode. *Nuclear Science, IEEE Transactions on*, 49(5):2279–2283, Oct 2002. [cited at p. 127]

[78] S. Baranov, M. Bosman, I. Dawson, V. Hedberg, A. Nisati, and M. Shupe. Estimation of radiation background, impact on detectors, activation and shielding optimisation in atlas. Atlas radiation background task force summary document, atl-gen-2005-001, CERN, 13 January 2005. [cited at p. 128]

165

[79] T. Holy, J. Jakubek, S. Pospisil, J. Uher, Z. Vykydal; Z. Dolezal, M. Suk, I. Wilhelm; M. Campbell, E. Heijne, X. Llopart, L. Tlustos; C. Leroy; B. Mikulec; M. Nessi; C. Buttar, V. O'Shea, and K. Smith. Proposal to measure spectral characteristics and composition of radiation in atlas by medipix2-usb devices. Atlas internal note, atl-gen-2005-001, ATLAS, 18 October 2006. [cited at p. 128]

[80] M. Shupe I. Dawson. Radiation background benchmarking at the lhc and simulations for an atlas upgrade at the slhc. Atlas project document no. atc-ge-xx-0000, 1/3/2006, CERN, 13 January 2005. [cited at p. 128]

[81] M. Fiederle, D. Greiffenberg, J. Idarraga, J. Jakubek, V. Kral, C. Lebel, C. Leroy, G. Lord, S. Pospisil, V. Sochor, and M. Suk. Energy calibration measurements of medipix2. *Nucl. Instr. and Meth. A*, 591(1):75 – 79, 2008. Radiation Imaging Detectors 2007 - Proceedings of the 9th International Workshop on Radiation Imaging Detectors. [cited at p. 130, 136]

[82] D Twerenbold. Biopolymer mass spectrometer with cryogenic particle detectors. *Nucl. Instr. and Meth. A*, 370:253–255, February 1996. [cited at p. 138]

[83] Mahadeva P. Sinha and Mark Wadsworth. Miniature focal plane mass spectrometer with 1000-pixel modified-ccd detector array for direct ion measurement. *Review of Scientific Instruments*, 76(2):025103, 2005. [cited at p. 138, 139]

[84] David W. Koppenaal, Charles J. Barinaga, M. Bonner Denton, Roger P. Sperline, Gary M. Hieftje, Gregory D. Schilling, Francisco J. Andrade, James H. Barnes, and IV IV. Ms detectors. *Analytical Chemistry*, 77(21):418 A–427 A, 2005. [cited at p. 138, 139]

[85] C Giffin, H Boettger, and D Norris. An electrooptical detector for focal plane mass spectrometers. *International Journal or Mass Spectrometry and Ion Physics*, 15:437–449, December 1974. [cited at p. 139]

[86] Stephen Fuerstenau, George Soli, Thomas Cunningham, Bruce Hancock, Bedabrata Pain, and Mahadeva Sinha. Active pixel sensors for mass spectrometry. *International Journal of Mass Spectrometry*, 215(1-3):101 – 111, 2002. [cited at p. 139]

[87] Private communication with kiev group. [cited at p. 149]

[88] M Trocmé, S Higueret, D Husson, a Nourreddine, and T D Lê. Development of a new electronic personal neutron dosemeter using a cmos active pixel sensor. *Radiation protection dosimetry*, 126:536–40, January 2007. [cited at p. 152]

[89] S Higueret, D Husson, T Le, a Nourreddine, and N Michielsen. Electronic radon monitoring with the cmos system-on-chip alpharad. *Nucl. Instr. and Meth. A*, 584:412–417, January 2008. [cited at p. 153]

[90] J. Cabello, K. Wells, A. Metaxas, A. Bailey, I. Kitchen, A. Clark, M. Prydderch, and R. Turchetta. Digital autoradiography imaging using cmos technology: First tritium autoradiography with a back-thinned cmos detector and comparison of cmos imaging performance with autoradiography film. *Nuclear Science Symposium Conference Record, 2007. NSS '07. IEEE*, 5:3743–3746, 26 2007-Nov. 3 2007. [cited at p. 153]

Appendices

Appendix A

List of abbreviations

Abbreviation	Description	Definition
MAPS	**M**onolithic **A**ctive **P**ixel **S**ensor	page iii
CMOS	**C**omplementary **M**etal **O**xide **S**emiconductor	page iii
CCD	**C**harge-**C**oupled **D**evices	page iii
ATLAS	**A** **T**oroidal **L**HC **A**pparatu**S**	page iv
VLSI	**V**ery **L**arge **S**cale **I**ntegration	page 2
ILC	**I**nternational **L**inear **C**ollider	page 3
LCFI	**L**inear **C**ollider **F**lavour **I**dentification	page 3
HEPAPS	**H**igh **E**nergy **P**hysics **A**ctive **P**ixel **S**ensor	page 4
MIP	**M**inimum **I**onising **P**article	page 4
UV	**U**ltra**V**oilet	page 4
eLeNA	e^- **L**ow e^- **N**oise **A**PS	page 4
TCAD	**T**echnology **C**omputer-**A**ided **D**esign	page 22
MOSFET	**M**etal **O**xide **S**emiconductor **F**ield-**E**ffect **T**ransistor	page 22
CDS	**C**orrelated **D**ouble **S**ampling	page 29
PTC	**P**hoton **T**ransfer **C**urve	page 30
QE	**Q**uantum **E**fficiency	page 30

Abbreviation	Description	Definition
FPN	**F**ixed **P**attern **N**oise	page 32
ADC	**A**nalog to **D**igital **C**onverter	page 32
LED	**L**ight **E**mitting **D**iode	page 34
FW	**F**ull **W**ell capacity	page 37
DR	**D**ynamic **R**ange	page 37
PRNU	**P**ixel **R**esponse **N**on-**U**niformity	page 40
EGT	**E**nclosed **G**eometry **T**ransistors	page 49
DAQ	**D**ata **A**c**Q**uisition	page 51
FPGA	**F**ield-**P**rogrammable **G**ate **A**rray	page 51
PCI	**P**eripheral **C**omponent **I**nterconnect	page 51
RAM	**R**andom **A**ccess **M**emory	page 52
MI3	**M**ultidimensional **I**ntegrated **I**ntelligent **I**maging	page 85
ROI	**R**egion **O**f **I**nterest	page 85
LVDS	**L**ow **V**oltage **D**ifferential **S**ignalling	page 124

Appendix B

List of publications

Below is the list of publications arised during the time of work on this thesis.

1. A. Blue, R. Bates, A. Laing, D. Maneuski, V. O'Shea, A. Clark, M. Prydderch, R. Turchetta, C. Arvanitis, S. Bohndiek,
   Characterisation of Vanilla - a novel active pixel sensor for radiation detection, Nucl. Instr. and Meth. A, Volume 581, Issues 1-2, 21 October 2007, Pages 287-290.

2. Sopczak, A.; Aoulmit, S.; Bekhouche, K.; Bowdery, C.; Buttar, C.; Damerell, C.; Davies, G.; Djjendaoui, D.; Dehimi, L.; Greenshaw, T.; Koziel, M.; Maneuski, D.; Stefanov, K.; Tikkanen, T.; Woolliscroft, T.; Worm, S;
   Radiation hardness studies in a CCD with high-speed column parallel read-out, Journal of Instrumentation, 3, May, 2008

3. D. Maneuski,
   Simulation of the charge transfer inefficiency of column parallel CCDs, Nucl. Instr. and Meth. A, Volume 591, Issue 1, 11 June 2008, Pages 252-254.

4. A. Blue, R. Bates, S.E. Bonhiek, A. Clark, A. Costas, T. Greenshaw, A. Laing, D. Maneuski, R. Turchetta, V. O'Shea,

Spectral characterisation and noise performance of Vanilla an active pixel sensor, Nucl. Instr. and Meth. A, Volume 591, Issue 1, 11 June 2008, Pages 237-240.

5. L. Eklund, A. Laing, L. Jones, D. Maneuski, R. Turchetta, F. Zakopoulos, *First results from the HEPAPS4 active pixel sensor*, Nucl. Instr. and Meth. A, Volume 598, Issue 1, 1 January 2009, Pages 64-66.

6. D. Greiffenberg, M. Fiederle, Z. Vykydal, V. Kral, J. Zemlicka, J. Jakubek, T. Holy, S. Pospisil, D. Maneuski, V. O'Shea, M. Suk, M. Kralik, *Detection efficiency of MPX-ATLAS devices with respect to neutrons*, Nucl. Instr. and Meth. A, Volume 607, Issue 1, 1 August 2009, Pages 38-40.

7. Z. Vykydal, J. Bouchami, M. Campbell, Z. Dolezal, M. Fiederle, D. Greiffenberg, A. Gutierrez, E. Heijne, T. Holi, J. Idarraga, J. Jakubek, V. Kral, M. Kralik, C. Lebel, C. Leroy, X. Llopart, D. Maneuski, M. Nessi, V. O'Shea, M. Platkevic, S. Pospisil, V. Sochor, M. Suk, L. Tlustos, P. Vichoudis, I. Wilhelm and J. Zemlicka, *The Medipix2-based network for measurement of spectral characteristics and composition of radiation in ATLAS detector*, Nucl. Instr. and Meth. A, Volume 607, Issue 1, 1 August 2009, Pages 35-37.

8. D. Maneuski, L. Eklund, A. Laing, V. O'Shea, R. Turchetta, *Characterisation of HEPAPS4 - a family of CMOS active pixel sensors for charged particle detection*, Nucl. Instr. and Meth. A, Volume 604, Issue 1-2, June 2009, Pages 404-407.

9. A. Laing, L. Eklund, D. Maneuski, J. Velthuis, *First particle results for the HEPAPS4 characterisation*, Nucl. Instr. and Meth. A, Volume 604, Issue 1-2, June 2009, Pages 262-264.

10. A. Blue, S. Huston, A. Laing, D. Maneuski, V. O'Shea, R. Turchetta, *Optical and electrical characterisation of a back-thinned CMOS active pixel*

sensor, Nucl. Instr. and Meth. A, Volume 604, Issue 1-2, June 2009, Pages 215-217.

11. D. Maneuski, L. Eklund, M. Kralik, A. Laing, V. O'Shea, S. Pospisil, Z. Vykydal,
    Evaluation of silicon monolithic APS as a neutron detector, IEEE NSS 2008. Conference proceedings.

12. Z. Vykydal, J. Bouchami, M. Campbell, Z. Dolezal, M. Fiederle, D. Greiffenberg, A. Gutierrez, E. Heijne, T. Holy, J. Idarraga, J. Jakubek, V. Kral, M. Kralik, C. Lebel, C. Leroy, X. Llopart, D. Maneuski, M. Nessi, V. O'Shea, M. Platkevic, S. Pospisil, V. Sochor, J. Solc, M. Suk, L. Tlustos, P. Vichoudis, J. Visschers, I. Wilhelm, J. Zemlicka,
    Evaluation of the ATLAS-MPX devices for neutron field spectral composition measurement in the ATLAS experiment, IEEE NSS 2008. Conference proceedings.

13. A. Sopczak, S. Aoulmit, K. Bekhouche, C. Bowdery, C. Buttar, C. Damerell, D. Djendaoui, L. Dehimi, T. Greenshaw, M. Koziel, D. Maneuski, A. Nomerotski, K. Stefanov, T. Tikkanen, T. Woolliscroft, S. Worm,
    Modeling of charge transfer inefficiency in a CCD with high-speed column parallel readout, IEEE NSS 2008. Conference proceedings.

14. S. Cipiccia, R. Issac, R. Islam, G. Vieux, M. Wiggins, R. Shanks, A. Reitsma, D. Maneuski, V. O'Shea, N. Lemos, R. Bendoyro, J. Martins, F. Fiuza, M. Marti, L. Silva, R. Pattathil, P. Foster, N. Bourgeois, T. Ibbotson, D. Jaroszynski, J. Mendanha Dias,
    Study of betatron radiation produced by laser plasma accelerator, Presented at SPIE Europe Optics + Optoelectronics Conference, Prague, Czech Republic 2009.

15. R. Turchetta, T. Anaxagoras, N. Allinson, T. Pickering, A. Blue, D. Maneuski, V. O'Shea,
    Reset noise reduction architectures for the detection of charged particles,
    Presented at International Image Sensor Workshop, Bergen, Norway, 2009.

16. A. Blue, R. Bates, D. Maneuski, A. Laing, R. Turchetta, A. Clark, N. Allinson, V. O'Shea,
    A review of MI3 produced active pixel sensors, Presented at International Workshop on Radiation Imaging Detectors, Prague, Czech Republic 2009.

17. E. Gimenez, D. Maneuski, A. Mac Raighne, C. Parkes, R. Bates, V. O'Shea, C. Fleta, G. Pellegrini, M. Lozano, L. Alianelli, K.J.S. Sawhney, J. Marchal, N. Tartoni,
    Characterization of a 3D Medipix2 detector with a micro-focused synchrotron beam, Presented at International Workshop on Radiation Imaging Detectors, Prague, Czech Republic 2009.

18. S. E. Bohndiek, A. Blue, J. Cabello, A. T. Clark, N. Guerrini, P. M. Evans, E. J. Harris, A. Konstantinidis, D. Maneuski, J. Osmond, V. O'Shea, R. D. Speller, R. Turchetta, K. Wells, H. XingLiang, H. Zin and N. Allinson,
    Characterization and testing of LAS – a prototype 'Large Area Sensor' for medical imaging applications, Accepted for publication in IEEE Transactions on Nuclear Science.